THE FLORIDA STATE UNIVERSITY

COLLEGE OF ARTS AND SCIENCES

THE COASTAL UPWELLING CYCLE ON A BETA-PLANE: HYDRODYNAMICS AND THERMODYNAMICS

By
J. DANA THOMPSON

A Dissertation submitted to
the Department of Meteorology
in partial fulfillment of the
requirements for the degree of
Doctor of Philosophy

Approved:

James J. O'Brien
Professor Directing Dissertation

Richard L. Haff

Yoshi

Christopher Hunter

Jean J. Stephens

Jean J. Stephens

June, 1974

June, 1974

ABSTRACT

A set of governing equations is derived for the vertically-averaged velocity, density, and thickness fields in a time-dependent, nonlinear, two-layer model of coastal upwelling. The model includes the effects of the earth's rotation, bottom topography, an atmospheric pressure gradient, short and long-wave radiation, latent and sensible heat flux, horizontal and vertical turbulence, and retains both barotropic and baroclinic modes. Surface, interfacial, and bottom stresses and vertical mixing based on a parameterization of boundary and shear generated turbulence are incorporated in the model.

Depth of the mixed layer, stratification, and sea surface temperatures are predicted explicitly. Solutions in coastal upwelling zone require a realistic Sverdrup ocean interior and the existence of westward propagating Rossby waves. Depth-dependent momentum equations are developed and solved analytically to account for Ekman-like boundary layers occurring in high vertical shear zones. Solutions to the vertically-averaged momentum equations for the two-dimensional case are obtained using a highly efficient semi-implicit numerical scheme and a discrete variation telescoping grid which allows high resolution near the coast.

Upon reconstruction of the total flow fields for model cases with and without bottom topography, solar heating, and continuous wind forcing, several features observed in actual coastal upwelling situations are reproduced and investigated, including: 1) Strong sea surface temperature gradients which appear within 10-50 km of the coast. 2) The equatorward surface jet which is found within the baroclinic Rossby radius of deformation of the coast and the poleward undercurrent which appears over the continental shelf. 3) The two cyclonically rotating cells reported by Mooers et al. (1973), as situated in a plane normal to and within 10-50 km of the coast. These model results are compared directly with observations and the dynamical basis for each is examined in some detail.

ACKNOWLEDGMENTS

This work was supported primarily by the Office of Naval Research, Ocean Science and Technology Branch. The International Decade of Ocean Exploration (IDOE) provided partial support through the Coastal Upwelling Ecosystems Analysis (CUEA) program under NSF Grant No. GX-33502. The author was supported in part by a graduate fellowship from the University Corporation for Atmospheric Research. Computations were performed on the CDC 6600/7600 system at the National Center for Atmospheric Research, Boulder, Colorado and on the CDC 6500 at the Florida State University, Tallahassee. NCAR and UCAR are sponsored by the National Science Foundation.

It is with utmost respect and gratitude that I acknowledge my major professor, Dr. James J. O'Brien. He taught me well, challenged me often, and inspired me throughout my graduate career. Dr. O'Brien's suggestions and criticisms during the course of this research were most constructive and enlightening. The members of my doctoral committee, Dr. J. J. Stephens, Dr. Phil Hsueh, Dr. Richard Pfeffer, and Dr. Christopher Hunter, deserve particular plaudits for their guidance and stimulating dialogue during

the past three years. Dr. Chris Mooers, Dr. Jane Huyer, Dr. Richard Garvine, Dr. John Allen, Dr. Merritt Stevenson, Dr. David Halpern and Dr. N. D. Bang deserve many thanks for presenting fertile ideas and observations pertinent to this research. Sincere appreciation is extended to my colleagues Dr. John Lee, Mr. John Kindle, Mr. Richard McNider, and especially Dr. Harley Hurlburt for providing many hours of fruitful discussions.

I am grateful to Mr. Dewey Rudd for drafting many of the figures, to Mrs. Gerry Woodhouse for typing most of the early draft versions of the manuscript, and to Mrs. Janina Richards for typing the final copy.

In conclusion, I wish to thank my understanding wife Brenda, for encouraging and supporting me in this research.

TABLE OF CONTENTS

LIST OF TABLES

LIST OF ILLUSTRATIONS

24. Time-series of mixed-layer depth (a) and temperature (b) at 1 km and 4 km offshore for the heated (solid) and unheated (dashed) continental shelf continuously forced case 103

1. INTRODUCTION

Smith (1968) defines upwelling as "ascending motion of some minimum duration and extent by which water from the subsurface layers is brought into the surface layer and is removed from the area of upwelling by horizontal flow." Coastal upwelling results when prevailing winds produce a condition of surface divergence near a coastal boundary. The simplest mathematical description of coastal upwelling was presented by Thorade (1909) in an extension of Ekman's (1905) pioneering work.

Coastal upwelling off the west coasts of continents affects both the marine ecology and the climate of the adjacent land. The disproportionately high biological productivity in the narrow band of cold upwelled water accounts for over half the world's commercial fish catch (Ryther, 1969). Lowered sea surface temperatures in these areas suppress atmospheric convection and evaporation and produce a stable, humid-desert environment.

Recently the physical oceanography and biology of coastal upwelling has received widespread interest. Elaborate field studies in the United States and abroad have been mounted in an intensive effort to study coastal upwelling circulation dynamics and its phenomenal biological productivity. The global search for additional high-protein food

sources, the increased chemical, nuclear, and thermal pollution in coastal upwelling zones, and the dramatic mesoscale air-sea interactions which occur there have each spurred this substantial research.

Understanding the voluminous data obtained in such field programs requires a sophisticated theoretical framework. For many years that framework consisted of little more than the work of Ekman (1905). However, substantial contributions to the theoretical literature have been made in the past decade. Recent numerical and analytical models of coastal upwelling along a north-south coast have reproduced numerous features prominent in actual observations. Ekman-type zonal flows, offshore in upper regions, onshore in lower regions under equatorward winds are a common thread in these models, although there is diversity in the dynamical basis for the return flows. An equatorward near-surface jet, confined within the baroclinic Rossby radius of deformation length scale of the coast also has been successfullly modeled (O'Brien and Hurlburt, 1972; Allen, 1973). It now appears certain that the formation of this jet can be ascribed to conservation of potential vorticity (Charney, 1955). Finally, a poleward undercurrent, weaker in strength but within the same length scale as the surface jet, also has been reproduced (Hurlburt and Thompson, 1973). While this undercurrent is a striking component of the real upwelling circu-

reproduced (Hurlburt and Thompson, 1973). While this undercurrent is a striking component of the real upwelling circu-

lation, it is not yet clear which of several competing dynamical mechanisms is responsible for the feature. It

does appear that nonlocal properties of the wind stress are important (Pedlosky, 1974; Hurlburt, 1974; Gill and Clarke, 1973; Suginohara, 1973).

Certainly the recent advances in modeling gross aspects of the coastal upwelling circulation are encouraging. It is notable, however, that these advances concern themselves solely with currents along straight coastlines. With the exception of Hurlburt (1974), virtually no progress has been made in accommodating more realistic, irregular coastlines and attendant three-dimensionality. Nor has significant progress been made in accounting for the time evolution of temperature, salinity, and density fields during the upwelling process.

Ideally, the analysis of coastal upwelling would proceed from a continuously stratified analytical model. Although great difficulties are encountered in modeling the singular coastal corner region, models of coastal upwelling in a continuously stratified ocean have been constructed (Allen, 1973; Pedlosky, 1974; Pietrafesa, 1973). In many ways these models suffer from lack of realism. Analyses are restricted largely to steady, linear theory with highly idealized geometries and boundary conditions. While quite successful in predicting gross, steady-state circulation patterns, they fail to cope with the real and important complications introduced by time-dependent forcing, turbulent patterns, they fail to cope with the real and important complications introduced by time-dependent forcing, turbulent mixing (especially with regard to deepening of the mixed layer), and the existence of thermoclines and pycnoclines.

These features must be considered in both ecosystem modeling of the upwelling regime and in predicting sea-surface temperatures.

Numerical models provide an alternative approach to understanding coastal upwelling dynamics. While they too suffer from lack of realism, a careful formulation of the governing equations, numerical scheme and boundary conditions can lead to a useful, sophisticated and instructive tool for building a theoretical model. Heretofore, numerical models of coastal upwelling have included only a crude treatment of thermodynamics. In the layered models of O'Brien and Hurlburt (1972), Hurlburt and Thompson (1973), Thompson and O'Brien (1973), and McNider and O'Brien (1973), a constant density (both in space and time) is maintained in each layer, with no mixing allowed across an interface. Consequently, there is no realistic steady state possible. Implicit in all these models is the assumption that the time scale for vertical advection is much shorter than that for vertical diffusion due to turbulence. The work of Kraus and Turner (1967), Denman (1973), Denman and Miyake (1973), and Pollard and Millard (1970) in studies of the oceanic wind-mixed layer and analogous laboratory work of Kato and Phillips (1969) and Thompson (1969) casts doubt on the general validity of this assumption. Under conditions of strong surface turbulence, tidal mixing or shear instability in
validity of this assumption. Under conditions of strong surface turbulence, tidal mixing or shear instability in
the upwelling zone, the assumption is particularly suspect. Indeed, it will be shown in this paper that vertical mixing

may be comparable to vertical advection during the week to ten-day coastal upwelling event time scale. In addition, changes in the density field due to solar heating, vertical mixing and horizontal advection may be significant over the same event time scale. In this paper an upwelling event will be defined as an interval, longer than an inertial period, during which local winds initiate and maintain coastal upwelling. The importance of the upwelling event to upwelling off the west coast of the United States has been demonstrated by O'Brien and Grotjahn (1974).

Our investigations proceed from numerical and analytical solutions of time-dependent, nonlinear hydrodynamic and thermodynamic equations. Although the governing equations will be formulated for the general case, longshore length scales will be assumed much greater than offshore scales in order to ignore longshore variations in the velocity and density fields. Time scales of interest range from less than a day to several months. Vertical turbulence and solar heating are parameterized using laboratory and oceanographic observations as well as dimensional analysis. Results of the model are compared directly with observations.

It is the purpose of this paper to investigate at least three phenomena presumed characteristic of coastal upwelling regions. First, we are interested in the cellular circulations situated in a vertical plane normal to and within the baroclinic Rossby radius of deformation of the coast. Mooers et al. (1973) proposed the existence of two

semi-permanent cyclonic cells during active upwelling off Oregon. Mittelstaedt and Koltermann (1974), upon analyzing currents in the Northwest African Upwelling Area, describe two cells having opposite rotation, the near-surface cell being cyclonic. Finally, Bang (1973) indicates that near-surface mixing cells may propagate through frontal zones during upwelling off Southwest Africa. We will investigate possible dynamical explanations for these circulations.

The second aspect of interest concerns the remarkable horizontal temperature gradients and attendant oceanic fronts which occur within 10-50 km of the coast. Sea surface temperatures (henceforth abbreviated SSTs) may drop by 10°C in one week during intense coastal upwelling, a change comparable to the amplitude of the annual cycle (Thompson et al., 1972). Often during active upwelling extremely stable meteorological conditions prevail near the coast, with attendant low fog, stratus, and cool coastal land temperatures. There appears to be a strong feedback between these SST changes and the sea breeze circulation (Johnson and O'Brien, 1973).

Surface convergence in the vicinity of the oceanic front may be quite strong, with long foam lines, color fronts, and tidal rips tending to align themselves along the coastal orientation. Such intense surface convergence in frontal zones off Oregon has been studied by Stevenson et al. (1973), though little is known about the maintenance and decay of the ocean fronts themselves.

Finally, we wish to investigate the equatorward surface jet and poleward subsurface undercurrent which have been found in coastal upwelling zones. The equatorward surface jet has been documented by Mooers et al., (1973), off Oregon, and by Mittelstaedt and Koltermann (1974) off Northwest Africa. Poleward undercurrents have been observed near the west coasts of South America (Gunther, 1936; Wyrtki, 1963, 1967; Wooster and Gilmartin, 1961), North America (Pavlova, 1966; Pillsbury et al., 1970; Mooers et al., 1973) and Africa (Defant, 1936; Hart and Currie, 1960). They appear on the continental shelf and slope at depths of 50-1000 m with speeds of 5-20 cm sec^{-1}. The theoretical explanation for the undercurrent remains quite controversial, as noted by Hurlburt and Thompson (1973) in their review of the various theories. In the same paper they propose a new theory which relates the undercurrent to the β-effect, the existence of a Sverdrup balance in the ocean interior, and the development of a north-south sea surface slope. In light of recent work that theory will be re-examined in assessing the effects of vertical transfers of horizontal momentum, deepening of the wind-mixed layer, and heating, on the longshore flow.

This research is presented in three units. The first unit (1) describes the formulation of the vertically-averaged governing equations for the two-layer model, (2) discusses the parameterization of vertical turbulence and solar heating, and (3) presents an analytical solution to finite-depth

Ekman-thermal wind equations obtained for departures of the horizontal flow from the vertical average. The second unit includes a discussion of the relevant parameter space, the numerical scheme, and the initial and boundary conditions. Finally, unit three offers representative results from the numerical model, compares them with observations, and critically analyzes the contributions and deficiencies of the work.

It will be demonstrated in this paper that a realistic sea surface temperature front and a two-cell circulation in the zonal flow can be obtained in a simple numerical-analytical model of coastal upwelling. Both the equatorward surface jet and poleward undercurrent, conspicuous in recent observations, are produced within several baroclinic Rossby radii of deformation of the model coastline during a time scale short compared to the diffusion scale. Aspects of frontogenesis and frontolysis, not heretofore studied in coastal upwelling models, will be examined.

2. MODEL FORMULATION – VERTICALLY AVERAGED EQUATIONS

In this section a set of governing equations is derived which describes the vertically integrated and time-dependent velocity and density fields in a numerical model of the eastern ocean circulation. The effects of vertical turbulence are parameterized via dimensional and physical arguments verified by laboratory and oceanographic observations. A parameterization of incident solar short-wave radiation, emitted long-wave radiation and latent and sensible heat flux is incorporated in the governing equations. A discussion of turbulent transfers of heat and momentum concludes the section.

Consider a stably-stratified, rotating, incompressible fluid adjacent to the west coast of a continent. A schematic of the model geometry for the particular case of an x-z plane two-layer model is shown in Fig. 1. Suppose the fluid consists of m incompressible layers having initial thicknesses $h_j(x,t)$ and densities $\rho_j(x,t)$, $j = 1(1)\ m$, counting down from the surface layer. Assume that the fluid is hydrostatic and Boussinesq and that the hydrodynamic and thermodynamic equations are integrated vertically over the depth of each layer. The vertically-averaged horizontal velocity and density com-

tions are integrated vertically over the depth of each layer. The vertically-averaged horizontal velocity and density com-

ponents are thus independent of depth within each layer.

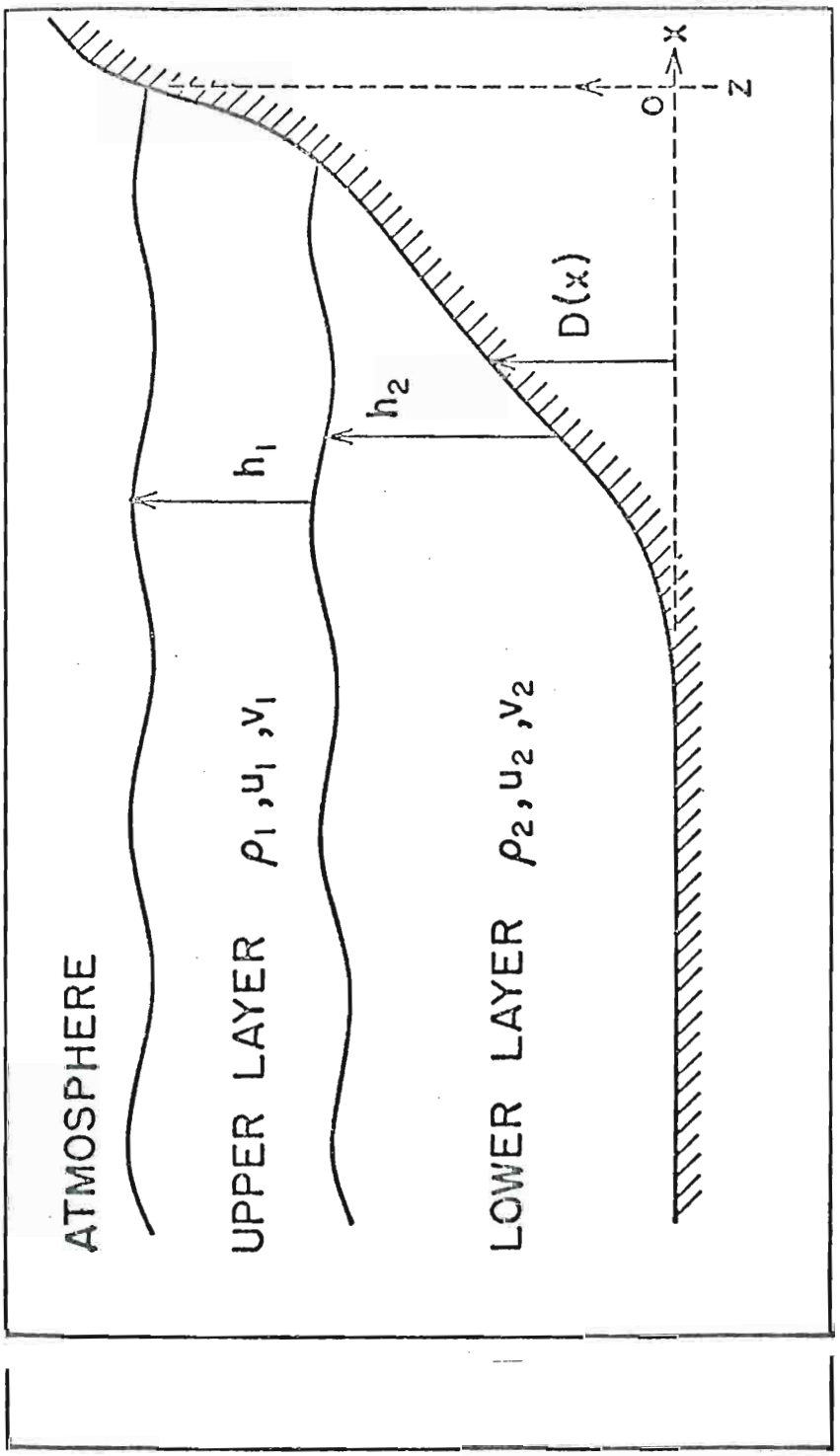

Fig. 1. Schematic diagram of the geometry for the two-layer model. Height of the bottom topography above some reference level is D(x).

Thermodynamic effects will be included insofar as the density field in space and time is explicitly predicted and parameterization of turbulent mixing across the interface and the effects of solar heating are included.

2.1 The density and continuity equations

Consider the simplest fluid system which retains the baroclinic mode, i.e., a two-layer system. Assume that turbulent energy may be generated (1) by surface action of the winds and waves, (2) by shear instabilities, and (3) by tidal action. Further, in accord with the observations of Rouse and Dodu (1955), Turner and Kraus (1967), and others, assume that the transfer of fluid during entrainment is always from the nonturbulent into the turbulent fluid. Citing the laboratory work of Turner (1968), it is required, finally, that the entrainment rates for the respective layers are statistically independent.

Consider the special case of a turbulent upper layer entraining quiescent lower layer fluid. The rate of change of mass per unit area per unit time for the upper layer is

$$\frac{\delta M_1}{\delta t} = \rho_2 Q_1 , \qquad (1)$$

where Q_1 represents an as yet unspecified entrainment process for the upper layer. All symbols are defined in Appendix A. Now consider the reverse situation, where the turbulent lower layer entrains quiescent upper layer fluid.

In this case the rate of change of mass per unit area per unit time of upper layer fluid is

$$\frac{\delta M_1}{\delta t} = - \rho_1 Q_2 , \qquad (2)$$

where Q_2 is the lower layer entrainment rate. Clearly the net time rate of change of mass per unit area for the upper layer fluid is

$$\frac{\delta M_1}{\delta t} = \rho_2 Q_1 - \rho_1 Q_2 . \qquad (3)$$

The complete Reynolds' averaged equations representing the time rate of change of mass per unit area per unit time for the upper layer is then

$$(\rho_1 h_1)_t + \vec{\nabla} \cdot (\rho_1 h_1 \vec{v}_1) = \rho_2 Q_1 - \rho_1 Q_2 + \vec{\nabla} \cdot (h_1 K_H \vec{\nabla} \rho_1) , \qquad (4)$$

where K_H is the horizontal diffusion coefficient for heat and $\vec{\nabla}$ is a horizontal operator.

For the lower layer a similar equation applies, viz.

$$(\rho_2 h_2)_t + \vec{\nabla} \cdot (\rho_2 h_2 \vec{v}_2) = \rho_1 Q_2 - \rho_2 Q_1 + \vec{\nabla} \cdot (h_2 K_H \vec{\nabla} \rho_2) . \qquad (5)$$

Note that the total mass in a vertical column comprising both layers can only be changed via horizontal mass flux due to turbulent eddies. No mass gain or loss through the top or bottom of the column has been assumed.

to turbulent eddies. No mass gain or loss through the top or bottom of the column has been assumed.

The change in heat content per unit area per unit time for the upper layer due to entrainment is simply

$$\frac{\delta C_1}{\delta t} = \rho_2 c_p T_2 Q_1 - \rho_1 c_p T_1 Q_2 \, . \qquad (6)$$

where T_1 and T_2 are upper and lower layer temperatures, respectively.

The Reynolds' averaged equations representing the time rate of change of heat content per unit area for the upper layer can be written

$$(\rho_1 h_1 c_p T_1)_t + \vec{\nabla} \cdot (\vec{v}_1 \rho_1 c_p T_1) = \rho_2 c_p T_2 Q_1 - \rho_1 c_p T_1 Q_2 + H + \vec{\nabla} \cdot [h_1 K_H \vec{\nabla}(\rho_1 T_1 c_p)] \, . \qquad (7)$$

A similar equation holds for the lower layer:

$$(\rho_2 h_2 c_p T_2)_t + \vec{\nabla} \cdot (\vec{v}_2 \rho_2 h_2 c_p T_2) = \rho_1 c_p T_1 Q_2 - \rho_2 c_p T_2 Q_1 + \vec{\nabla} \cdot [h_2 K_H \vec{\nabla}(\rho_2 T_2 c_p)] \, , \qquad (8)$$

where H represents a heating function to be specified in the next section. Note that the total heat content for a vertical column including both layers only changes due to heating through the top and through turbulent diffusion of heat through the sides of the column. No heat flux is allowed through the bottom boundary.

Explicit density and continuity equations for each layer can be obtained using Eqs. (4), (5), (7) and (8). At this point it is necessary to assume that for small departures from a reference density ρ_0, the total density can be
this point it is necessary to assume that for small departures from a reference density ρ_0, the total density can be considered a linear function of temperature or apparent temperature. Although salinity is not explicitly included

in this model, it is a simple matter to add this variable to the model – as will be done in future work. Following Fofonoff (1961) and O'Brien (1965), set

$$\rho_1 = \rho_0 - \gamma T_1$$
$$\rho_2 = \rho_0 - \gamma T_2 \,, \tag{9}$$

where γ is the product of the effective coefficient of thermal expansion for sea water and the reference density and T_1 and T_2 represent departures from a reference temperature. Using (9) in (7) and (8) and using (4) and (5), the following set of nonlinear, time-dependent equations for density and layer thicknesses is obtained:

$$(\rho_1)_t + \vec{v}_1 \cdot \nabla\rho_1 = \frac{\Delta\rho Q_1}{h_1} - \frac{\gamma H}{\rho_1 c_p h_1} + \frac{1}{h_1}\vec{\nabla} \cdot (K_H h_1 \vec{\nabla}\rho_1), \tag{10}$$

$$(h_1)_t + \vec{\nabla} \cdot (\vec{v}_1 h_1) = Q_1 - Q_2 + \frac{\gamma H}{\rho_1^{\,2} c_p} \,, \tag{11}$$

$$(\rho_2)_t + \vec{v}_2 \cdot \vec{\nabla}\rho_2 = -\frac{\Delta\rho Q_2}{h_2} + \frac{1}{h_2}\vec{\nabla} \cdot (K_H h_2 \vec{\nabla}\rho_2) \,, \tag{12}$$

$$(h_2)_t + \vec{\nabla} \cdot (\vec{v}_2 h_2) = Q_2 - Q_1 \,, \tag{13}$$

where $\Delta\rho = (\rho_2 - \rho_1)/\rho_1$.

A similar set of equations without horizontal diffusion was used by Johnson (1973) in modeling the seasonal density structure and circulation on the continental shelf.
sion was used by Johnson (1973) in modeling the seasonal density structure and circulation on the continental shelf.
Pike (1971) also derived a set of equations corresponding to (10) through (13) in a study of the ITCZ using an

interacting air-sea model. Hantel (1971) developed a similar, though steady, two-layer system in his investigation of entrainment in a tropical-subtropical β-plane ocean.

At the outset it should be made clear that the modeling is restricted to wind-dominated (forced convective) regimes, in contrast to heat-dominated (free convective) ones. Consequently, this model is unable to explicitly form a new thermocline at a shallower depth under conditions of strong solar heating. No new layers can be added during numerical integrations and the initial wind-mixed layer can only deepen under the influence of mechanical stirring. An initial seasonal thermocline (or third layer) has not been included. Future research may determine the importance of the seasonal thermocline to coastal upwelling processes.

2.2 Momentum equations

In allowing mass transfer across the fluid interface, a mechanism for momentum transfer has also been provided. For the entrainment processes described previously, the net change of momentum per unit area per unit time for the upper layer due to vertical mixing is

$$\frac{\delta M_1}{\delta t} = \vec{v}_2 \rho_2 Q_1 - \vec{v}_1 \rho_1 Q_2 \ , \qquad (14)$$

where $\vec{v}_1 = u_1 \hat{i} + v_1 \hat{j}$. Hence, the vertical transfer of momentum at the interface due to mixing can be expressed by a term representing a source or sink in the momentum equations for each layer. The particular functional form of this term

is governed by the constraint that any parameterization of turbulent mixing processes must lead to a dissipation of the total energy in the fluid system. As indicated in Appendix C, the forms given by (15a) and (15b) below are consistent with this requirement.

The term in the upper layer equation for momentum per unit mass representing this process has the form

$$\vec{S}_1 = \frac{\rho_2 Q_1 (\vec{v}_2 - \vec{v}_1)}{\rho_1 h_1} \quad . \tag{15a}$$

For the lower layer equation the term may be written

$$\vec{S}_2 = - \frac{\rho_1 Q_2 (\vec{v}_2 - \vec{v}_1)}{\rho_2 h_2} \quad . \tag{15b}$$

These forms are similar to those proposed by Niiler (1973) for a model of the deepening of the wind-mixed layer. In previous layered numerical models such as O'Brien and Hurlburt (1972), where momentum but not mass crosses an interface, an interfacial stress was formulated, using energetic arguments, in terms of vertical shears of the horizontal currents. An interfacial stress constant was determined by assuming that the time scale for vertical diffusion was large compared to vertical advection (see Thompson and O'Brien, 1973, for the details). In this new model the additional physical process of vertical mixing must be included in a complete determination of vertical transfers of momentum.

On retaining the first term in the perturbation expression for the advective terms, the vertically integrated momentum equations for the two-layer model are

$$\frac{\partial \vec{v}_1}{\partial t} + \vec{v}_1 \circ \vec{\nabla}\vec{v}_1 + \hat{k} \times f\vec{v}_1 = - g\vec{\nabla}(h_1 + h_2 + D) - \frac{1}{\rho_0} \vec{\nabla} P_A$$

$$- \frac{gh_1}{2\rho_0} \vec{\nabla}\rho_1 + \frac{\vec{\tau}_S - \vec{\tau}_I}{\rho_0 h_1} + \vec{S}_1 + \frac{(\nabla \circ (\rho_1 h_1 A_H \vec{\nabla}))\vec{v}_1}{\rho_0 h_1} , \qquad (16)$$

$$\frac{\partial \vec{v}_2}{\partial t} + \vec{v}_2 \circ \vec{\nabla}\vec{v}_2 + \hat{k} \times f\vec{v}_2 = - g\vec{\nabla}(h_1 + h_2 + D) - \frac{\vec{\nabla}P_A}{\rho_0}$$

$$+ g'\vec{\nabla}h_1 - \frac{gh_1}{\rho_0} \vec{\nabla}\rho_1 - \frac{gh_2}{2\rho_0} \vec{\nabla}\rho_2 + \frac{\vec{\tau}_I - \vec{\tau}_B}{\rho_0 h_2} + \vec{S}_2$$

$$+ \frac{(\vec{\nabla} \circ (\rho_2 h_2 A_H \vec{\nabla}))\ \vec{v}_2}{\rho_0 h_2} , \qquad (17)$$

where

$$\left.\begin{aligned} g' &= g(\rho_2 - \rho_1)/\rho_2 , \\ \vec{\tau}_B &= \rho_0 c_B |\vec{v}_2| \vec{v}_2 , \\ \vec{\tau}_S &= \tau_{Sx}\hat{i} + \tau_{Sy}\hat{j} , \\ \vec{\tau}_I &= \rho_0 c_I q(\vec{v}_1 - \vec{v}_2), \\ q &= |\vec{v}_1 - \vec{v}_2| . \end{aligned}\right\} \qquad (18)$$

The subscript S refers to the surface, I to the interface, and B the bottom. The height of the bottom topography above a reference level is given by D(x,y). The atmospheric pressure is denoted by P_A and A_H represents the

horizontal eddy viscosity. Interfacial and bottom stress coefficients are represented by C_I and C_B, respectively.

The details of the derivation of (16), (17), and (18) are extensive but, in general, easily obtained. Those details will not be discussed here, rather the relevant literature for the interested reader will be cited. The unusual formulation for horizontal momentum transfer due to turbulence is discussed in Appendix B.

Greenspan (1968) carefully discusses the depth-averaged equations governing certain oceanic flows, with special emphasis on nonlinear processes. O'Brien and Reid (1967) derive the barotropic and baroclinic pressure gradient terms in their study of the response of a two-layer ocean to a stationary, axially-symmetric hurricane. Simons (1974) examines the problem of partitioning diffusive fluxes in layered models into horizontal and vertical components and discusses the inadequacies of Laplacian-type forms for turbulent diffusion of momentum in these models.

For generality, no boundary or initial conditions or particular numerical values to any parameters in (16) through (18) in this section will be specified, except in discussing Q_1 and Q_2. At this point note that (10) through (13) plus (16) through (18) form a closed prognostic set of governing equations for the unknowns u_1, u_2, v_1, v_2, ρ_1, ρ_2, h_1, h_2. These equations may be applied to two or three-dimensional equations for the unknowns u_1, u_2, v_1, v_2, ρ_1, ρ_2, h_1, h_2. These equations may be applied to two or three-dimensional models of coastal upwelling. They are nonlinear, time-dependent, and include the effects of earth's rotation, bottom

topography, the atmospheric pressure gradient, solar heating, the effects of horizontal and vertical turbulence including a surface wind stress and interfacial and bottom stresses, and both baroclinic and barotropic modes. In later sections these equations will be specialized to coastal upwelling in an x-z plane.

2.3 Parameterization schemes

In this section a parameterization of the vertical turbulent mixing process based on results from the laboratory, ocean observations, turbulence theory, and physical reasoning will be described. In addition, a form for the surface turbulent heat flux H and for the horizontal diffusivity K_H will be presented.

2.3a Determination of Q_1 and Q_2

Many of the relevant laboratory studies and mathematical models of entrainment processes have been essentially one-dimensional, with the effects of horizontal advection and lateral boundaries ignored or minimized. For a near-boundary problem such as coastal upwelling one reasonably suspects the applicability of certain of these results. Nevertheless, much of the physics will likely remain in the analysis of vertical mixing in a coastal upwelling regime.

Recall that entrainment may arise due to turbulent motions produced by boundary stresses or shear instabilities.

Recall that entrainment may arise due to turbulent motions produced by boundary stresses or shear instabilities.

First consider the case where turbulence is generated by the action of a wind on the sea surface, in which turbulent

energy is fed in on scales much smaller than the depth of the fluid or fluid layers. This corresponds to what Denman (1973) terms the wind-dominated regime.

In the laboratory work of Kato and Phillips (1969) an annular tank was filled with a fluid having a linear density gradient produced by a salt solution. The fluid was subjected to an applied surface stress τ by rotation of a plastic screen placed just under the surface. They found that a turbulent homogeneous layer quickly formed and was bounded below by a sharp interface. In measuring the depth D_1 of the interface, which increased in time at a decreasing rate, they found that the relation

$$Q_1 = u_* f(Ri) , \tag{19}$$

held over a wide range of Ri from 30 to 300. Here

$$\tau = \rho_0 u_*^2$$

$$Ri = \frac{g \left(\frac{\partial \rho}{\partial z}\right)}{2\rho_0 u_*^2} D_1^2 = \frac{g\Delta\rho D_1}{\rho_0 u_*^2} ,$$

and u_* is the friction velocity.

In considering these results, Turner (1973) uses an explicit dimensional argument to obtain a particular form of f(Ri). Part of that argument is reproduced here: Consider that $\Delta\rho$ and Q_1 only appear as the product $\frac{g\Delta\rho}{\rho_0} Q_1$ (the buoyancy flux across the interface). Dimensional sider that $\Delta\rho$ and Q_1 only appear as the product $\frac{g\Delta\rho}{\rho_0} Q_1$ (the buoyancy flux across the interface). Dimensional reasoning gives

$$g\Delta\rho Q_1 D_1 \propto \rho_0 u_*$$

or

$$\frac{Q_1}{u_*} \propto Ri^{-1} .$$

Thus the rate of change of potential energy of the well-mixed layer is proportional to the rate of working of the wind stress. Furthermore, the rate of change of density of the layer is independent of the density difference, for a fixed rate of working. Similar relations between Q_1 and Ri have been obtained or employed by Pollard et al. (1973), Denman (1973), and Niiler (1973). For very large Ri, Fortiscue and Pearson (1967) show that the entrainment is independent of Ri.

Neglecting molecular diffusion, set

$$Q_1 = \phi u_* Ri^{-1} ,$$

or, for the layered model under consideration

$$Q_1 = \frac{\rho_0 \phi u_*^3}{g \Delta\rho h_1} . \qquad (20)$$

It remains to determine the value of ϕ, assumed a constant.

Pike (1971) concluded from the work of Turner (1968) that $\phi = 5$. Johnson (1973) sets $\phi = 2.5$, based on the laboratory work of Kato and Phillips (1969). However, the Kato and Phillips study applied to the range $30 < Ri < 300$. It is common in coastal upwelling regimes to find $Ri < 30$. For example, Huyer (1974) found minimum Richardson numbers < 10

is common in coastal upwelling regimes to find Ri < 30. For example, Huyer (1974) found minimum Richardson numbers < 10

during the July 1072 upwelling off Oregon. To clarify the determination of ϕ consider Denman's (1973) examination of

the wind mixed layer at ocean station PAPA. Using energetic arguments it is found that

$$\phi = 2m \left[\frac{\rho_a}{\rho_0} C_{10}\right]^{1/2} ,$$

where ρ_a is the air density at the sea surface, C_{10} is the drag coefficient, and m represents the fraction of downward flux of turbulent energy of the wind field available as turbulent energy for the mixing in the layer. Values of m can be estimated from the rate of increase of potential energy of the water column calculated from temperature profiles of the upper layer before and after a storm passage. Denman sets m = 0.0012 and finds that realistic solutions for the depth of the mixed layer can only result when values of m differ by less than a factor of 2. Kato and Phillips (1969) find m = 0.0015. In lieu of determining m from hydrographic data in the coastal upwelling area, the value cited by Denman will be used, in which case $\phi = 2.0$.

Shear instabilities may provide turbulent energy for vertical mixing. In this case, at least in the usual hard-limiting view, little transfer of conserved quantities occurs until some physical number exceeds a critical or threshold value, after which turbulence grows rapidly, acting to reduce the number. In this context the local Richardson number is the critical number of interest. Using this approach Pollard
the number. In this context the local Richardson number is the critical number of interest. Using this approach Pollard et al. (1973) show that the kinetic energy released due to

the shear of the mean flow at the interface is important in the initial half-day deepening of the wind-mixed layer.

One might attempt to parameterize the shear instability usually termed Kelvin-Helmholtz instability, produced by large vertical shear due to internal waves, inertial oscillation, baroclinic tides, or shear in the mean wind-driven currents. Such Kelvin-Helmholtz instability has been observed in the atmosphere (i.e., the billow turbulence discussed by Woods, 1968) and is often cited as a possible mechanism for production of clear air turbulence. In the oceanic context Woods and Wiley (1972) have postulated that such turbulence is the primary mechanism for vertical mixing in the ocean.

Entrainment due to shear instability may be expressed, for the upper layer, as

$$Q_1 = H'\left(\frac{1}{4} - R_L\right) \frac{C[(u_1 - u_2)^2 + (v_1 - v_2)^2]^{3/2}}{g'L}$$

where H' is the Heaviside step function, g' is reduced gravity, and L is a vertical length scale, in this case taken to be the distance between midway points in each layer. The scale L is used instead of h_1 since the intensity of the turbulence generated at the interface is not simply dependent on the thickness of the upper layer. Also,

$$R_L = \frac{gL\ \Delta\rho}{\rho_0 \left|\vec{v}_1 - \vec{v}_2\right|}$$

and the properties of the Heaviside step function are

$$H' = \begin{cases} 0 & \text{if } \frac{1}{4} - R_L \leq 0 \\ 1 & \text{if } \frac{1}{4} - R_L > 0. \end{cases}$$

Internal mixing processes of the type represented in (21) have not been studied as intensively as the wind-generated boundary turbulence. Pike (1971), using a related approach, considered R_L always less than one-fourth. Pike chose $C = 10^{-5}$ in order that entrainment due to surface turbulence would be comparable to shear-generated entrainment at low latitudes. For the range of parameters applicable to coastal upwelling situations R_L is rarely below the critical value. Because of the speculative nature of the shear turbulence process described, this process will be omitted from all model runs shown in this paper.

In summary, the entrainment rate Q_1 is a result of two physical processes: turbulent mixing at the interface produced by downward flux of surface turbulence generated by the wind, and turbulent mixing driven by shear instabilities of the Kelvin-Helmholtz type, sometimes termed billow turbulence. For problems in modeling coastal upwelling the former process will be of primary concern.

Parameterization of the lower layer entrainment rate Q_2 is not as straightforward as that for Q_1, particularly since no strong theoretical or observational foundation exists to justify arguments used in the previous discussion. Certainly the shear instability mechanism used in determining

Q_1 may be applied in its identical form for Q_2, i.e.,

$$Q_2 = H' \left(\frac{1}{4} - R_L\right) \frac{C[(u_1 - u_2)^2 + (v_1 - v_2)^2]^{3/2}}{g'L} . \quad (22)$$

The role of bottom boundary turbulent processes analogous to that played by surface generation of turbulence due to the winds is unclear. Several studies have shown that the bottom boundary is important in the production of internal waves due to tidal interaction (Rattray, 1960; Summers and Emery, 1963; Mooers, 1970). There is some evidence for a well-mixed bottom layer over the continental shelf during coastal upwelling (Huyer and Smith, 1972). However, the importance of bottom-generated turbulence in producing substantial vertical mixing, even in shallow water, is not well known. It is reasonable to assume that turbulent kinetic energy generated at the bottom can produce entrainment in a manner analogous to that accomplished by surface turbulence. Thus, we assume that entrainment of warm, upper-layer fluid into the lower layer due to bottom generated turbulence can be expressed as

$$Q_2 = \frac{\rho_0 \phi u_{*2}^3}{g\Delta\rho\, h_2} , \quad (23)$$

where $u_{*2}^2 = \frac{|\vec{\tau}_B|}{\rho_0}$ represents the bottom friction velocity and $|\vec{\tau}_B|$ is determined from (18). Using parameters appropriate to the coastal upwelling area in (23) we find that $Q_2 << Q_1$ except when the interface is very near the bottom. On the seasonal time scale, Johnson (1973) assumes that bottom-generated turbulent mixing due to tides can be significant.

Considering this point, it should be noted that tidal effects are not included in this model. While inclusion of tides would increase the realism of the model, a detailed numerical investigation of tidal effects is beyond the scope of this research.

2.3b Formulation of H

In order to provide bottom boundary conditions for the atmosphere in an interacting air-sea model, it is imperative that sea surface temperatures be predicted accurately. In so doing both long and short-wave radiation absorbed and emitted at the sea surface, and latent and sensible heat fluxes must be determined. In this subsection those processes are parameterized for use in the numerical model.

Clearly, in the real ocean the temperature varies with depth in the uppermost layer due to absorption of short wave solar radiation. However, the largest vertical variations occur in the upper two meters or so, since the absorption of energy with depth decreases exponentially from the surface. Due to wave action, this region is well-mixed and hence the heating can be considered a surface input (Niiler, 1973). In our model it is assumed that the heating is uniformly mixed in the upper layer and that no solar radiation penetrates through the interface.

The net downward heat flux at the sea surface may

tion penetrates through the interface.

The net downward heat flux at the sea surface may

be written as

$$H = R - \varepsilon\sigma T^4 - (H_S + H_L) \tag{24}$$

where $\sigma = 1.355\times10^{-12}$ cal cm^{-1} sec^{-1} $°K^{-4}$ is the Stefan-Boltzman constant. Kraus and Rooth (1961), following Budyko (1956) assume the short-wave radiation R which penetrates the sea surface to be of the form

$$R = 0.94 \ (1 - 0.68n) \ R_0$$

and (25)

$$\varepsilon = 0.985 \ (0.39 - 0.05 \sqrt{e}) \ (1 - cn^2).$$

R_0 is the average clear-sky short-wave radiation, n is cloudiness in tenths and the term $1 - cn^2$ is a correction factor which represents the reduction of outgoing radiation due to clouds. Budyko (1956) cites the value of c for the subtropics as 0.6. The factor 0.94 in R is due to an assumed albedo of 0.06. The surface (ship level) vapor pressure e is expressed in millibars, while H_S and H_L represent sensible and latent heat flux, respectively.

Various formulae have arisen in the literature, primarily based on empirical evidence, which parameterize latent and sensible heat flux in terms of readily measurable quantities. However, as noted by the GARP Joint Organizing Committee (1972) our knowledge of heat and water vapor transfer between ocean and atmosphere is far less satisfactory than that for momentum transfer. With this in mind we assume that. (after Kraus and Rooth, 1961)

that for momentum transfer. With this in mind we assume that. (after Kraus and Rooth, 1961)

$$H_S + H_L = (1 + B) \ L \ K_p \ |\vec{V}_{10}| (1 - r) \ C_w \ ,$$

where B denotes Bowen's ratio, L is the latent heat of evaporation (585 cal g^{-1}), $|\vec{V}_{10}|$ is the wind speed at ship level (10 meters), r is the ratio of vapor pressure e to the saturated value e_w, and K_p is a proportionality constant, taken as 1.5×10^{-9} cm^{-2} sec^2 according to estimates by Budyko (1956), Kraus (1959), and others.

For our simple ocean model H_S, H_L, e, e_w, n, R_0, $\vec{V}_{10}$ and T must be specified. In an interacting air-sea model these quantities will be determined during model integrations, with appropriate consideration made for the diversity of time scales in the air and sea.

2.3c Estimation of turbulent transfers of momentum and heat

It is always a delicate problem to estimate appropriate values of diffusion coefficients for geophysical problems. Indeed, the whole concept of treating macroscale turbulence in a manner analogous to microscale molecular processes, is subject to question. In the absence of a complete theory of turbulence we are forced to account for subgrid scale processes using such artifices. In practice it seems best to minimize the importance of turbulence unless there exists strong evidence to the contrary.

Several variable forms of A_H have been proposed. For example, based on inertial subrange theory, Smagorinsky et al.,

Several variable forms of A_H have been proposed. For example, based on inertial subrange theory, Smagorinsky et al.,
(1965) suggest that

$$A_H = \frac{1}{2}(k_0\Delta x)^2\left|\left(\frac{\partial u}{\partial x}\right)^2 + \left(\frac{\partial v}{\partial x}\right)^2\right|^{1/2}$$

for the two-dimensional model. Here k_0 is von Karman's constant and Δx is the grid spacing. Leith (1968) has discussed a somewhat similar form using two-dimensional turbulence theory. O'Brien (1973) has modified Leith's formulation and obtained the result

$$A_H = c\,(\Delta x)^3 \left|\frac{\partial \zeta}{\partial x}\right|$$

for $\Delta x >> \Delta z$, with c a constant and ζ the vertical component of vorticity. In our model, for lack of a strong reason to do otherwise, we will assume A_H is constant. The estimated numerical value of A_H for upwelling regions has decreased dramatically in recent years. In the early work of Hidaka (1954) and Saito (1956), the width of the upwelling zone was thought to be the width of the lateral viscous boundary layer. To correspond to an assumed 100 km upwelling width A_H was assumed $0(10^8\ cm^2\ sec^{-1})$. As recently as 1971 Garvine, for example, used this value in a steady homogeneous model of upwelling dynamics. It is likely that the width of the upwelling zone is governed by the baroclinic Rossby radius of deformation, not the viscous scale. Stevenson et al. (1973) have discussed from observations of surface drogue motions off Oregon during the upwelling season of 1972 that A_H is $0(10^7\ cm^2\ sec^{-1})$. Recently, Mooers et al. (1973) calculated A_H from observations in the same region to be $1\text{-}5\times10^5\ cm^2\ sec^{-1}$. The numerical coastal upwelling models calculated A_H from observations in the same region to be $1\text{-}5\times10^5\ cm^2\ sec^{-1}$. The numerical coastal upwelling models of O'Brien and Hurlburt (1972), Hurlburt and Thompson (1973), Thompson and O'Brien (1973), and McNider and O'Brien (1973)

have consistently used $A_H = 10^6$ cm^2 sec^{-1}, while Allen (1973) and Pedlosky (1974) have used identical values in their continuously stratified analytical upwelling models. This value is chosen for the work presented in this paper.

The vertical eddy viscosity A_V has not been well estimated in ocean regions. In general, we expect A_V to vary by orders of magnitude with depth, decreasing downward (Kullenburg, 1971). Yet in the upwelling region the minimum Richardson number may occur near the base of the permanent pycnocline (Mooers, 1970) indicating that substantial mixing may occur well below the so-called surface mixed layer. For simplicity of analysis, a depth-independent $A_V = 10^2$ cm^2 sec^{-1} will be employed in obtaining solutions discussed in this paper. For comparison, it is noted that Allen (1973) sets $A_V = 50$ cm^2 sec^{-1}, while Pedlosky and Hsueh and O'Brien (1971) set $A_V = 10^2$ cm^2 sec^{-1}.

For lack of better estimates, it is assumed that turbulent horizontal and vertical Prandtl numbers are 0(1), in which case

$$K_V = A_V \quad \text{and} \quad K_H = A_H.$$

3. MODEL FORMULATION – DEPTH-DEPENDENT EQUATIONS

Obvious mathematical and physical problems arise in modelling a continuous fluid system in terms of vertically averaged equations. Of paramount concern is the clearly unphysical smearing-out of boundary layers in regions of large vertical gradients of density or velocity. These layers can be dynamically important and in some cases here observed in upwelling regions. For example, Halpern (personal communication) found a cum sole deflection of currents in the upper 10 meters of water following the onset of strong northerly winds in the Oregon upwelling regime during July, 1972. Using a high resolution, near-surface current meter string, Halpern observed currents 18.5 km offshore in water 102 m deep before, during, and after the inception of strong northerly winds. (A detailed description of the current meters and the array design may be found in CUE-I Technical Report No. 3, 1973.) Before and after the strong wind period no Ekman-like circulation was noted; during the strong wind period however, a remarkable Ekman-like circulation appeared, as shown in the time-averaged current vector hodographs shown in Fig. 2. It should be noted that contribution to currents due to Stokes drift, estimated from surface wave

graphs shown in Fig. 2. It should be noted that contribution to currents due to Stokes drift, estimated from surface wave measurements, was negligible during all three observing periods.

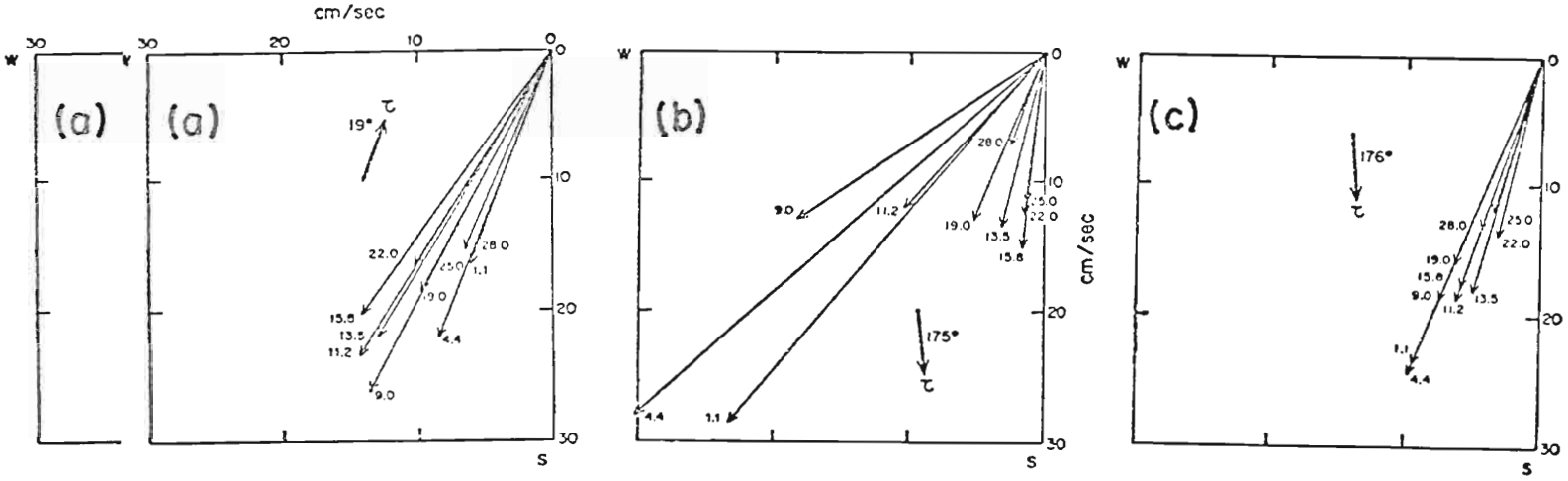

Fig. 2. Near-surface currents obtained during July, 1972 by the Pacific Oceanographic Laboratory Buoy at 44°45.2'N, 124°17.2'W off the Oregon coast (from Halpern, personal communication). Vector-averaged currents were obtained at depths shown beside the arrows. In (a) the ambient flow prior to an upwelling event is shown. In (b) the resultant currents occurring after the onset of the northerly winds suggest an Ekman-type circulation. Following the event, between 18-22 July the Ekman-type circulation was not observed as shown by the current vectors in (c).

As regards the internal shear layers, Csanady (1972) has observed a double Ekman layer of several meters thickness in the sharp thermocline zone of Lake Ontario. This layer was observed during upwelling-favorable conditions and in conjunction with the detection of a near-coast surface jet. Further, an Ekman transport away from shore was noted just below the thermocline.

Finally, there is evidence for the existence of a bottom boundary layer over the continental shelf off Oregon during the upwelling season. According to Huyer and Smith (1972), hydrographic data taken within 20 km of the Oregon coast during June and July, 1972 indicated an extremely well-mixed bottom layer. The top of the layer was clearly defined by a discontinuity in the vertical gradients of both temperature and salinity. Depth of the layer varied from 5 to 15 km. Unfortunately, no current meter data were obtained in this layer.

In this section the dynamical formulation is extended beyond the numerical solution of vertically-averaged equations in order to obtain analytical solutions for the departures of the velocity fields from the vertical mean. In so doing, boundary layers are introduced at the internal and external fluid interfaces. The velocity field in these boundary layers exhibits characteristics of a finite-depth Ekman solution and a thermal wind component arising from boundary layers exhibits characteristics of a finite-depth Ekman solution and a thermal wind component arising from the large horizontal temperature gradient existing in the upwelling zone. The latter component is analogous to the

gravitational circulation observed in estuarine regimes (Hansen and Rattray, 1972). The mass flux into and out of these boundary layers substantially alters any simple upwelling circulation pattern indicated solely by the vertically-averaged equations.

Define a vector quantity $\vec{P}_T$ as

$$\vec{P}_T = \vec{P}(x,y,t) + \vec{P}'(x,y,z,t)$$

where $\vec{P}$ represents the vertical average of the quantity over some specified depth, and $\vec{P}'$ represents the departure from the vertical average over the same depth. Upon subtracting the vertically-averaged equations (16) and (17) from the Navier-Stokes equations representing the total flow at any depth, differentiating the result with respect to the vertical coordinate and employing the hydrostatic relation, we obtain the departure equations for the regions separated by the pycnocline:

$$\frac{\partial}{\partial z}\left[\frac{\partial \vec{v}_j}{\partial t}\right] + \frac{\partial}{\partial z}\left[\vec{v}_j' \cdot \vec{\nabla}(\vec{v}_j + \vec{v}_j') + \vec{v}_j \cdot \vec{\nabla}\vec{v}_j'\right] + \hat{k} \times f \frac{\partial \vec{v}_j'}{\partial z} =$$

$$\frac{1}{\rho_0} g \vec{\nabla}(\rho + \rho')_j + A_H \nabla^2 \left[\frac{\partial \vec{v}_j'}{\partial z}\right] + A_V \frac{\partial^3 \vec{v}_j'}{\partial z^3}, \quad j = 1,2 . \tag{26}$$

Upon introducing scaling parameters appropriate to a coastal upwelling regime, assuming small Rossby number and quasi-equilibrium conditions, the lowest order form of (26) becomes

upwelling regime, assuming small Rossby number and quasi-equilibrium conditions, the lowest order form of (26) becomes

$$\hat{k} \times f \frac{\partial \vec{v}_j'}{\partial z} = \frac{g}{\rho_0} \vec{\nabla}\rho_j + A_V \frac{\partial^3 \vec{v}_j'}{\partial z^3}, \quad j = 1,2 . \tag{27}$$

In obtaining (27) we have assumed that horizontal variations of the perturbation density field are small compared to those of the mean field. A similar equation has been used by Rao and Murty (1973) in studying oceanic fronts and by Bates (1973) in a theory which generalizes the atmospheric CISK mechanism. The effect of the earth's rotation is customarily omitted in models of estuarine circulation (Hansen and Rattray, 1972). The familiar Ekman components of rotation and vertical diffusion are accompanied by a thermal wind term which may be important in regions of large horizontal density gradient, i.e., in upwelling fronts.

It remains to pose a formal mathematical statement of the problem with appropriate boundary conditions. First define

$$w_1 = u_1' + i\, v_1' \quad ,$$

$$w_2 = u_2' + i\, v_2' \quad ,$$

where $i = \sqrt{-1}$. Assume that the sea surface is at $z = 0$, the pycnocline at $z = b$, and the bottom at $z = c$. Upon using w_1 and w_2 in (27), the formal problem becomes

$$\frac{\partial^3 w_1}{\partial z^3} - s^2 \frac{\partial w_1}{\partial z} = G_1, \qquad b \leq z \leq 0 \quad , \tag{28}$$

$$\frac{\partial^3 w_2}{\partial z^3} - s^2 \frac{\partial w_2}{\partial z} = G_2, \qquad c \leq z \leq b \quad , \tag{29}$$

$$\frac{\partial^3 w_2}{\partial z^3} - s^2 \frac{\partial w_2}{\partial z} = G_2, \qquad c \leq z \leq b \quad , \tag{29}$$

with integral constraints

$$\left.\begin{aligned} \int_b^0 w_1 \, dz &= \int_c^b w_2 \, dz = 0 , \\ \text{and boundary conditions,} & \\ \frac{\partial w_1}{\partial z} &= \frac{\tau_{sx}}{A_v} + i \frac{\tau_{sy}}{A_v} = P , \qquad z = 0 , \\ w_1 &= w_2 - \Delta v = J , \qquad z = b , \\ \frac{\partial w_1}{\partial z} &= \frac{\partial w_2}{\partial z} , \qquad z = b , \\ w_2 &= -(u_2 + i v_2) = K , \qquad z = c . \end{aligned}\right\} \quad (30)$$

The symbols τ_{sx} and τ_{sy} refer to the surface wind stress in the x and y directions, respectively. Also,

$$\left.\begin{aligned} G_j &= -\frac{g}{\rho_0 A_v}\left[\frac{\partial \rho_j}{\partial x} + i \frac{\partial \rho_j}{\partial y}\right] , \qquad j = 1,2 \\ s &= (1 + i) r \\ r &= \left(\frac{f}{2A_v}\right)^{1/2} \end{aligned}\right\} \quad (31)$$

and

$$\Delta v = u_1 - u_2 + i(v_1 - v_2).$$

The boundary conditions at z = b match both stress and velocity across the pycnocline while at z = c a no-slip condition is applied to the total flow. Note that (27) and (28) are directly coupled through the matching conditions at the pycnocline.

The details involved in solving (27) through (31) are straightforward though extensive and are provided in Appendix D. It will suffice here to write down the resulting solution in compact form. For the upper region

$$w_1 = \frac{A_1 e^{sz}}{s} - \frac{B_1 e^{-sz}}{s} - \frac{G_1 z}{s^2} + C_1 \quad , \tag{32}$$

where

$$\left.\begin{aligned} A_1 &= P - B + \frac{G_1}{s^2} \ , \\ B_1 &= P e^{sb} - Q + \frac{G_1}{s^2}\left(e^{sb} - 1\right) \ , \\ C_1 &= \frac{1}{b}\left[\frac{A_1}{s^2}\left(1 - e^{sb}\right) + \frac{B_1}{s^2}\left(1 - e^{-sb}\right) + \frac{G_1 b^2}{2s^2}\right], \end{aligned}\right\} \tag{33}$$

and

$$Q = \frac{Y - \varepsilon R - \varepsilon \Delta v}{1 + \varepsilon \eta} \quad .$$

Also,

$$Y = \frac{X + \left[\mu s K \gamma_1 \gamma_3 + \mu s \alpha_1 K - \dfrac{\mu G_2(\alpha_1 \gamma_3 - \alpha_3 \gamma_1)}{s}\right]}{\alpha_1 \gamma_2 - \alpha_2 \gamma_1} \tag{34}$$

$$\varepsilon = \frac{\mu s \alpha_1}{\alpha_1 \gamma_2 - \alpha_2 \gamma_1} \ ,$$

$$\mu = \frac{\alpha_2}{\alpha_1} e^{sb} + e^{-sb} \ ,$$

$$X = \frac{K \gamma_3 \, s e^{sb}}{\alpha_1} + \frac{G_2 \alpha_3 \, e^{sb}}{s \alpha_1} - \frac{G_2}{s^2}$$

$$\alpha_1 = e^{sc} \gamma_3 - \frac{\gamma_1}{s} \ ,$$

$$\alpha_2 = e^{-sc} \gamma_3 + \frac{\gamma_2}{s}$$

$$\alpha_3 = \frac{(\gamma_3)^2}{2} ,$$

$$\gamma_1 = e^{sb} - e^{sc} ,$$

$$\gamma_2 = e^{-sb} - e^{-sc}$$

and

$$\gamma_3 = b - c .$$

For the lower region

$$w_2 = \frac{A_2 e^{sz}}{s} - \frac{B_2 e^{-sz}}{s} - \frac{G_2 z}{s^2} + C_2 , \tag{35}$$

where

$$\left.\begin{aligned} A_2 &= \left[K\gamma_3 + \frac{G_2\alpha_3}{s^2} + \frac{B_2\alpha_2}{s}\right] \frac{s}{\alpha_1} , \\ B_2 &= s\left[\frac{K\gamma_1\gamma_3 - \alpha_1 (J - K) - \frac{G_1}{s^2} (\alpha_1\gamma_3 - \alpha_3\gamma_1)}{\alpha_1\gamma_2 - \alpha_2\gamma_1}\right] \\ C_2 &= J - \frac{A_2 e^{sb}}{s} + \frac{B_2 e^{-sb}}{s} + \frac{G_2 b}{s^2} , \end{aligned}\right\} \tag{36}$$

and

$$J = \frac{R + (Y - \varepsilon R - \varepsilon\Delta v)\eta}{1 + \varepsilon\eta} .$$

Also,

$$\left.\begin{aligned} R &= \frac{P_1\delta_1}{s} + \frac{G_1\delta_3}{s^2} , \\ \eta &= \frac{1}{s}\left[\coth sb - \frac{1}{sb}\right] , \\ \delta_3 &= e^{sb} (1 - \coth sb) + \frac{1}{sb} . \\ \eta &= \frac{1}{s}\left[\coth sb - \frac{1}{sb}\right] , \\ \delta_1 &= e^{sb} (1 - \coth sb) + \frac{1}{sb} , \\ \delta_2 &= \coth sb - \frac{1}{sb} , \end{aligned}\right\} \tag{37}$$

$$\delta_3 = \frac{e^{sb}}{s}(1 - \coth sb) + \frac{\coth sb}{s} - \frac{b}{2} \quad , \qquad (37)$$

$$\lambda_1 = e^{sb} + \frac{(1 - e^{sb})}{sb} \quad ,$$

and

$$\lambda_2 = -\frac{(1 - e^{-sb})}{sb} + e^{-sb} \quad .$$

Even upon separating the real and imaginary components in (32) and (35) the form of the solutions is not very useful for analyzing flow dynamics. A more fruitful approach is to examine model cases in Section 5. In that section results of the combined analytical and numerical model provide a continuous profile for u, v, and, through mass continuity, w at each grid point.

For negligible horizontal density gradients and a thick upper layer during early spinup (32) and (35) produce the familiar Ekman spiral hodograph with the surface current directed 45 degrees to the right of the surface wind stress.

4. MODEL FORMULATION – NUMERICAL DESIGN

The highly efficient semi-implicit numerical scheme developed by Kwizak and Robert (1971) for atmospheric models and extended to the ocean case by O'Brien and Hurlburt (1972) is modified for use in the present model. When used with an unusual telescoping grid system the efficiency of this model over the usual explicit, ordinary grid model is increased by at least two orders of magnitude with no sacrifice of accuracy. Initial and boundary conditions are discussed in terms of actual ocean conditions. Choice of initial layer depths, densities, and necessary constants are justified in light of observations. The formulation of far field boundary conditions are discussed in detail.

4.1 Semi-implicit numerical scheme

In a landmark paper Kwizak and Robert (1971) demonstrated that the ordinary Courant-Friedrich-Lewy condition governing the maximum time step allowed in a numerical model could be relaxed if an implicit treatment of the physics governing the fastest moving waves in the system were employed. O'Brien and Hurlburt (1971) used an implicit scheme in treating both the external and internal gravity wave modes in an f-plane numerical model of coastal upwelling. In the present paper their treatment has been

extended to accomodate spatial and temporal variations in the density field on a nonuniform grid.

When the free surface and internal waves are treated implicitly in the two-layer x, t model one obtains coupled Helmholtz equations for the vertically-averaged zonal flow u_1 and u_2 or the layer thickness h_1 and h_2. We choose to solve for the former variables in a model with physical lateral boundaries. The appropriate time-differenced equations are written

$$u_{2j}^{n+1} - b' \left[\frac{\partial^2 u_2}{\partial x^2}\right]_j^{n+1} + (c'-a') \left[\frac{\partial^2 u_1}{\partial x^2}\right]_j^{n+1} = d , \qquad (38)$$

$$-u_{1j}^{n+1} + u_{2j}^{n+1} + c' \left[\frac{\partial^2 u_1}{\partial x^2}\right]_j^{n+1} = e . \qquad (39)$$

where d and e are known functions, $a' = gH_1\Delta t^2$, $b' = g(H_2+D)\Delta t^2$, $c' = g'H_1\Delta t^2$, and H_1 and H_2 refer to initial upper and lower layer depths, respectively. The time step is represented by Δt. In the original model the coefficients in (38) and (39) were constant in space and time. In the present work the stratification varies in space and time due to vertical mixing and solar heating. Therefore, when we replace the spatial derivatives with second-order finite differences and solve (38) and (39) interatively using the tridiagonal variant of Gaussian elimination we must account for different c' values at each grid point. The most efficient procedure is to sub-
Gaussian elimination we must account for different c' values at each grid point. The most efficient procedure is to sub-tract (38) from (39) and obtain a new equation which has constant coefficients, then use that equation iteratively

with (39). This approach enables us to use efficiently the forward scan feature of Gaussian elimination in the equation containing constant coefficients.

To indicate the dramatic increase in computational efficiency introduced by the semi-implicit method, we have calculated the ratio of the time steps required for an explicit model (Δt_{ex}) with a free surface compared to a semi-implicit scheme (Δt_{si}) that treats free surface and internal waves implicitly. For typical model parameters,

$$\frac{\Delta t_{ex}}{\Delta t_{si}} = \frac{[g(H_1 + H_2)]^{1/2}}{\bar{u}} \approx 400 ,$$

where $\bar{u}$ represents the maximum advective speed. In practice the computational efficiency is reduced by the additional time required in iterative operations. The actual efficiency increase due to the semi-implicit scheme is about 50 for the model described in this paper. Accuracy is not noticeably different in the two methods.

4.2 Discrete variation telescopic grid

The region of interest in this paper is the coastal upwelling zone of offshore length scale 0(10-100 km). Features of interest within this zone have length scales 0(1-10 km). However, Hurlburt and Thompson (1973), Garvine (1974), and others have shown that realistic solutions in the upwelling zone can only be obtained when the ocean interior solution is included, in which case a model basin

0(1000 km) is required. Only in such a wide basin can a realistic Sverdrup interior and westward-propagating Rossby waves exist. Clearly we require high spatial resolution in the upwelling zone and would be satisfied with lower resolution elsewhere. Consequently, a variable grid system is appropriate. An unusual discrete variation telescoping grid has been designed for this purpose.

The essence of the discrete variation telescoping grid system for a single layer x-t model is shown in the schematic diagram of Fig. 3. In this case three different grid intervals are indicated. Imagine a basin bounded zonally by rigid vertical walls. At a given time the zonal flow field is solved semi-implicitly on the greatest grid scale Δx_1 across the entire model basin, using the appropriate boundary conditions at the physical boundaries. Next, the forecast value for u at the Δx grid point labeled "computational boundary (Grid 2)" is used as a boundary condition for solution of the equations on the next finest resolution grid (Δx_2) at the same time step. Then the zonal flow at each grid point on the Δx_2 scale is calculated. Those previously calculated u values on grid points of the Δx_1 grid coincident with Δx_2 points are ignored. Finally, the entire procedure is repeated for the Δx_3 high resolution grid.

The remaining variables are calculated at each grid grid.

The remaining variables are calculated at each grid point using ordinary finite difference techniques. All spatial derivatives at grid points separating grid intervals of

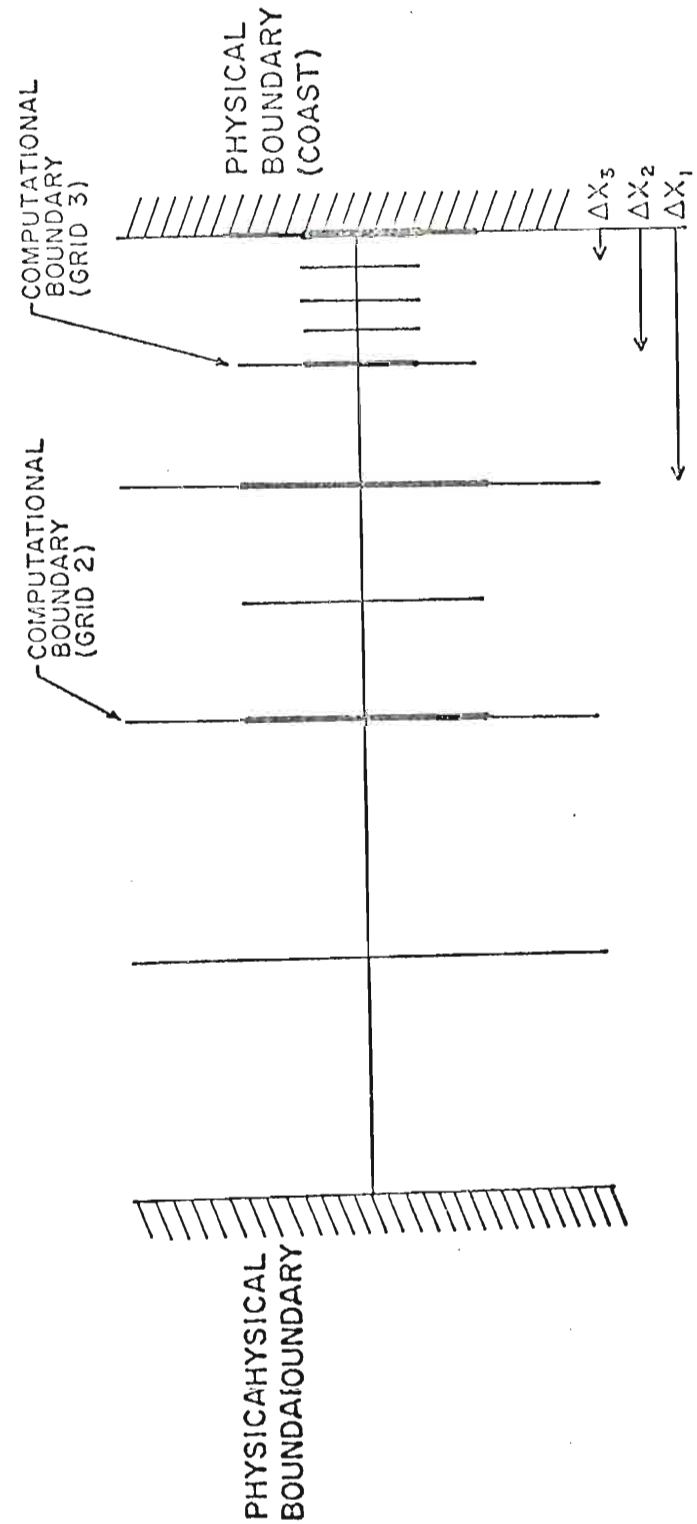

Fig. 3. Schematic diagram of the discrete variation telescoping grid system.

differing lengths are calculated on the larger grid mesh. No interpolations are necessary since we require all grid intervals to be integral multiples of the finest grid length.

Substantial effort has been invested in testing the telescoping grid system. Many different model runs 0(50) were made in comparing solutions from the telescoping grid with those from the constant interval grid. Results from one of the most severe tests are summarized in Table 1. All details of these test models need not concern us here. The two runs are identical except that in the telescoping grid case Δx_1 = 48 km, Δx_2 = 6 km, and Δx_3 = 2 km, with each grid containing 24 grid points for a total model width of 1344 km. The ordinary grid case contains 600 interior grid points with a uniform grid interval of 2 km. In this case H_1 = 50 m, H_2 = 150 m, g' = 2 cm sec^{-2}, D is 140 m at the eastern coast and decays linearly to zero at 100 km. All additional constants and boundary conditions are standard and are provided in the next sub-section. The models were started from rest on a β-plane.

The comparison shown in Table 1 originates at day 9 in the model integrations. Of particular note is the extremely good agreement in velocity and height fields in the nearest 20 km of the coast. In general, differences between solutions are less than one per cent. The comparison of upper layer depths is important since the time history of

Table 1. Comparison data from telescoping and ordinary grid models at day 9

Distance from coast (km) \ Variable	u_1 (cm/sec)	u_2 (cm/sec)	v_1 (cm/sec)	v_2 (cm/sec)	h_1 (cm)
6	-1.627	.7399	-48.53	-5.722	2104
	-1.623	.7566	-48.63	-5.958	2108
10	-1.660	1.084	-48.62	-11.47	2942
	-1.632	1.124	-48.76	-11.67	2943
20	-1.507	1.422	-32.84	-16.96	4276
	-1.515	1.443	-33.01	-17.14	4276
104	-1.084	.379	1.159	1.867	4963
	-1.114	.364	1.140	1.876	4963
240	-1.200	.452	-1.280	-1.298	4994
	-1.172	.395	-.828	-.884	4993
960	-.1366	.003	-1.146	-1.216	5070
	-.109	.084	-1.561	-1.514	5088
960	-.109	.084	-1.561	-1.514	5088

the zonal flow is partially represented by this value. Thus, although the velocity fields between model runs differ significantly at 240 km offshore due to phase errors introduced by the telescoping grid, the layer thicknesses are virtually identical for the two cases.

The telescoping grid model ran 9 days in 183 sec using a half-hour time step on the CDC 6500. With the same time step the ordinary grid semi-implicit model ran the 9 days in 1200 sec. The telescoping system increased numerical efficiency by at least a factor of five in every case studied. Accuracy degradation was not significant in the near coast solutions using the telescoping grid.

From this research the following remarkable conclusion can be drawn: running the discrete variation telescoping grid model with semi-implicit on the CDC 6500 for 1 minute is equivalent to running the ordinary grid, explicit model with similar near-coast resolution for 6 hours.

With slight modification the present model can provide high resolution at both coastal boundaries simultaneously. Further, as many as five changes in grid interval can be accomplished across the channel.

In the actual numerical solutions the zonal flow is determined using the x-directed momentum equations while the longshore flow is determined from a vorticity equation for each laver. Formation of a vorticity equation allows us to longshore flow is determined from a vorticity equation for each layer. Formation of a vorticity equation allows us to retain the barotropic and baroclinic longshore pressure

gradients so long as we assume longshore derivatives of the velocity and density field are small. This procedure is discussed in detail by Hurlburt and Thompson (1973) and follows an approach similar to that used by Veronis and Stommel (1956). The reader is urged to consult those papers for the details. As an aside, Hurlburt (1974) has shown from results of his x-y-t two-layer hydrodynamical model that for a long straight north-south coastline the assumption of small longshore derivatives in the velocity field is excellent. Indeed, the solutions obtained from a purely hydrodynamical version of this model are virtually identical to those obtained in the x-y-t model with a long straight N-S coastline.

The nonlinear advective terms are treated using quadratic averaging (scheme F from Grammeltvedt, 1969). The Coriolis terms are centered-in-time while the diffusive terms are lagged in time. The vorticity equations are integrated from an outer boundary region toward the coast. Planetary vorticity advection βv is treated implicitly using the trapezoidal rule in space and time.

Because a leap-frog time differencing scheme was employed, time-splitting computational modes were present in the numerical solutions. Though the amplitudes of these modes were small, they were reduced by an order of magnitude using a forward time difference at the initial time. Other methods, such as averaging solutions over time

tude using a forward time difference at the initial time. Other methods, such as averaging solutions over time

(Orlanski and Ross, 1973) have been employed to eliminate this problem, but for our work the forward time-difference

method was found most satisfactory. This method was also used during the integrations when the time step was changed (see below).

During the course of the integrations the interface between layers rises near the coast as the coastal upwelling proceeds. In previous numerical models the integrations were terminated when the interface reached the sea surface, usually within a week under strong wind forcing. Theoretically, in the present model the interface cannot intersect the sea surface due to the vertical mixing included in the formulation. Nevertheless, the interface may, in certain instances, rise to within several meters of the surface. If one uses a large Δt, the vertical motion of the interface $0\ (10^{-3} - 10^{-1}$ cm $\text{sec}^{-1})$ may be large enough so that a negative interfacial depth is predicted for the next time level. Consequently, when the pycnocline is near the sea surface, a higher time resolution is required in order to prevent surfacing. This is a CFL-like condition governing the time step. In this case, since we have no vertically-propagating waves the restriction arises from the motion of the fluid interface itself. This interesting result leads to the following time-step restriction for layered models, i.e.,

$$\Delta t \leq \frac{h_m}{2w_I} ,$$

$$\Delta t \leq \frac{h_m}{2w_I} ,$$

where h_m is the thickness of the layer and w_I is the magnitude of the vertical velocity of the interface. Such a

restriction is somewhat different from usual CFL conditions in that h_m is determined during the course of the integrations.

In order to avoid numerical instability when the above condition is violated we have allowed the time step to vary during the integrations. Typically the model proceeds with a large time step until the interface reaches a predetermined minimum depth. At that point the model is stopped and restarted with a smaller Δt, using a forward difference during the restart procedure. This method has proven quite satisfactory during extensive testing runs. Larger Δt can be reintroduced at a later time using the same restart strategy.

4.3 Initial and boundary conditions

The initial conditions for all model runs discussed are a state of rest for the velocity field, spatially homogeneous layer densities, and constant layer thicknesses. The rest initialization is justified by noting that the shallow shelf region responds quickly to the wind-driving, and hence the spin-up process is an actual feature of the coastal upwelling cycle. Since we are interested in modelling the upper ocean layers the ocean interior is assumed quite shallow, possessing low inertia and having a short spin-up time scale. We are mindful of the important abyssal

quite shallow, possessing low inertia and having a short spin-up time scale. We are mindful of the important abyssal

circulations that do exist in the ocean, but for the

investigations cited in this paper that circulation is not explicitly included.

It is possible to develop a quasi-balanced initialization for the model in order to remove large amplitude inertial and Rossby wave modes (Hurlburt, 1974) generated by the impulsive starting of the wind stress and wind stress curl, respectively. For the purpose of our model a slow spin-up is introduced by driving the system with a wind stress which linearly increased in magnitude from zero at the initial time to 1 dyne cm^{-2} at day one. Only the longshore component of wind stress is included in model runs presented. The stress is held constant until the end of an event, at which time the model is spun-down. In spin-down the winds decay over a one day period and then integrations are continued for a suitable additional period.

The particular choice of layer thicknesses is somewhat arbitrary since the base of the well-mixed layer is sometimes ill-defined in the coastal upwelling hydrography. One may follow the convention of assigning the 25.5-26.0 sigma-t band of water as delineating the region of the permanent pycnocline off Oregon (Pillsbury, 1972). In that case the ten year average pycnocline depth for January and February ranges from 80-120 m in the mid-latitude eastern ocean (Halpern, 1973). In spring and early summer that depth decreases to 50-100 m. We have chosen the 50 m
eastern ocean (Halpern, 1973). In spring and early summer that depth decreases to 50-100 m. We have chosen the 50 m initial pre-upwelling condition near the coast in early summer.

The lower layer depth, 150 m for the flat bottom case, is chosen under the assumption that the primary circulations occur above a 200 m deep depth of no motion. Yoshida (1967) explicitly includes a resting bottom layer in his upwelling model, as does O'Brien and Reid (1967) for an interacting hurricane-ocean model. However, model experiments with much deeper lower layers have not shown significant qualitative differences from the model cases described here. Of course over the continental shelf the fluid depth may be much less than 200 m.

The initial density (and temperature) values for each layer are specified using hydrographic data from CUE-I. The initial upper layer density is taken as 1.024 gm cm^{-3}, the lower layer density 1.026 gm cm^{-3}. The initial density contrast is identical to that used in the previous numerical models of O'Brien and Hurlburt (1972), Thompson and O'Brien (1973), and Hurlburt and Thompson (1973). The reference density ρ_0 = 1.0285 gm cm^{-3} corresponds to cold saline water. Upon determining a coefficient of thermal expansion appropriate to a linear equation of state relating density and temperature, the upper layer mean temperature is approximately 16.5°C and the lower layer temperature is just above 9°C. All pertinent parameters are listed in Table 2.

The no-slip and kinematic conditions are applied to the vertically-averaged horizontal velocity at the coast and

The no-slip and kinematic conditions are applied to the vertically-averaged horizontal velocity at the coast and far boundary. Thus the horizontal flow vanishes there. At

Table 2. Constants and scaling parameters of the model.

Parameter	Value	Parameter	Value
f	10^{-4} sec^{-1}	τ_{sy} (max)	-1 dyne cm^{-2}
g	10^{3} cm sec^{-2}	H_1	5×10^{3} cm
g' (initial)	2 cm sec^{-2}	H_2	15×10^{3} cm
A_H, K_H	10^{6} cm^2 sec^{-1}	L	3100 km
A_v, K_v	10^{2} cm^2 sec^{-1}	β	2×10^{-3} cm^{-1} sec^{-1}
ρ_0	1.0285 gm cm^{-3}	Δx	variable
c_I	10^{-5}	Δt	variable
c_B	10^{-3}	c_p	1 cal gm^{-1} °K^{-1}
ρ_1 (initial)	1.024 gm cm^{-3}	ϕ	2
ρ_2 (initial)	1.026 gm cm^{-3}	γ	2.67×10^{-4} K^{-1}
τ_{sx}	0		

the far boundary where no wind forcing is applied, an additional boundary condition on the long-shore flow is required to close the problem since the vorticity equations contain a third order diffusion term.

Note that at the far boundary the y-momentum equations for vertically-averaged flow reduce to

$$\left.\begin{aligned} &- g \frac{\partial}{\partial y} (h_1 + h_2 + D) + \frac{\tau_{sy}}{\rho h_1} + \vec{\nabla} \cdot (\rho_1 h_1 A_H \vec{\nabla}) v_1 = 0 , \\ &- g \frac{\partial}{\partial y} (h_1 + h_2 + D) + \frac{\partial h_1}{\partial y} + \vec{\nabla} \cdot (\rho_1 h_1 A_H \vec{\nabla}) v_1 = 0 , \\ &- g \frac{\partial}{\partial y} (h_1 + h_2 + D) + g' \frac{\partial h_1}{\partial y} + \vec{\nabla} \cdot (\rho_2 h_2 A_H \vec{\nabla}) v_2 = 0 . \end{aligned}\right\}$$

These equations yield the additional boundary condition

required, if two of the three terms in each equation are independently specified. In this model we will require that the wind stress and the N-S sea surface and interfacial slopes vanish at the far boundary. These restrictions preclude the possibility of western intensification in the model. Nevertheless, the solutions in the upwelling zone are little affected by the particular form of the boundary conditions imposed in the far field. This results, originally discovered in the hydrodynamic model of Hurlburt and Thompson (1973), is of extreme importance to the present work. It is possible to balance diffusion of longshore momentum with the sea surface slope and wind-stress terms in order to obtain a realistic western intensification. Yet, when this is accomplished the solution in the upwelling zone is almost identical to the case without western intensification. In short, regardless of the wind stress and N-S pressure gradient imposed at the western boundary, any initial imbalance results in western boundary currents and Rossby waves such that, for a sufficiently wide basin, the eastern ocean circulation is little affected. For a closed, three-dimensional basin the results may be quite different.

Finally, no heat or mass flux is allowed across the sea bottom or across lateral boundaries. Heat flux will be allowed across the sea surface in the heating model discussed in Section 5.3. In that case short wave and long wave radia-
allowed across the sea surface in the heating model discussed in Section 5.3. In that case short wave and long wave radia-
tion will be included using the extremely simple parameterization scheme discussed earlier.

5. MODEL RESULTS – CASE STUDIES

In this section we present results from several model runs, each chosen to investigate particular aspects of the coastal upwelling problem. The simple two-cell circulation, the coastal jet and undercurrent, and frontogenesis and frontolysis are studied using flat bottom and continental shelf wind-driven models with and without radiative fluxes at the sea surface. Both a simple time-varying wind, designated the event forcing, and continuous wind forcing are applied. Results from all model runs are subsequently compared with actual, though sparse, observations. Our goal is to unravel basic dynamical balances, rather than to simply observe the numerical results.

5.1 The flat bottom model

Consider a 200 m deep ocean with a flat bottom. The vertical lateral walls bound a two-layer fluid of 3100 km zonal extent. The model is started from rest, forced by a longshore wind stress whose spatial variation is shown in Fig. 4a. The wind provides a constant -1 dyne cm^{-2} stress out to 300 km. It decays linearly out to 2300 km, resulting in a realistic (O'Brien, 1972) large-scale wind stress curl of 5×10^{-9} dyne cm^{-3}. The zonal wind component remains zero for all time. Temporal variations of wind stress are shown

in a realistic (O'Brien, 1972) large-scale wind stress curl of 5×10^{-9} dyne cm^{-3}. The zonal wind component remains zero

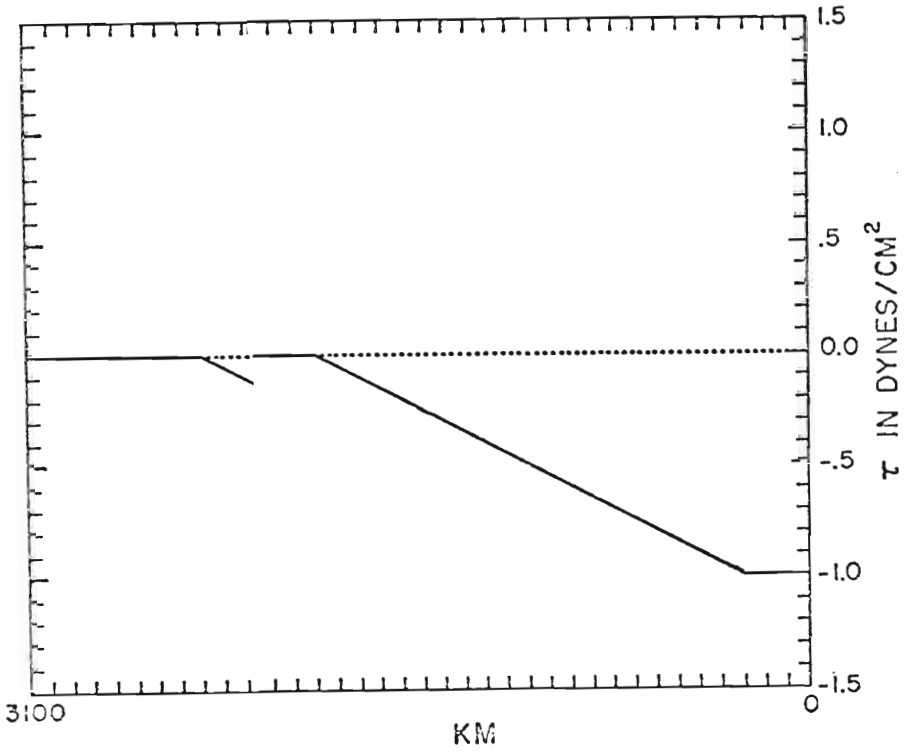

(a)

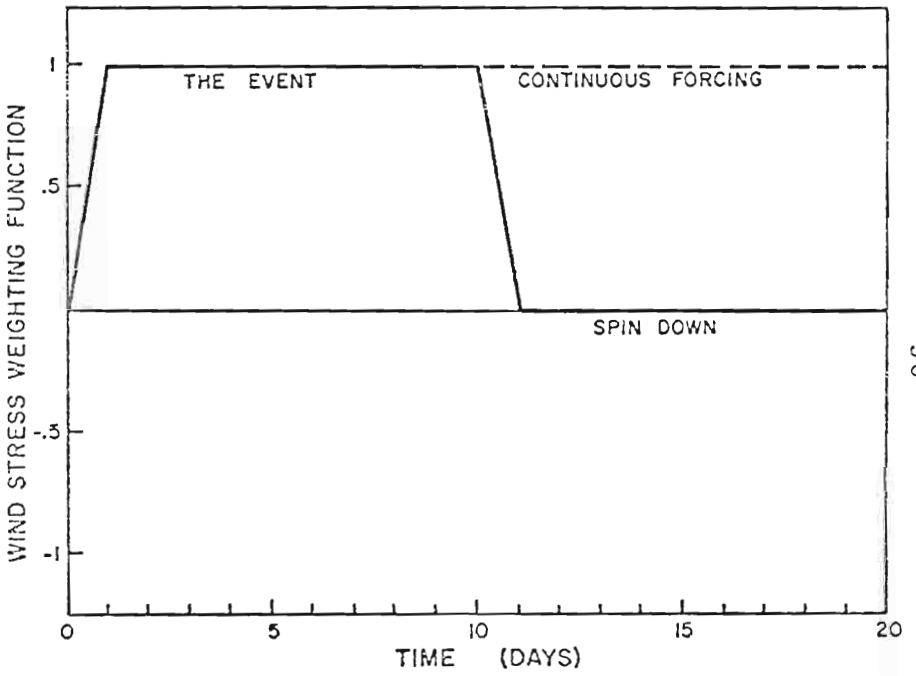

(b)

Fig. 4. The spatial distribution of the wind stress is shown in (a): τ_{sy} (solid) is -1.0 dyne cm^{-2} near the coast; τ_{sx} (dashed) is zero everywhere. In (b) the temporal variation of the wind stress weighting function is indicated.

in Fig. 4b. The wind stress magnitude linearly increases from day 0 to day 1, remains constant to day 10, then decays linearly to zero at day 11. This represents the characteristic wind forcing that sometimes accompanies an upwelling event. Note that a continuous forcing to day 20 (and beyond) is also represented.

In the simplest view, as the winds blow, one-sided divergence at the coast requires subsurface replacement water. The rising near-coast water can be traced rather well by the interface, though in this mixing model the interface is permeable to vertical mass flux. Fig. 5a shows the deviation of the interface from the initial depth (height anomaly) at day 5, 10, and 15 for the event case. Upwelling at the coast has forced the interface upward 27 m in the first five days. Before day 10, when the winds begin to decay, the interface has begun its descent, as noted in the x-t sections of height anomaly in Fig. 5b. The interface does not continue to rise during strong forcing due to the downward flux of surface turbulent energy, which deepens the mixed layer and overcomes vertical advection. Stratification near the coast decreases as deeper, colder water is entrained into the turbulent surface layer. As stratification decreases surface turbulence acts more effectively to deepen the mixed layer.

The upper layer has deepened slightly by day 10 far offshore. Nearshore the upwelling proceeds on a width scale

The upper layer has deepened slightly by day 10 far offshore. Nearshore the upwelling proceeds on a width scale comparable to the baroclinic Rossby radius of deformation

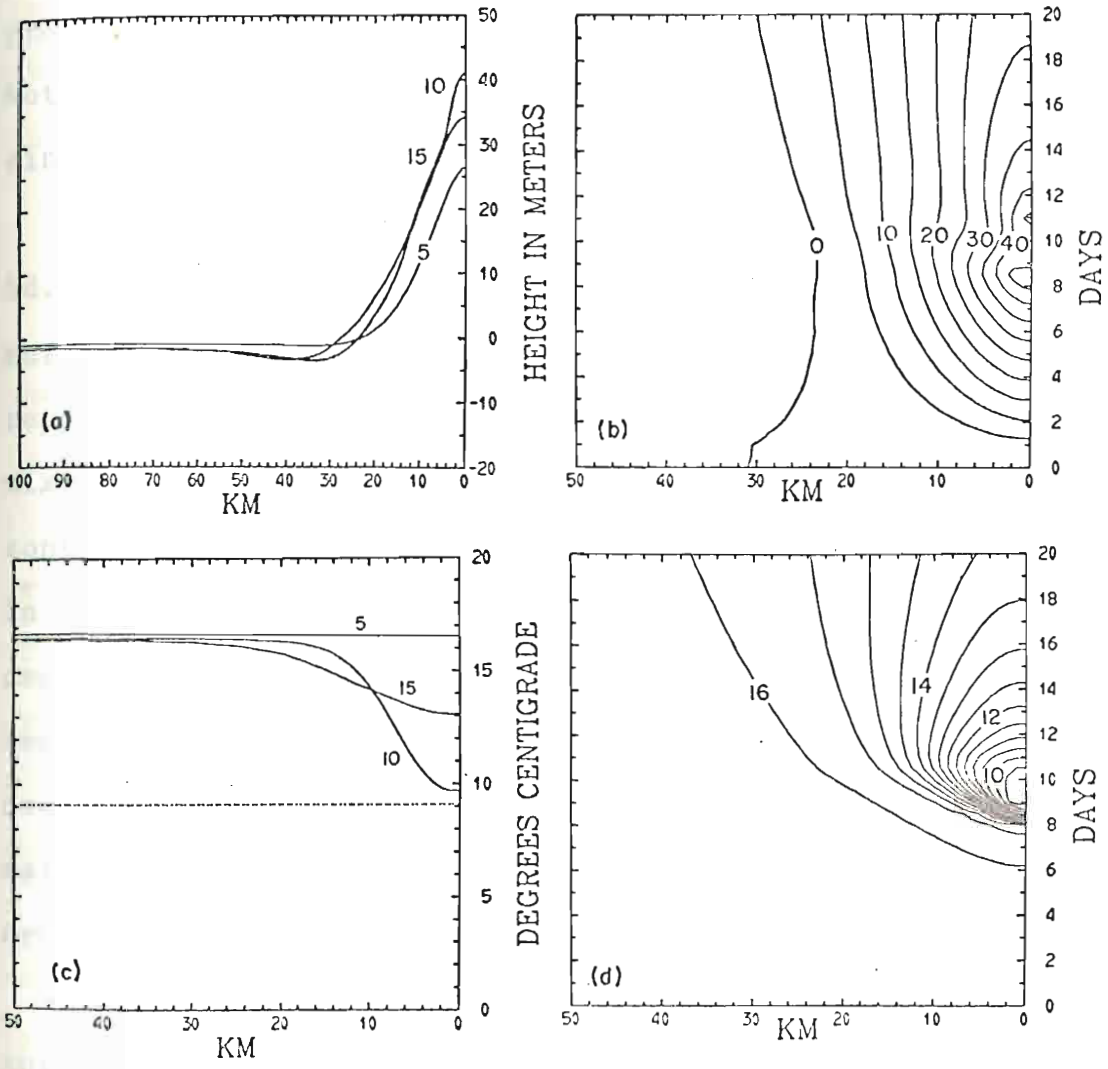

Fig. 5. (a) The interfacial height anomaly versus distance offshore for day 5, 10, and 15 for the flat bottom event case. (b) The x-t section of interfacial height anomaly for the same case. (c) and (d), respectively, represent similar diagrams for the upper layer temperature.

the flat bottom event case. (b) The x-t section of interfacial height anomaly for the same case. (c) and (d), respectively, represent similar diagrams for the upper layer temperature.

$$\lambda = \left[\frac{g' H_1 H_2}{f^2 (H_1 + H_2)}\right]^{1/2} .$$

Indeed, a simple application of the principle of conservation of potential vorticity requires an interface with exponential shape whose e-folding length is precisely λ. Note that for this model λ is a function of time and space, since g' depends on stratification.

The temperature field is represented in Fig. 5c and 5d. The major feature is the very rapid lowering of sea-surface temperatures (henceforth abbreviated SST and assumed representative of the mixed-layer temperature) during intense mixing. Fig. 5c indicates the formation of a marked horizontal temperature gradient (front) by day 10. As evidenced in Fig. 5d, this front begins to decay immediately after cessation of the winds. Further, the position of maximum temperature gradient appears to move offshore until wind decay, at which time it becomes quasi-stationary approximately 10 km offshore. Note that the water temperature drops 5°C in less than one day very near the coast.

The primary mechanism active in producing a strong surface front is the highly nonlinear, concerted action of vertical turbulence and vertical advection. As cold water is brought near the surface, vertical mixing acts to entrain cold water upward, decreasing the bulk stratification. From equation (11) we see that decreased stratification enhances the effect of vertical mixing in deepening the layer.

Finally, horizontal diffusion and advection of heat balances vertical advection and upward entrainment of cold subsurface water, resulting in a quasi-balanced mixed-layer depth. For no radiative inputs, ignoring horizontal advection, and using the Rossby radius of deformation as the appropriate horizontal length scale, equation (10) can be used to estimate the equilibrium depth

$$h_1 \simeq \left[\frac{\rho_0 \phi u_*^3 \lambda^2}{g K_H \Delta\rho}\right]^{1/2} = \left[\frac{\phi u_*^3 H_1 H_2}{K_H f^2 (H_1 + H_2)}\right]^{1/2}$$

where $\Delta\rho$ is the density contrast between the two layers. It is not surprising that increased surface turbulence increases the equilibrium depth and increased horizontal mixing decreases it. Note that the equilibrium depth is independent of the bulk stratification. We conclude that even under intense upwelling it may be possible to locate a definable pycnocline very near the sea surface. For parameters appropriate to our model the equilibrium depth is 0(10 m).

The vertically-averaged horizontal velocity components for four selected days are shown in Fig. 6. From these four snapshots numerous features of the basic dynamics can be elucidated. For example, in Fig. 6a, at day 5, the equatorward surface jet and the poleward undercurrent are both clearly in evidence. We will not recount in detail the dynamical basis for these currents since thev are discussed

clearly in evidence. We will not recount in detail the

dynamical basis for these currents since they are discussed by O'Brien and Hurlburt (1971) and Hurlburt and Thompson

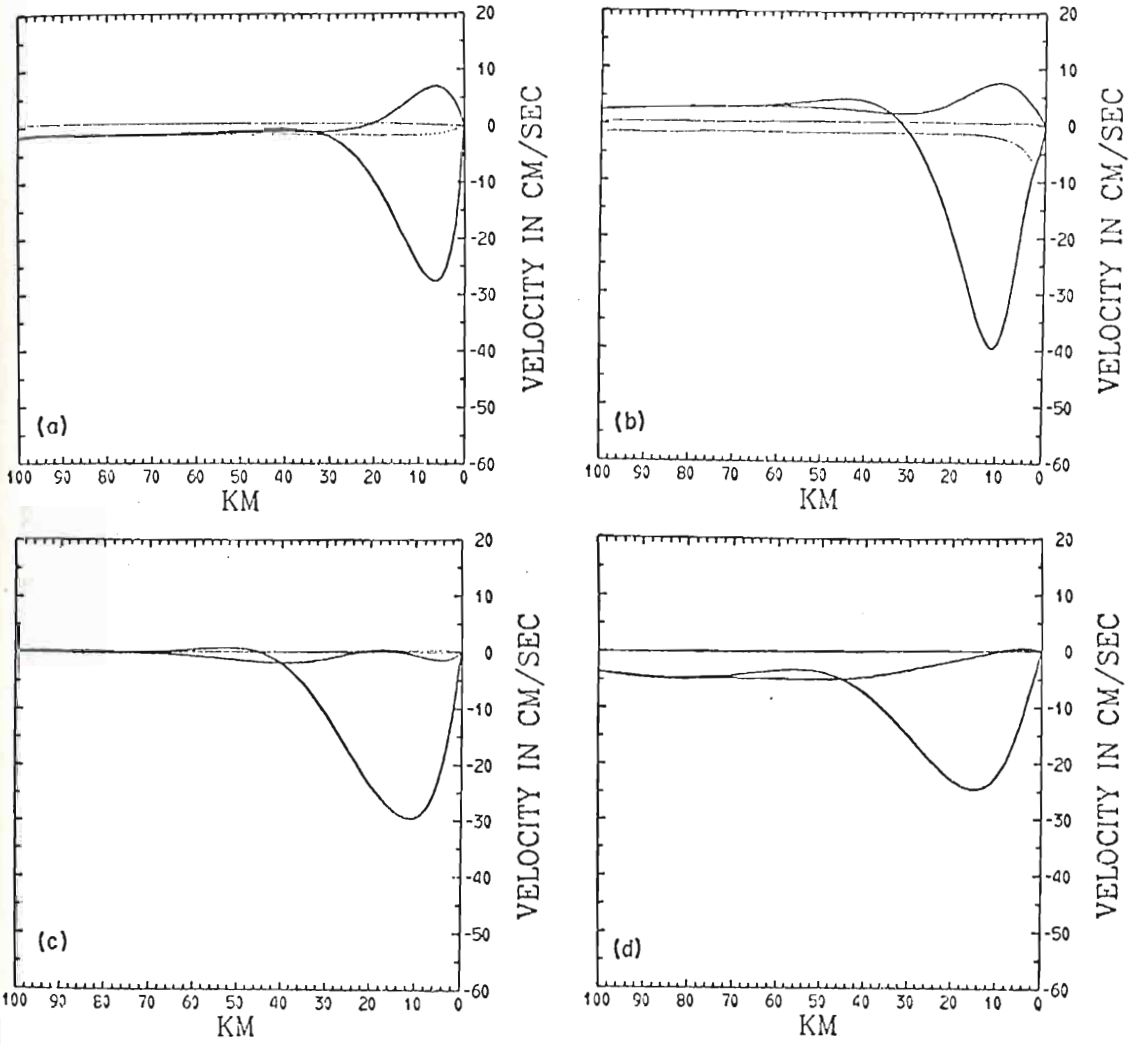

Fig. 6. Vertically averaged velocity component profiles for the flat bottom event as a function of distance offshore after 5, 10, 15, and 20 days, respectively. The zonal flow components are dashed. The upper layer longshore jet is clearly seen in each panel.

respectively. The zonal flow components are dashed. The upper layer longshore jet is clearly seen in each panel.

(1973). Simply put, the equatorward surface jet is a direct result of the conservation of potential vorticity (Charney, 1955; O'Brien and Hurlburt, 1972) applied to a wind-driven jet.

The time integral of the potential vorticity equation modified to include the β-effect for the two-layer fluid initially at rest gives

$$\frac{\partial v_1}{\partial x} - f\left(\frac{h_1 - H_1}{H_1}\right) = -\int_0^t \frac{\beta v_1}{h_1}\, dt \,, \qquad (40)$$

$$\frac{\partial v_2}{\partial x} - f\left(\frac{h_2 - H_2}{H_2}\right) = -\int_0^t \frac{\beta v_2}{h_2}\, dt \,, \qquad (41)$$

where H_1 and H_2 refer to initial layer thicknesses. The RHS of (40) and (41) are shown to be small on the upwelling event time scale. Clearly upwelling near the coast provides $(h_1/H_1) < 1$, $(h_2/H_2) > 1$, hence, for the inviscid case, v_1 must be a minimum near the coast, v_2 a maximum. While (40) and (41) do not necessarily require a jet structure for the upper layer, additional dynamical arguments assure that result.

The poleward undercurrent arises in a more complex fashion as a consequence of the north-south sea surface slope induced by the β-effect and a Sverdrup interior ocean. Physically the upper layer longshore momentum balance offshore is simply geostrophic zonal flow accompanied by an

Physically the upper layer longshore momentum balance off-

shore is simply geostrophic zonal flow accompanied by an Ekman drift component. Near the coastal boundary the zonal flow vanishes due to the kinematic boundary condition.

Consequently, the tendency term for longshore flow becomes important in the momentum balance inshore, having negative sign. Since the kinematic condition is felt on the Rossby radius of deformation length scale, the resulting equatorward acceleration has the same length scale as the upwelling scale.

Following cessations of the winds the poleward undercurrent vanishes rapidly. Upon using the first integral in x of the vorticity equation and the y-momentum equation we see that

$$\int_{-L}^{x} \beta v_1 \, dx = g \frac{\partial}{\partial y} (h_1 + h_2 + D)\Big|_x - g \frac{\partial}{\partial y} (h_1 + h_2 + D)\Big|_{-L}$$

where -L is the location of the far-wall boundary. This equation, relating the β-effect to the N-S sea surface slope, indicates that as the Sverdrup interior vanishes upon cessation of the winds, so does the Sverdrup interior velocity components, the sea surface slope, and the undercurrent.

Since the interface is still sloping toward the coast immediately after wind decay, the baroclinic component of the longshore flow may still be large, expressed approximately as

$$f(v_1 - v_2) = g' \frac{\partial h_1}{\partial x} .$$

However, near the coast intense vertical mixing substantially decreases the stratification by day 10, hence the baroclinic longshore flow component is much reduced there.

The last panel, Fig. 6d shows the spin down at day 20. The longshore jet is decaying on a viscous time scale. Allen (1973) has determined that the vertical diffusive time scale is appropriate,

$$T_V \approx \frac{H^2}{A_v} \approx 4\times10^6 \text{ sec} .$$

From our results the horizontal diffusive scale seems aplicable,

$$T_H \approx \frac{\lambda^2}{A_H} \approx 10^6 \text{ sec} .$$

Because the length scale is probably underestimated by scale λ due to spreading of the jet before decay of the wind stress, T_V and T_H are more nearly identical. Our results show the diffusive time scale to be 0(40 days).

Fig. 7a indicates the time-evolution of the pycnocline depth at 5, 10, and 15 km offshore. Note the nearly linear slope to the three curves during the first 8 days. This is a reasonable result when vertical mixing is unimportant, since from continuity and simple Ekman theory

$$W_I = -\frac{dh_1}{dt} = h_1 \frac{\partial u_1}{\partial x} \simeq \frac{-\tau_{sy}}{\rho_0 f \lambda} \approx 10^{-2} \text{ cm sec}^{-1} .$$

Subsequently, the interface at 5 km reaches a minimum depth near day 8 at which time wind mixing becomes important. Had we continued forcing past day 10 we would have found that the interface oscillates about a quasi-steady equi-

Had we continued forcing past day 10 we would have found that the interface oscillates about a quasi-steady equilibrium position near 10 m depth. At 10 km and 15 km the interface does not deepen immediately following cessation

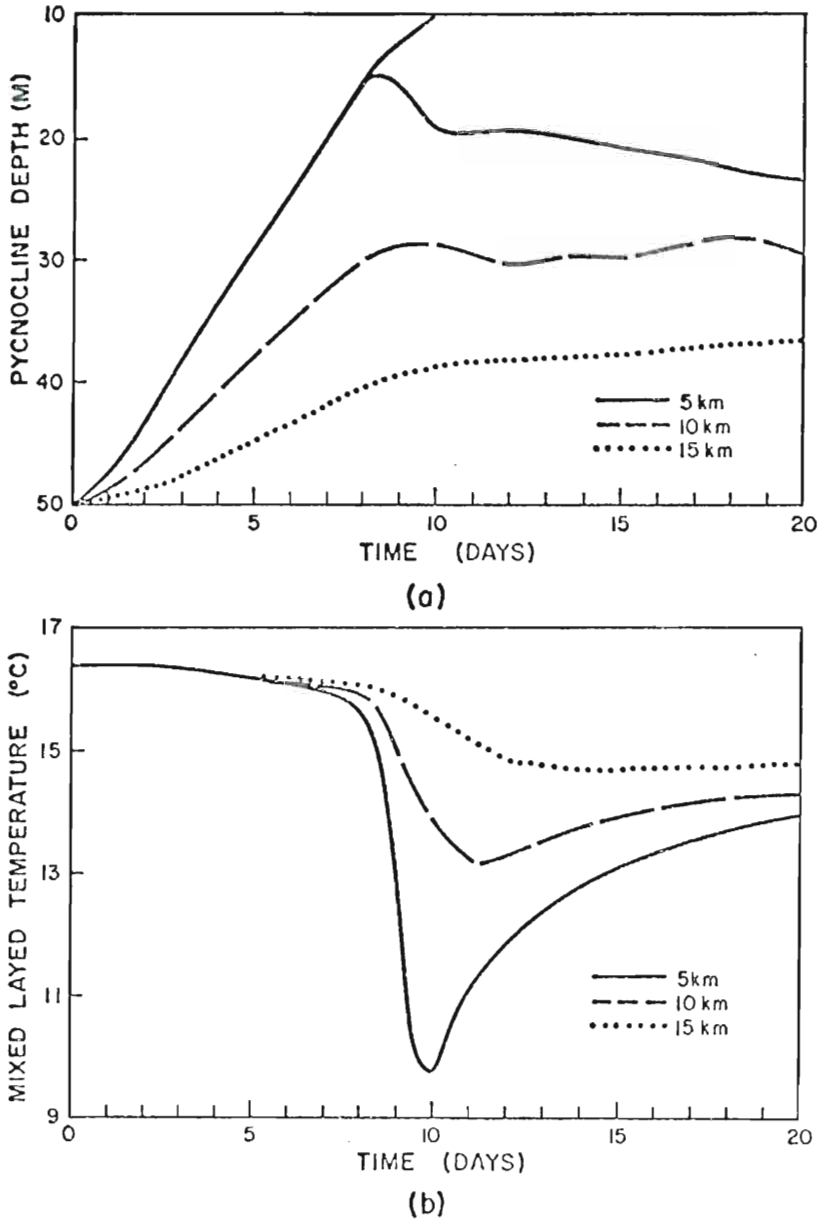

Fig. 7. Time series of pycnocline depth (a), and mixed layer temperature (b), at 5, 10, and 15 km offshore for the flat bottom event case.

and mixed layer temperature (b), at 5, 10, and 15 km offshore for the flat bottom event case.

of the wind due to the slow spin-down process. Rossby and internal wave modes are evident in the height anomaly time series of 7a.

Fig. 7b shows the SST at the same three locations. The most notable feature is the rapid cooling of the upper layer water at 5 km. Two nonlinear processes act to produce this result. First, the amount of fluid in the water column of the mixed layer decreases near shore during upwelling. As the layer thins, the pycnocline moves closer to the source of the turbulent energy at the sea surface; therefore the rate of entrainment of colder water from below is intensified. Note from equation (10) that the entrainment rate is inversely proportional to the square of the distance from the source of turbulence. At day 10 u_* begins to decrease and at that point horizontal diffusion and advection of heat become dominant. Fig. 7b and 5d indicate a small SST gradient near-shore following wind decay.

Figs. 8, 9, and 10 are composites of the total (perturbation plus vertically-averaged part) zonal, vertical, and longshore flow within 50 km of the coast at day 5, 10, and 15, respectively. These diagrams were obtained by employing the vertically-averaged flow arising from the numerical integrations in calculating perturbation quantities as discussed in Section 3.

Fig. 8a indicates the zonal flow at day 5. Outside

ties as discussed in Section 3.

Fig. 8a indicates the zonal flow at day 5. Outside the region of strong vertical shear a simple circulation described by Ekman dynamics exists, with offshore flow near

the surface and compensatory onshore flow occurring as a deep subsurface current. In this area a classical Ekman spiral solution is superimposed on the vertically-averaged current component.

Near the coast substantial vertical shear in the horizontal longshore currents occurs in the statically stable pycnocline layer. In this shear zone the longshore geostrophic balance is not maintained and shearing stress becomes sifnificant. As noted by Csanady (1972) this situation is similar to the case of rotating laminar flow between concentric disks discussed by Stewartson (1957). Here the problem is much more complicated since one actually has three "disks" at the sea surface, at the interface, and at the bottom. Further, the inner disk is tilted near the coast. Undoubtedly this analogy is easily overworked since neither the sea surface nor the interface represents a rigid surface. Also, the stress is only applied at the sea surface and is internally determined at the interface.

At the base of the pycnocline the flow is offshore while just above it the flow is onshore. The near surface offshore component is approximately 20 m deep except very near shore. This corresponds well with the Ekman depth $(A_v f^{-1})^{1/2} \simeq 10$ m. A depth of 20 m is cited by Smith (1973) as the depth over which the primary offshore transport occurs.

as the depth over which the primary offshore transport occurs.

Vertical motion at day 5 is shown in Fig. 8b. Maximum upwelling occurs at the coast and between 5-10 km

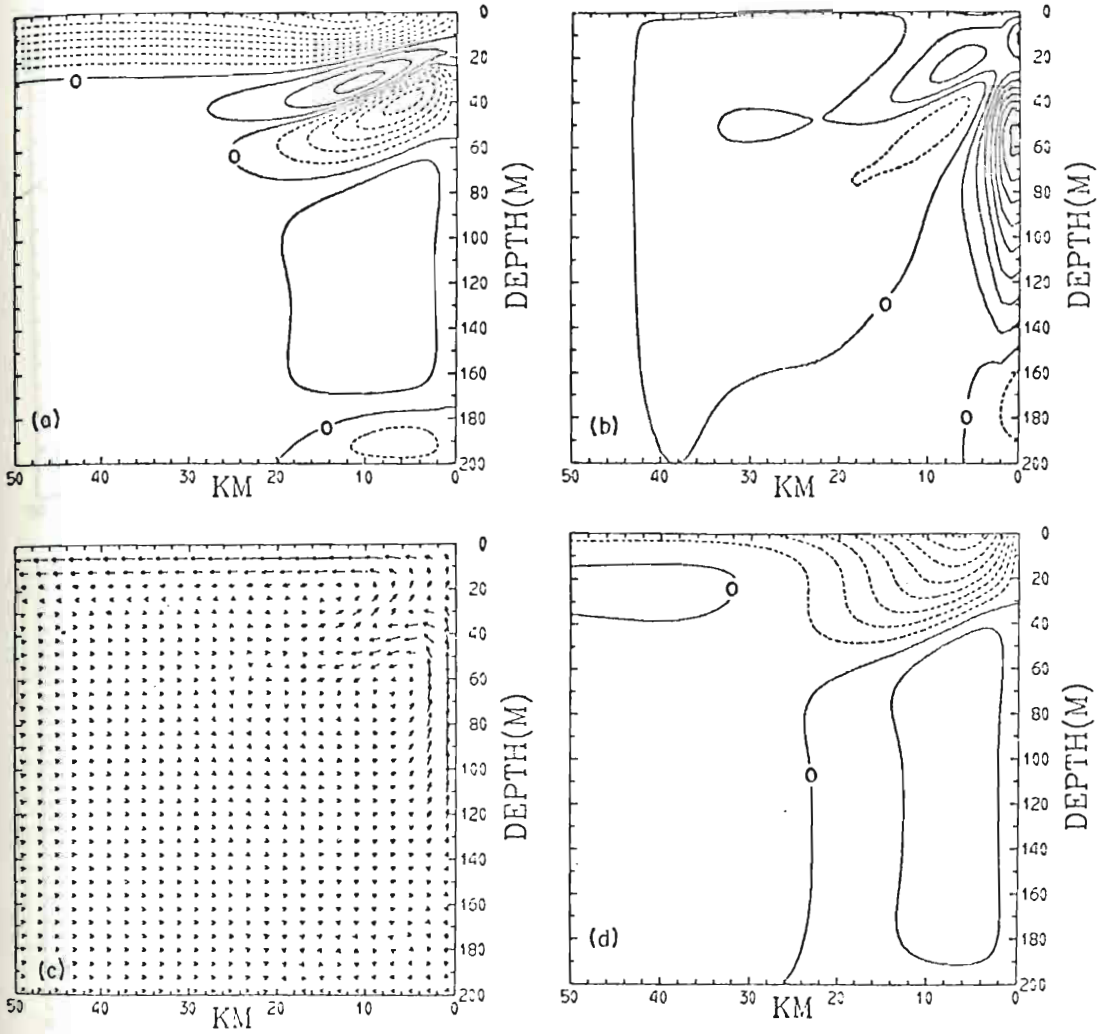

Fig. 8. Total velocity (vertically averaged plus perturbation) at day 5 for the flat shelf event case. Contours of zonal current speed are shown in (a) at 1 cm sec^{-1} intervals. The vertical motion contours in intervals of $.5x10^{-2}$ cm sec^{-1} are indicated in (b). The u-w vectors in (c) are scaled to the maximum length in the field. Longshore flow contours in (d) are presented in 5 cm sec^{-1} intervals. Dashed contours always indicate negative values.

the maximum length in the field. Longshore flow contours in (d) are presented in 5 cm sec^{-1} intervals. Dashed contours always indicate negative values.

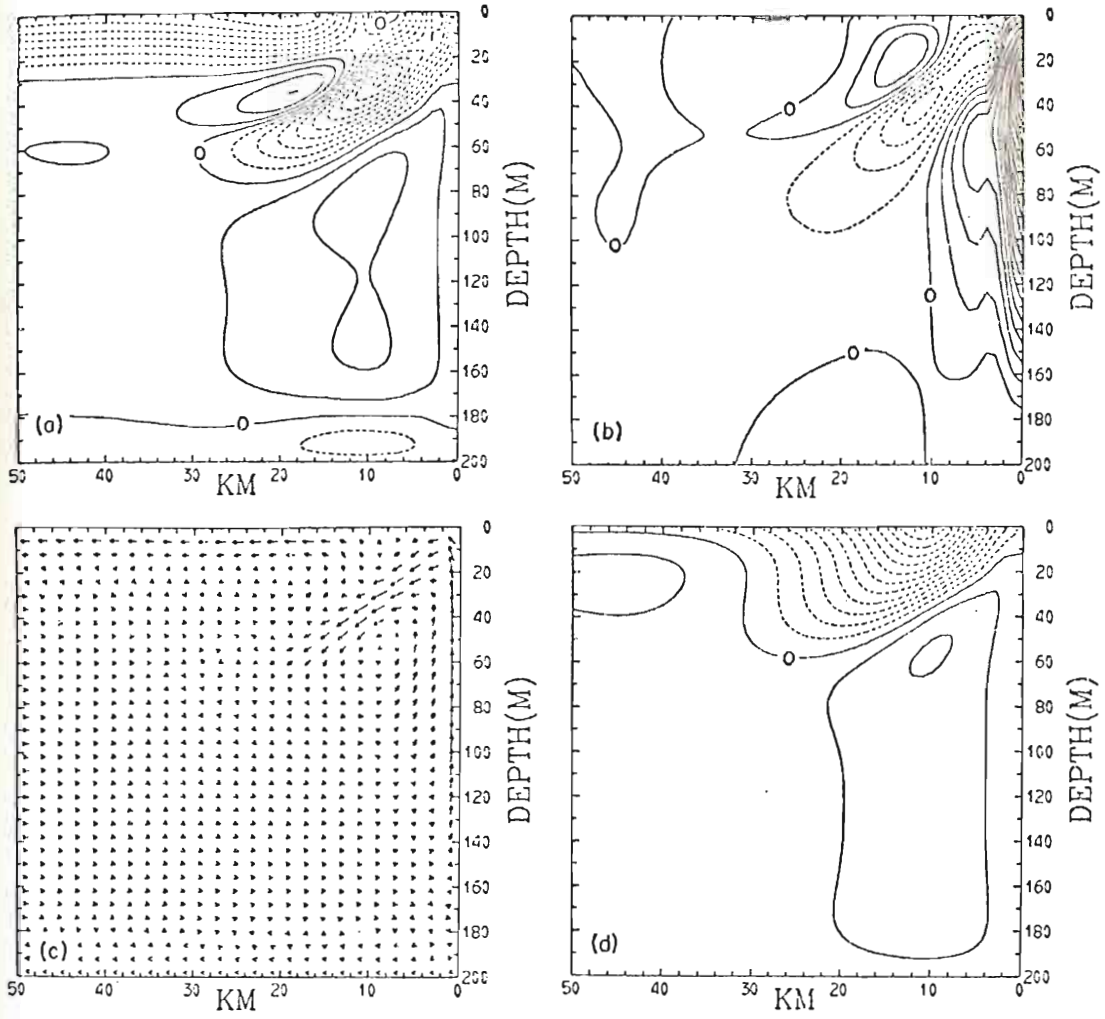

Fig. 9. Same as Fig. 8 but for day 10.

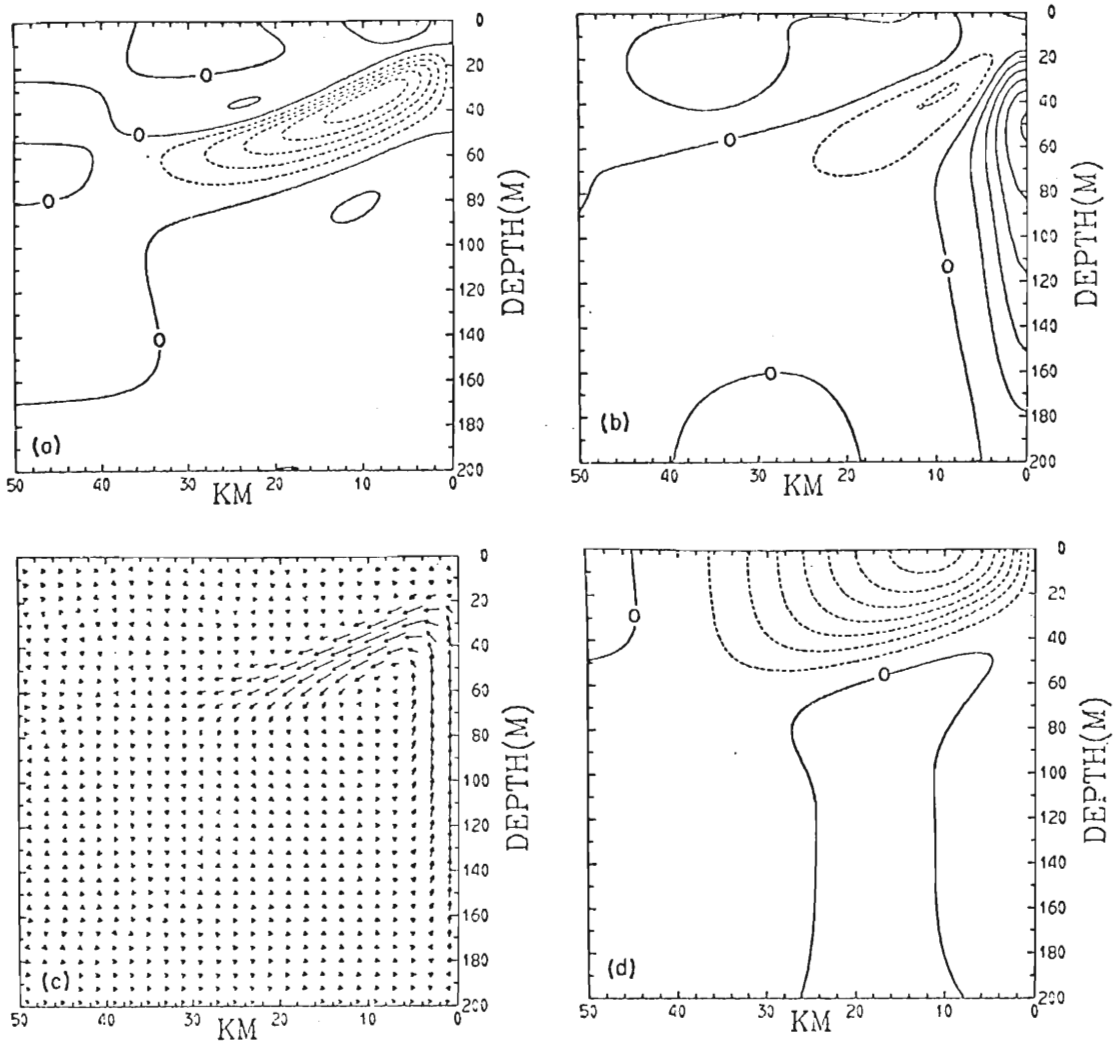

Fig. 10. Same as Fig. 8 but for day 15.

the surface and compensatory onshore flow occurring as a deep subsurface current. In this area a classical Ekman spiral solution is superimposed on the vertically-averaged current component.

Near the coast substantial vertical shear in the horizontal longshore currents occurs in the statically stable pycnocline layer. In this shear zone the longshore geostrophic balance is not maintained and shearing stress becomes sifnificant. As noted by Csanady (1972) this situation is similar to the case of rotating laminar flow between concentric disks discussed by Stewartson (1957). Here the problem is much more complicated since one actually has three "disks" at the sea surface, at the interface, and at the bottom. Further, the inner disk is tilted near the coast. Undoubtedly this analogy is easily overworked since neither the sea surface nor the interface represents a rigid surface. Also, the stress is only applied at the sea surface and is internally determined at the interface.

At the base of the pycnocline the flow is offshore while just above it the flow is onshore. The near surface offshore component is approximately 20 m deep except very near shore. This corresponds well with the Ekman depth $(A_v f^{-1})^{1/2} \simeq 10$ m. A depth of 20 m is cited by Smith (1973) as the depth over which the primary offshore transport occurs.
as the depth over which the primary offshore transport occurs.

Vertical motion at day 5 is shown in Fig. 8b. Maximum upwelling occurs at the coast and between 5-10 km

offshore at 20 m depths. Note we do not resolve the buoyancy boundary layer which brings w to zero at the wall. This omission is reasonable since that layer is passive to lowest order and supplies an insignificant net vertical mass flux.

The composite u-w vector flow is shown in Fig. 8c. Care in interpretation is desirable here since the horizontal and vertical length scales are grossly different and the vector arrows are scaled by the maximum value occurring at that time. From Fig. 8c one can clearly discern two cyclonically rotating cells within 20 km of the coast. The recirculation of fluid in the cells is highly significant to biological productivity there. Fig. 8c is similar to the schematic diagram of Mooers et al. (1973) shown in Fig. 26a, although length scales are somewhat different.

Fig. 8d depicts the isotachs of longshore flow at day 5. The equatorward surface jet and poleward undercurrent are distinct features of the diagram. Maximum equatorward and poleward flows appear 6 km offshore. Note the intense vertical shear 40 m deep within 10 km of the coast. The undercurrent jet core is broad and deep.

A significant new result is indicated in Fig. 9a showing the zonal flow at day 10. Note that at the sea surface 9 km offshore a zero zonal flow isotach is indicated. On the seaward segment of that isotach surface divergence surface 9 km offshore a zero zonal flow isotach is indicated. On the seaward segment of that isotach surface divergence exists, while on the shoreward segment convergence exists.

Physically the surface offshore Ekman drift component is opposed by the onshore gravitational circulation introduced by the intense SST gradients in the upwelling zone. At the point where these flows exactly balance the surface zonal flow vanishes. Depending on the details of the flow components a surface convergence or divergence zones may arise. It is proposed that a delicate balance between the offshore Ekman drift and the onshore gravitational circulation can produce the observed surface convergence zones. In the ocean buoyant debris lodges along the convergence lines, making them highly visible from ship or aircraft. The divergence zones are not so easily revealed although long surface streaks may indicate their presence. One reasonably expects that such convergence or divergence zones, if indeed they are produced by a delicate balance between wind forcing and SST gradients, would not persist for long periods and at times might be completely obscured by wave action.

The vertical motions shown in Fig. 9b indicate strong upwelling at the coast and 10-20 km offshore. Note the two distinct width scales of vertical motion within 10 km of the coast. The wider upwelling scale is the ordinary Rossby radius of deformation scale. The much narrower upwelling width scale represents a viscous scale arising from the very low stratification existing near the coastal boundary. This remarkable figure depicts a matching of upwelling circula-

low stratification existing near the coastal boundary. This remarkable figure depicts a matching of upwelling circula-

tions in stratified and homogeneous regimes and dramatically

depicts the two dominant horizontal length scales, the viscous scale and the deformation scale.

Fig. 9c graphically portrays the surface convergence and divergence zones, the two near-surface upwelling regions, and the two-celled circulation. Note the weak offshore flow at the sea bottom. Fig. 9d demonstrates the strong tilt with depth in the equatorward jet. A similar result was found by McNider and O'Brien (1973) in a four-layer hydrodynamic model. Notice that the jet maximum is observed further offshore compared to day 5.

To conclude this series corresponding profiles at day 15 are presented in Fig. 10. The circulation in the strong shear layer is striking in Fig. 10a, b, and c. Remarkably the upwelling motions are still significant four days after complete cessation of the winds, although subsurface water does not penetrate to the sea surface. A surface convergence zone can be found 36 km offshore and a surface divergence is evident 20 km offshore. The equatorward jet is in decay, as is the poleward undercurrent. The undercurrent jet axis is displaced seaward of the equatorward jet axis.

To provide additional perspective on the vertical structure of the flow the u and v speeds are plotted versus depth for days 5 and 10 at 10 km offshore. Fig. 11a depicts the vigorous two-cell circulation in the meridional flow at

depth for days 5 and 10 at 10 km offshore. Fig. 11a depicts the vigorous two-cell circulation in the meridional flow at day 5 and the effect of strong SST gradients on attenuating

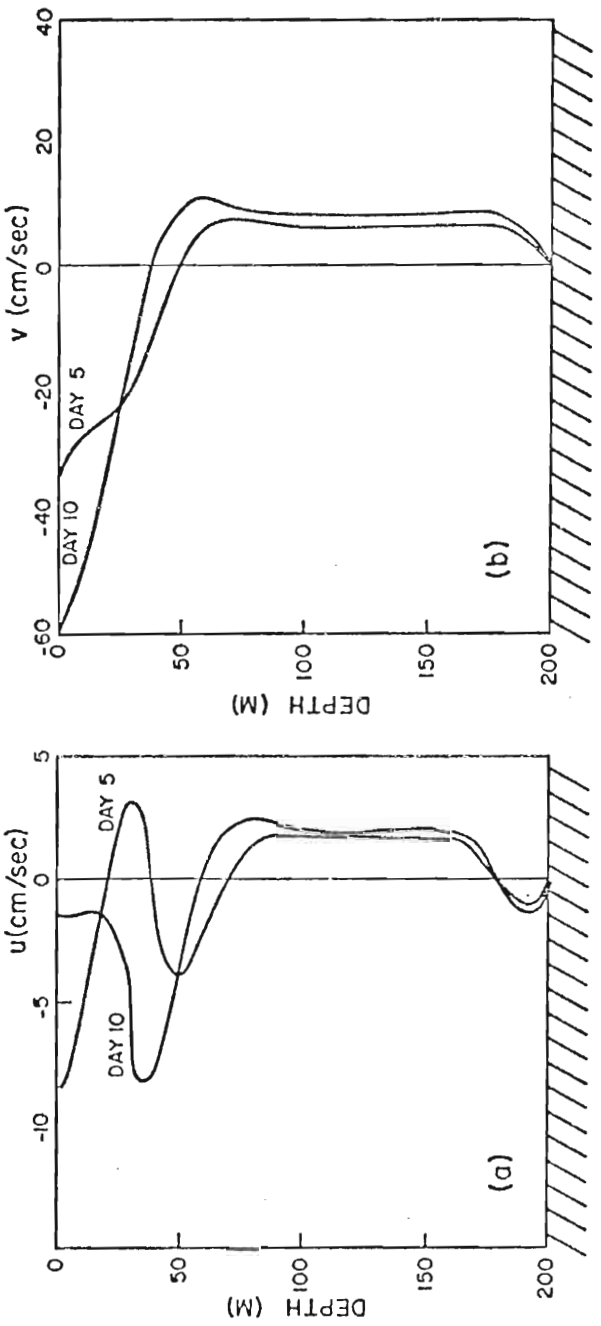

Fig. 11. Depth profiles of the zonal (a), and longshore (b) flow in the flat bottom event case at day 5 and 10, 10 km offshore.

the surface offshore flow at day 10. Near 35 m the onshore flow at day 5 has reversed to offshore flow by day 10. Weak offshore flow in the bottom Ekman layer is maintained over the period.

The longshore flow profile is rather simple with poleward flow below 50 m, equatorward flow above. The meridional gravitational circulation at day 10 provides a component which enhances the equatorward surface jet due to the earth's rotation. Also, as can be seen by the increased poleward flow near 50 m, it provides a poleward component near the base of the upper layer.

Fig. 12 indicates x-t sections of the longshore currents at 5 m and 150 m. Fig. 12a clearly delineates the time evolution of the equatorward jet. As the vertical mixing becomes intense around day 8 vertical transport of horizontal momentum attenuates the jet inshore, causing the jet maximum to be displaced further offshore. When the winds begin to subside at day 10 vertical turbulence diminishes , stratification is reestablished near the coast, and the jet core ceases further offshore movement. Of note is the Rossby wave velocity component appearing 30-50 km offshore. Fig. 12b clearly depicts the poleward undercurrent and the development of the Rossby wave mode.

The final figure in Subsection 5.1 summarizes an unusual experiment in which the flat bottom model was driven

The final figure in Subsection 5.1 summarizes an unusual experiment in which the flat bottom model was driven continuously for 60 days by a -1 dyne cm^{-2} longshore wind

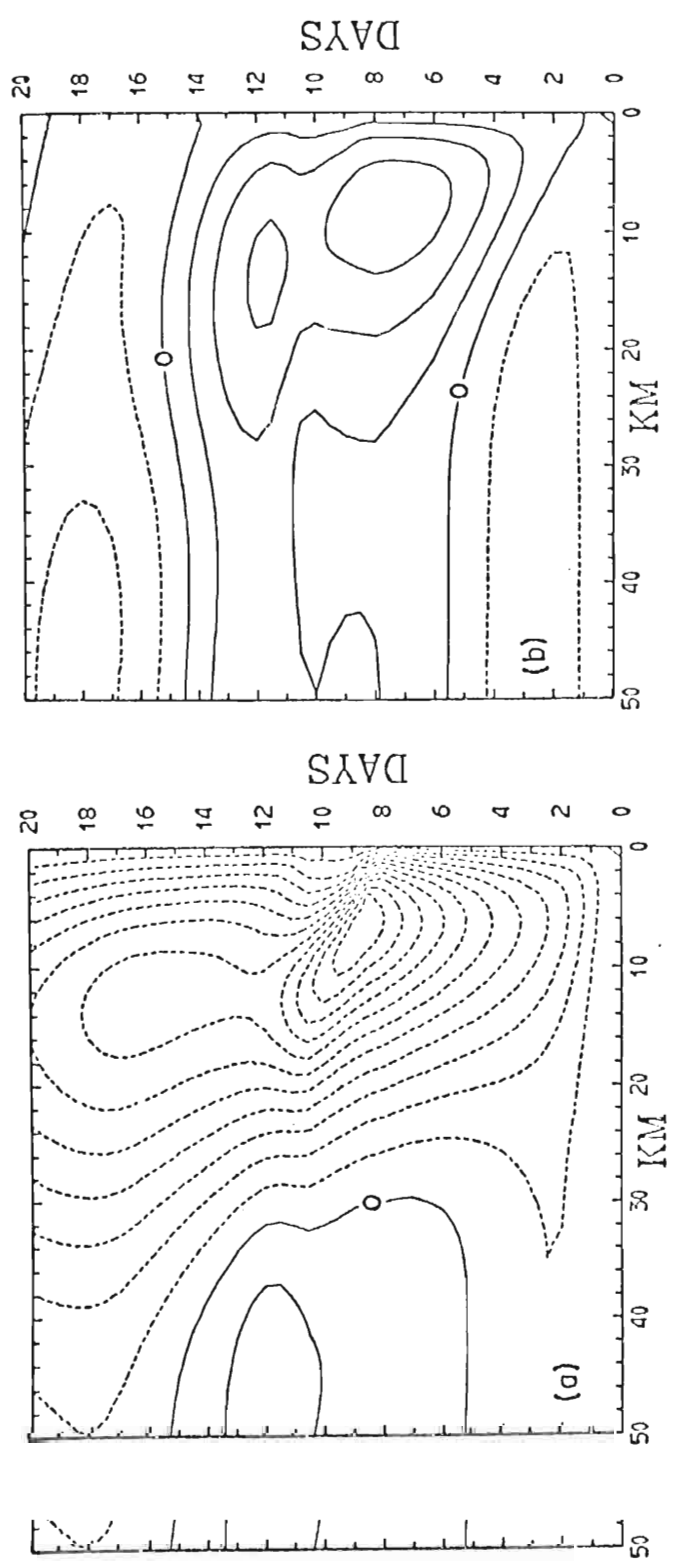

Fig. 12. The x-t sections for longshore flow in the flat bottom event case at 5 m (a) and 150 m (b). Contour intervals are 5 cm sec^{-1} in (a) and 3 cm sec^{-1} in (b).

stress. Remarkably the stratification inshore did not completely disappear with time. A quasi-steady state is in evidence during the latter half of the experiment.

Fig. 13a shows the x-t section of longshore flow at 5 m depth. Significantly, the longshore jet axis is located further offshore as time proceeds. Dynamically this result is a consequence of the combined effects of increased mixing arising from decreased stratification inshore and the offshore movement of the maximum SST gradient in time. Offshore the vertically-averaged upper layer longshore flow balance is

$$- fv_1 = - g \frac{\partial}{\partial x} (h_1 + h_2 + D) - \frac{g h_1}{2\rho_0} \frac{\partial \rho_1}{\partial x} .$$

Near the coast the horizontal density gradient provides a poleward component to the longshore flow which may be substantial.

The equatorward jet, whose width scale was originally governed by the baroclinic Rossby radius of deformation may be found far offshore as inshore mixing proceeds under strong northerly winds and the maximum SST gradient moves seaward. Observe the broad horizontally homogeneous water temperatures within 10 km of the coast following intense mixing.

Fig. 13c graphically illustrates one significant deficiency of this model, namely, that the wind-mixed layer can only deepen (ignoring vertical advection). There is no limiting depth at which no additional deepening occurs

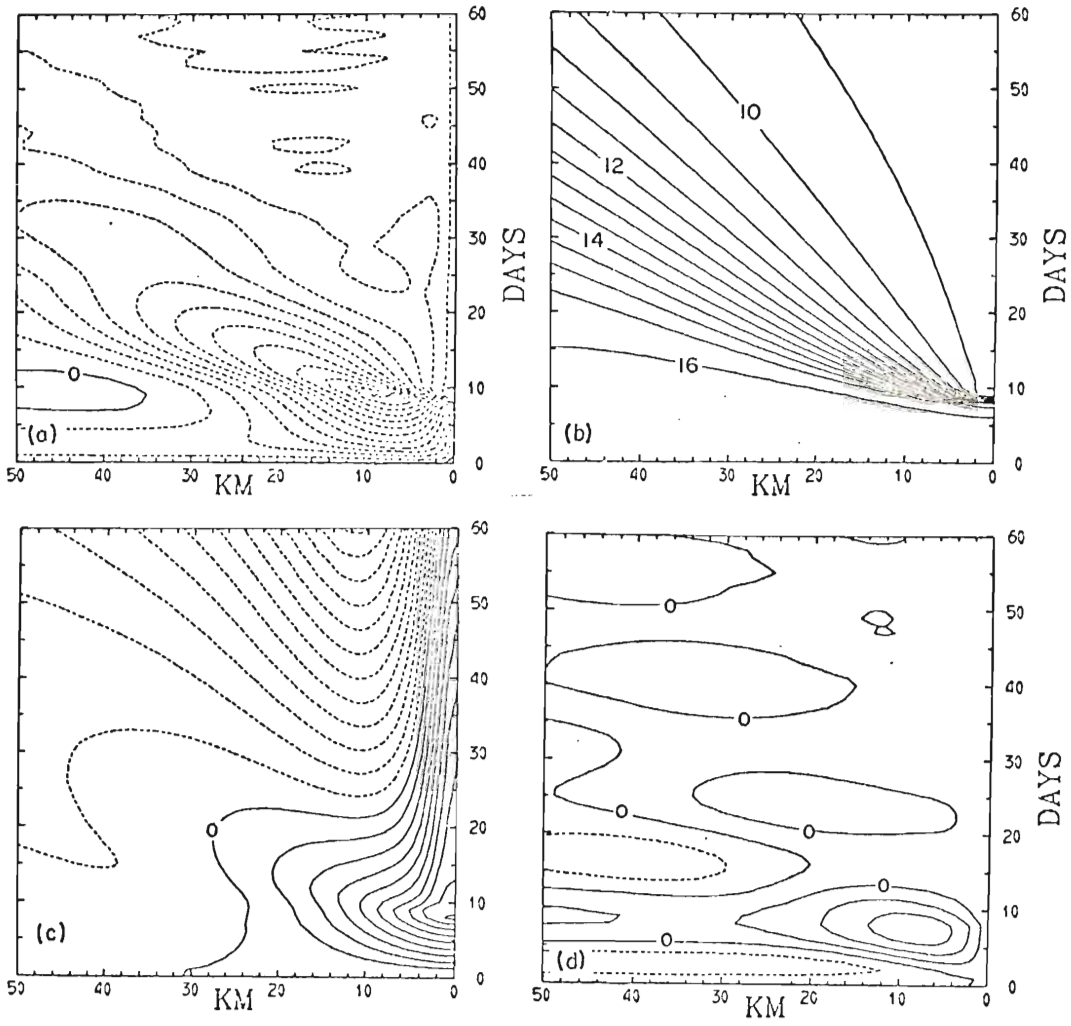

Fig. 13. The x-t section of longshore flow at 5 m for the flat bottom, continuously forced case is shown in (a). In (b) the upper layer temperature x-t section is presented. The interfacial height anomaly x-t section (10 m contours) for the same case is shown in (c). In (d) longshore speed contours at 150 m (3 cm sec^{-1} intervals) are presented.

m (3 cm sec^{-1} intervals) are presented.

(such as a u_*/f depth limit). Note that while the inshore stratification weakens the upwelling width scale transforms from the deformation scale to the viscous scale. The zone in which vertical advection dominates wind-deepening narrows with time. In addition, by day 60 the deepening process produces a 60 m negative height anomaly 10 km offshore. Clearly such a result is highly unrealistic. It must be remembered however that it is also unrealistic to expect continuous, strong northerly winds over an upwelling region for two months. Further, we have omitted radiative effects in this experiment, which would have maintained inshore stratification and substantially reduced the deepening process.

In conclusion, Fig. 13d is included in order to vividly portray the transient barotropic Rossby wave which propagates offshore with time. Analysis of this forced Rossby wave is complicated by the coastal boundary, the unusual spatial distribution of the wind forcing, and the quasi-impulsive starting of the wind stress curl. Longuet-Higgins (1965), Gates (1968) and Geisler and Dickinson (1972) have examined some aspects of the ocean Rossby wave problem both analytically and numerically but unfortunately their studies are not directly applicable to our work.

Assuming the gross applicability of the linear, plane wave physics governing a solitary Rossby wave unaffected by solid boundaries, advection, and viscosity, the phase speed is

$$C_R = \frac{-\beta}{\frac{m^2\pi^2}{L^2} + \frac{f^2}{g(H_1 + H_2)}}$$

where m = 1, 2 . . . and L is the channel width. Although many wavelength waves are excited by the near impulsive starting, the dominant wave scale appears to be ≃ 100 km. The calculated phase speed for that wave is 2 cm sec^{-1}. The phase speed determined directly from the x-t diagram is approximately 1.2 cm sec^{-1}. The detailed analysis of these Rossby wave modes awaits future work, though the apparent modulation of the wave as it moves offshore remains unexplained. Note that the nearshore undercurrent prior to day 10 appears as the first maximum in the Rossby wave field. From this result it appears likely that the observed poleward undercurrent is related to the development and offshore propagation of Rossby waves.

5.2 The continental shelf model

Realism in modelling actual coastal upwelling regimes requires the addition of a continental shelf. In this section a model case is described which has an exceedingly simple shelf topography, as indicated in Fig. 16. For this model the upper layer is initially 50 m deep and the shelf is 75 m below the sea surface inshore of 30 km. The bottom depth increases linearly to 200 m at 40 km, providing a realistic shelf slope of 1.25×10^{-2} between 30 and 40 km off the coast. Seaward of 40 km the ocean bottom is flat. All

other parameters are identical to the flat bottom case discussed in Section 5.1.

Two versions of this model were studied, one with the event forcing described earlier and the other with continuous forcing for a twenty-day period. In Fig. 14 interfacial height anomaly x-t sections are shown for the continuous (a) and event (b) forcing. Notably the event forcing provides an upwelling width scale much larger than that provided by the continuous forcing after day 10. Once more, intense vertical mixing inshore reduces the stratification, enhances mixed-layer deepening, and forces the upwelling to occur on a viscous width scale instead of a deformation scale. Fig. 14c depicts the SST x-t section for the continuous forcing case. The "event" analog was omitted since for that case insignificant mixing occurred before and after the winds were turned off and upper layer temperatures changed only slightly 0(.1°C) during the integrations.

The presence of the continental shelf reduces the rate of upwelling near the coast, as noted by Hurlburt and Thompson (1973). A secondary upwelling region over the shelf slope is produced which effectively widens the zone of positive height anomaly in Fig. 12a, b as compared to Fig. 5 of the flat bottom case. Secondary upwelling is consistent with potential vorticity conservation in the slope region.

The region of maximum zonal SST gradient moves off-tial vorticity conservation in the slope region.

The region of maximum zonal SST gradient moves offshore following the initial formation of the front during continuous forcing. It is not clear whether the front would

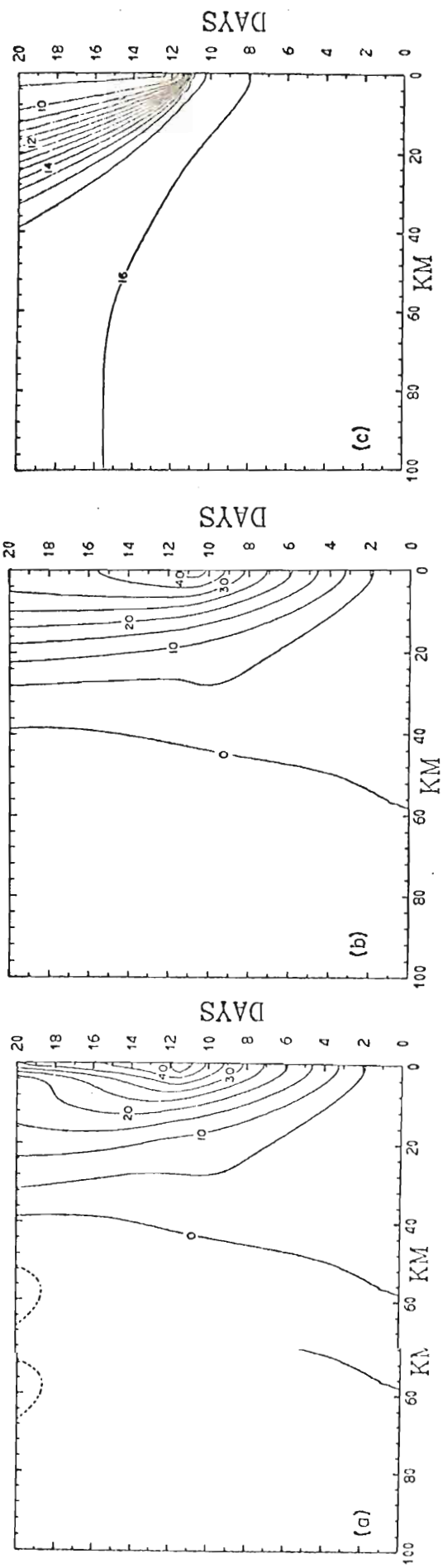

Fig. 14. The continental shelf case interfacial height anomaly x-t sections for the continuous (a) and event (b) forcing. The continuous forcing case x-t section for upper layer temperature is shown in (c).

continue offshore movement if the integrations were continued. Unfortunately, shortly after day 20 the water near shore became virtually homogeneous and the integrations were terminated. In this case significant entrainment of surface water downward into the lower layer was accomplished by bottom generated turbulent motions over the shallow shelf. There the lower layer temperature increased several tenths of degrees during the 20-day period and horizontal diffusion and advection could not balance the additional vertical mixing.

Fig. 15a presents time series of pycnocline depths at three locations offshore, while Fig. 15b depicts mixed-layer temperature time-series at these same three locations. In Fig. 15a both the event forcing and the continuous forcing results have been included. At 5 and 10 km offshore the pycnocline deepens rapidly under continuous forcing after day 11. Clearly vertical advection is dominated by the downward flux of turbulent energy which deepens the layer. In this case no quasi-equilibrium depth is encountered nearshore, although at 5 km the mixed-layer temperature does reach a quasi-steady value after day 15.

Fig. 16a depicts the zonal flow near the continental shelf at day 5. As expected, the near-surface transport is offshore following the usual Ekman theory. The presence of the sharp shelf break and slope introduces a secondary divergence and upwelling zone roughly 30 km offshore. Because
the sharp shelf break and slope introduces a secondary divergence and upwelling zone roughly 30 km offshore. Because
the offshore transport is roughly the same at points over the shelf and seaward of it, mass continuity requires that

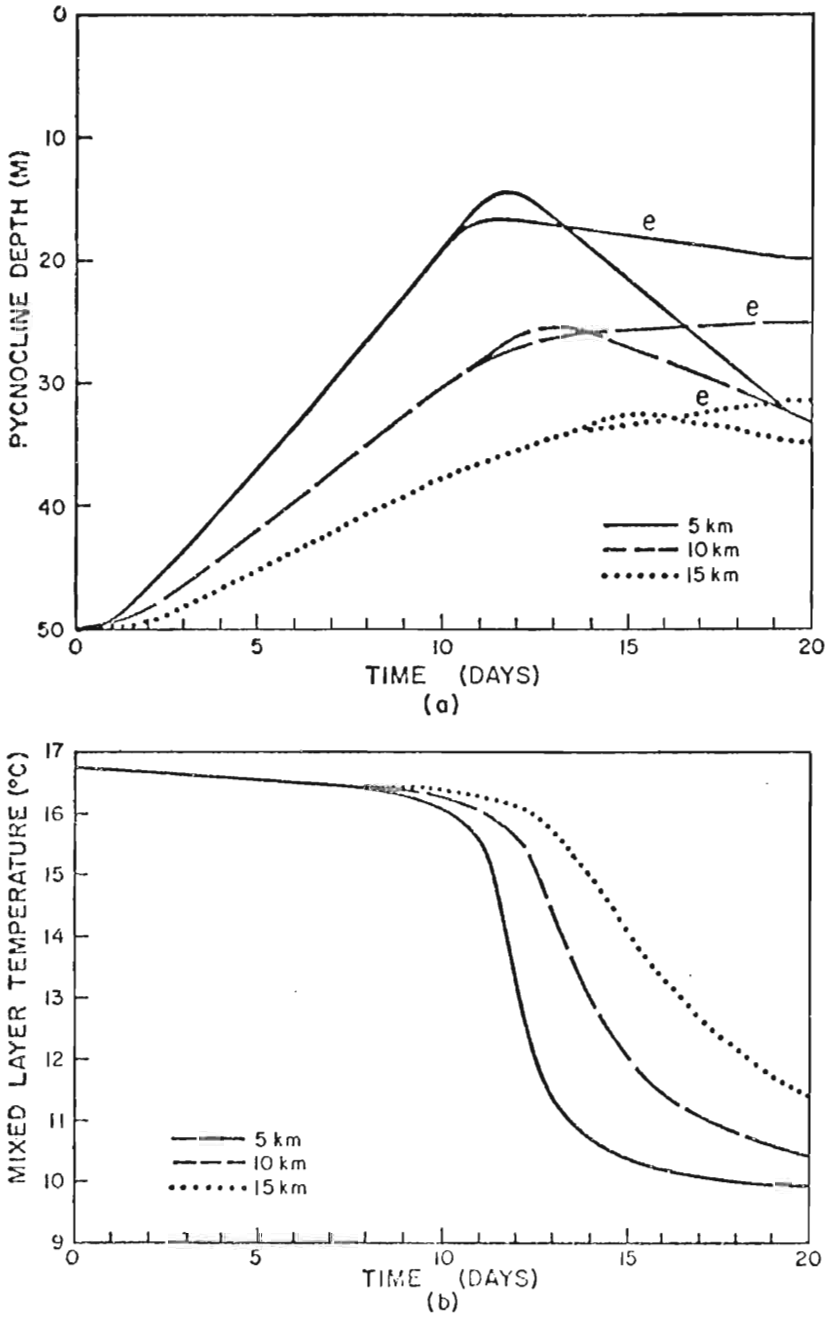

Fig. 15. Time series of pycnocline depth for the event (e) and continuously forced case at 5, 10, and 15 km offshore are shown in (a). In (b) mixed layer temperature time series for the continuously forced case are presented.

and 15 km offshore are shown in (a). In (b) mixed layer temperature time series for the continuously forced case are presented.

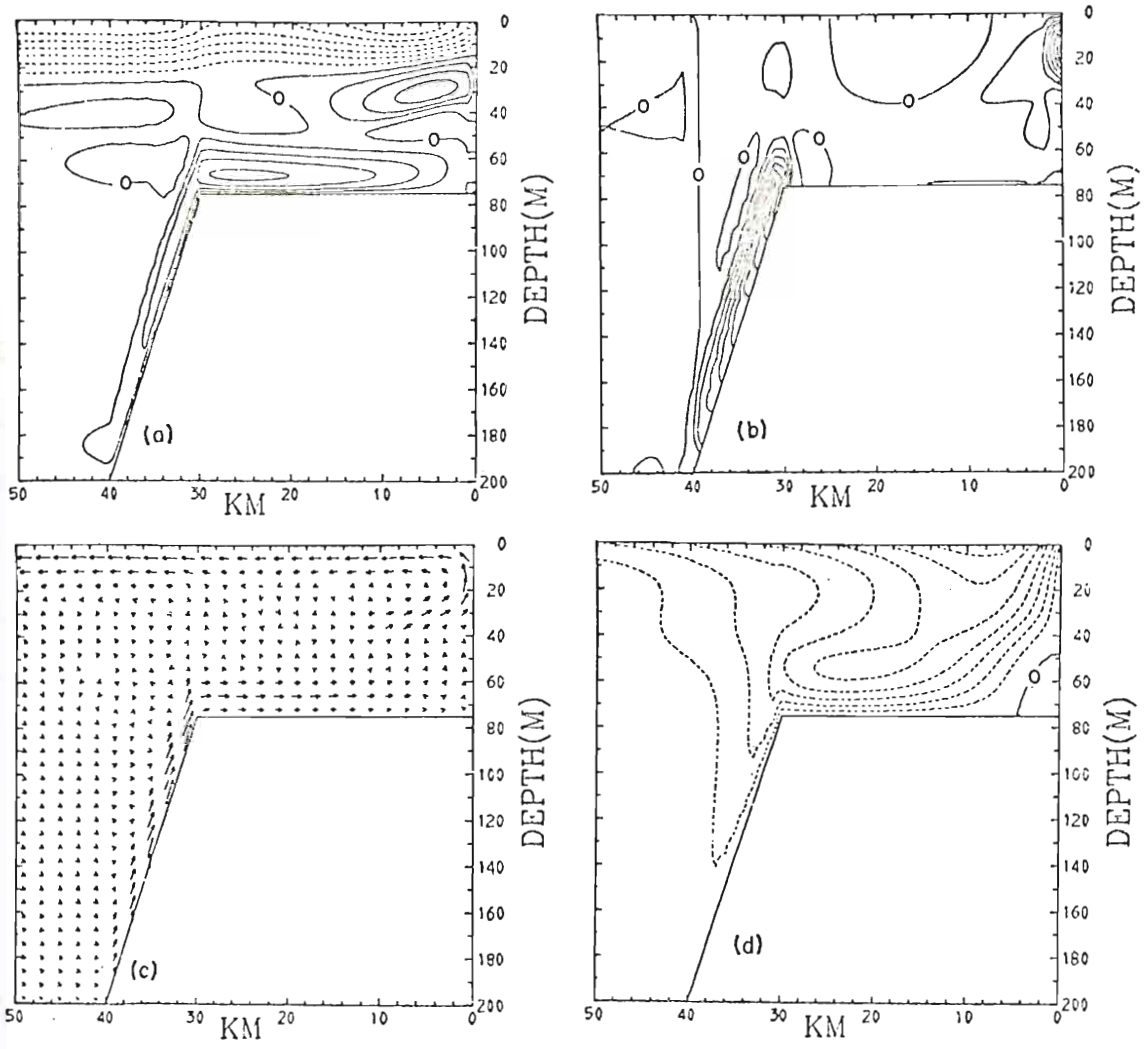

Fig. 16. Same as Fig. 8 but for the continental shelf event case at day 5.

the return flow be greater over the shallow shelf than outside it. Such a result is clearly indicated in Fig. 16a. Also, over the continental slope and shelf bottom friction becomes important, resulting in a strong bottom flow up the continental slope and across the shelf. Fig. 16b graphically outlines the primary and secondary coastal upwelling zones.

The vector plots of Fig. 16c are quite useful in determining the flow normal to the coast. Of interest is the splitting of the flow at the shelf break into two segments, one feeding the primary upwelling, the other feeding the secondary upwelling. Note the deep shoreward current appearing off the shelf slope. The two-cell circulation has not developed near the coast at day 5, rather a single cyclonic near-surface gyre provides the main transhore circulation. The bottom boundary flow does supply mass to the upwelling at the coast.

While the onshore, vertically-averaged flow is geostrophically balanced off the continental shelf, geostrophy over the shelf cannot be maintained due to bottom friction. In the initial spin-up supergeostrophic onshore flow over the shelf and slope provides an equatorward acceleration, and enhances the equatorward flow. Note in Fig. 16d the surface equatorward jet has a subsurface
acceleration, and enhances the equatorward flow. Note in Fig. 16d the surface equatorward jet has a subsurface

counterpart tilting offshore with depth. In fact, there appears an equatorward jet maximum over the continental slope. The development of the poleward undercurrent is inhibited by the equatorward acceleration introduced by the topographic influence. Nevertheless, within 6 km of the coast the N-S pressure gradient does produce a weak poleward flow, nestled against the coast.

Fig. 17a is a snapshot of the zonal flow at day 10. The singularly most dramatic difference between this picture and the same diagram at day 5 is the two-cell circulation that has developed near the coast. The shear in the longshore currents (Fig. 17d) near the coast has increased substantially from day 5. During the early spin up the baroclinic flow component increases as the pycnocline tilts upward toward the coast. The shearing stresses, arising from the vertical current shears and of greatest magnitude near the pycnocline, also increase as the pycnocline tilts upward. The net result is that an ageostrophic current develops in the vicinity of the pycnocline, directed offshore at its base, onshore above. Dynamically this current is analogous to cross-isobaric flow observed in the atmosphere near the ground. Very near the coast the stratification decreases rapidly as the interface rises near the sea

sphere near the ground. Very near the coast the stratification decreases rapidly as the interface rises near the sea

surface and wind-mixing becomes important. As the

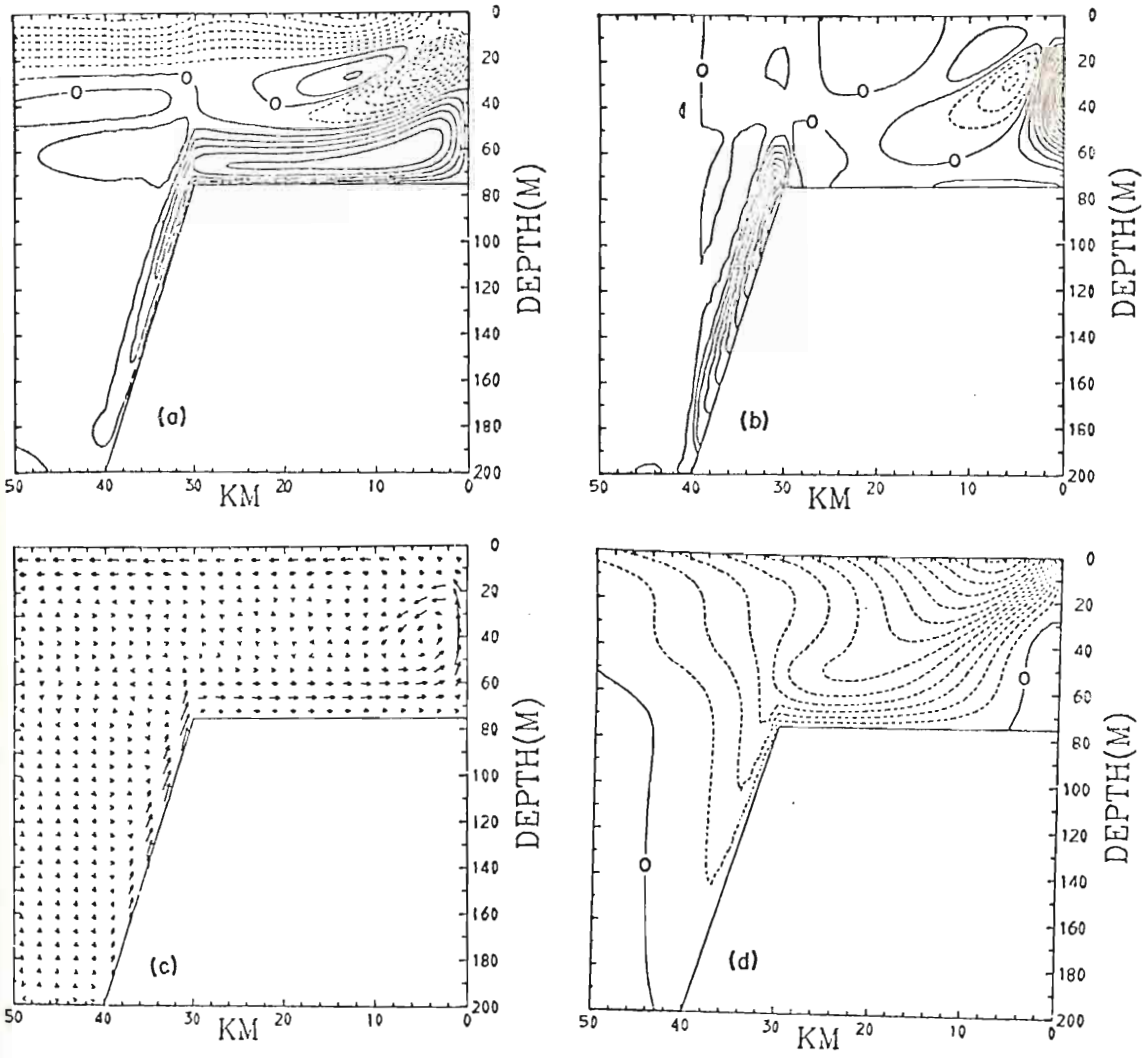

Fig. 17. Same as Fig. 8 but for the continental shelf event at day 10.

stratification decreases, upwelling occurs on a frictional length scale $O[(A_H f^{-1})^{1/2}]$ as well as the baroclinic radius of deformation scale. In regions where the water is virtually homogeneous no large baroclinic currents are possible and the two-cell circulation is not maintained.

Fig. 17c illustrates the two-cell circulation well. Note the cyclonic circulation on the continental shelf slope and just offshore. Mass is being fed into the flow along the slope from all depths, with some recirculation of mass indicated. The longshore flow of Fig. 17d contains the familiar equatorward jet tilting offshore and the near-coast weak undercurrent. The poleward flow seaward of the continental slope is significant but very weak and is a manifestation of a barotropic Rossby wave.

Upon cessation of the winds at day 11 the model begins to spin down slowly. The strong shear zone produced by the longshore flow is sufficient to drive an offshore current at the base of the pycnocline for a considerable period. Compensating flow near the bottom is required to complete the circulation, as shown in Fig. 18c for the event case at day 15. Further, the strong horizontal temperature gradient in the upper layer provides an additional driving, producing a thermal-wind component onshore very near the coast and a surface divergence zone about 10 km offshore.
producing a thermal-wind component onshore very near the coast and a surface divergence zone about 10 km offshore.

The comparison between the event and continuously forced continental shelf model cases is best accomplished

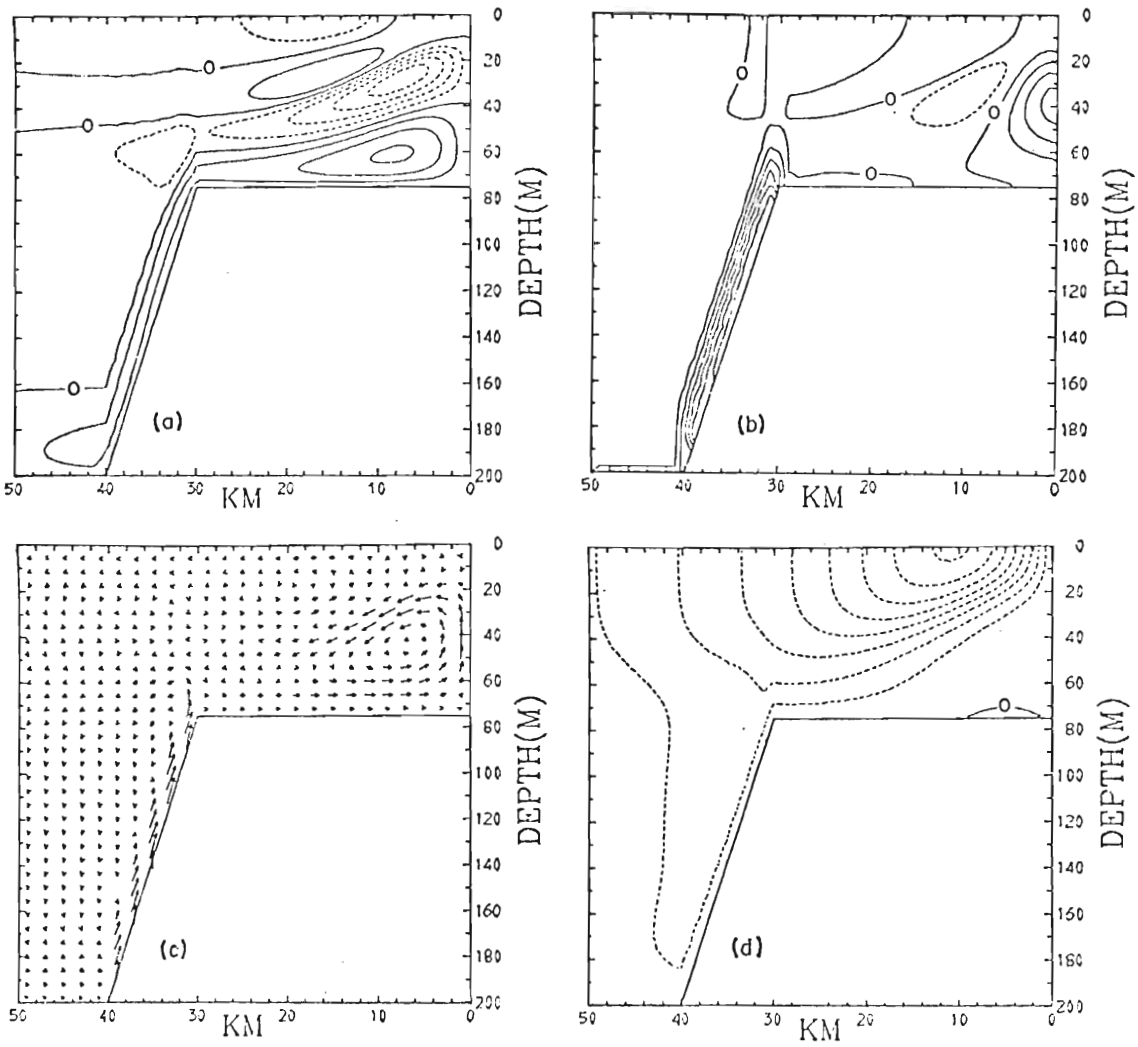

Fig. 18. Same as Fig. 8 but for the continental shelf event case at day 15.

using x-t sections. Fig. 19 compares longshore flow at 5 m and 50 m. Fig. 19a depicts the longshore flow in the event case at 5 m, while Fig. 19b shows the same parameter for the continuously forced case. Note that in the event case the longshore equatorward jet maximum moves only slightly offshore after cessation of the wind stress. The jet axis is found near 8 km offshore at day 10 and about 14 km offshore at day 20. Maximum amplitude of the jet ranges from above 60 cm sec^{-1} at day 10 to about 30 cm sec^{-1} at day 20.

The continuously forced model solutions at 5 m indicate that the jet maximum moves from the 8 km position at day 10 to approximately 24 km offshore by day 20. Near-shore the longshore flow is attenuated by vertical-mixing of momentum and by the effect of wind-induced deepening.

Regarding the longshore flow component at 50 m, there also occurs an equatorward jet in both cases. In the event case the jet maximum appears as a broad 10 km wide current which rapidly vanishes as the winds decay. As remarked above, this subsurface extension of the surface jet is a result of supergeostrophic onshore flow which acquired equatorward acceleration on rising up the continental slope. Noteworthy in Fig. 15c are the poleward-directed currents near the coast and seaward of the continental slope. The nearshore equatorward flow is small (< 3 cm sec^{-1}) and narrow (3 km). As the winds diminish the band widens, then decays suddenly at day 14, only to be reinitiated at day 18.

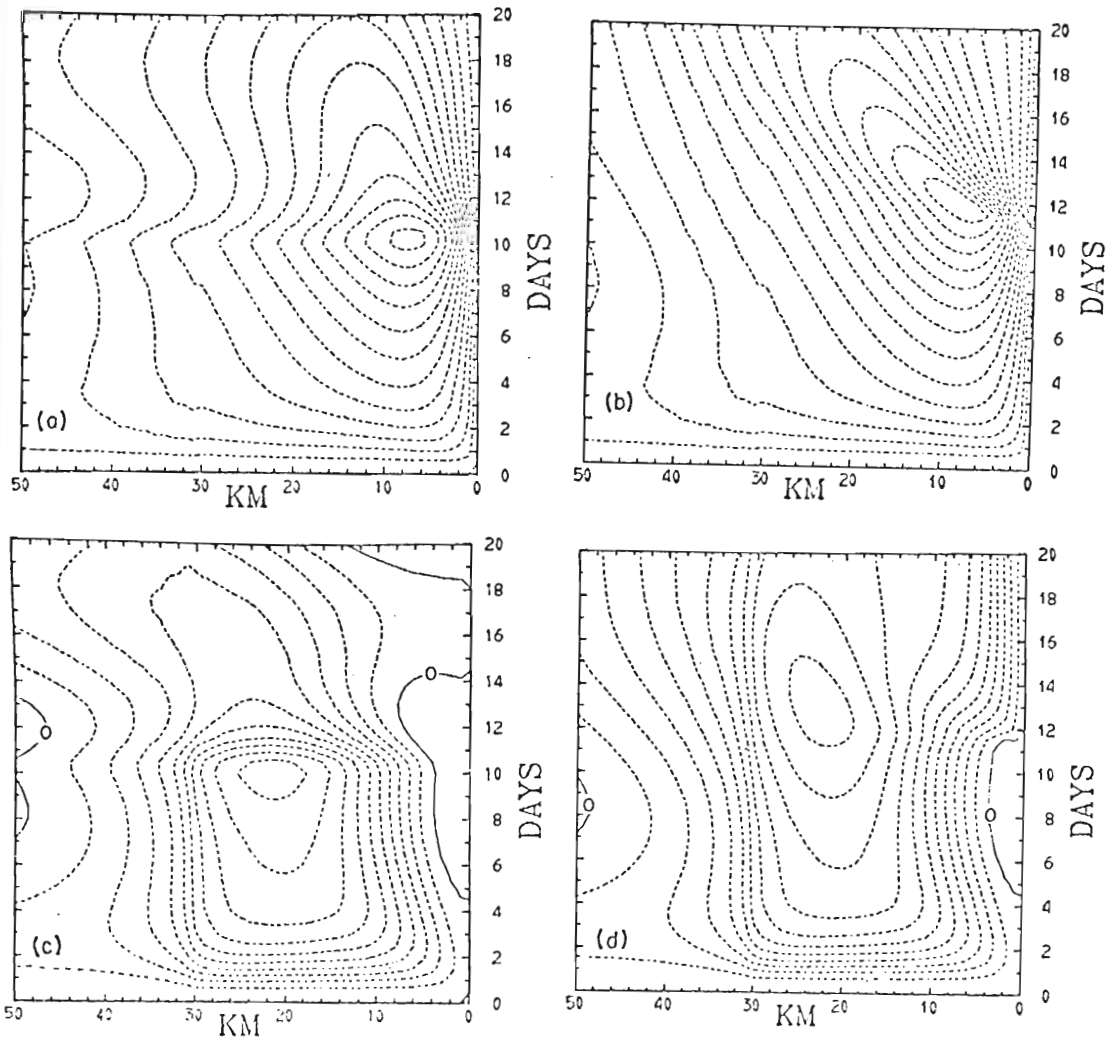

Fig. 19. The x-t sections of longshore flow at 5 m depth for the event (a), and continuously forced (b) continental shelf case. Similar sections at 50 m are presented in (c), (the event), and (d). Contour intervals are 5 cm sec^{-1} at 5 m, 3 cm sec^{-1} at 50 m.

at 50 m are presented in (c), (the event), and (d). Contour intervals are 5 cm sec^{-1} at 5 m, 3 cm sec^{-1} at 50 m.

The offshore poleward flow is also weak and quite tenuous. These poleward currents are manifestations of Rossby waves in the solutions.

To complete the comparison of event and continuously-forced cases Fig. 20 is included. This figure compares the zonal flow at 5 m and 50 m. The general offshore Ekman-drift is clearly in evidence during the first ten-day period. Not unexpectedly in Fig. 20a the offshore flow component rapidly decays as the wind driving vanishes, from day 10 to day 11. A divergence zone is denoted by the zero isotach approximately 8 km offshore from day 11 to day 20. Along this line residual upwelling continues even after the winds cease blowing. In Fig. 20b the maximum offshore flow speed occurs when the upper layer thickness within 2 km of the coast has decreased to its minimum value between day 11 and day 12.

In Fig. 20c even when the winds are turned off positive zonal flow continues, albeit diminishing in strength, within 10 km of the coast. In the continuously forced case offshore flow at 50 m depth is only found over the continental shelf slope. Note how sharply the isotachs define the shelf break and the accompanying divergence line.

To conclude the continental shelf case we have plotted the event case u and v velocity profiles versus depth at 9 km offshore for day 10 and day 15 in Fig. 21. We wish to include this picture in order to compare it with actual

at 9 km offshore for day 10 and day 15 in Fig. 21. We wish to include this picture in order to compare it with actual

observations in Section 5.4 and to illustrate the two-cell

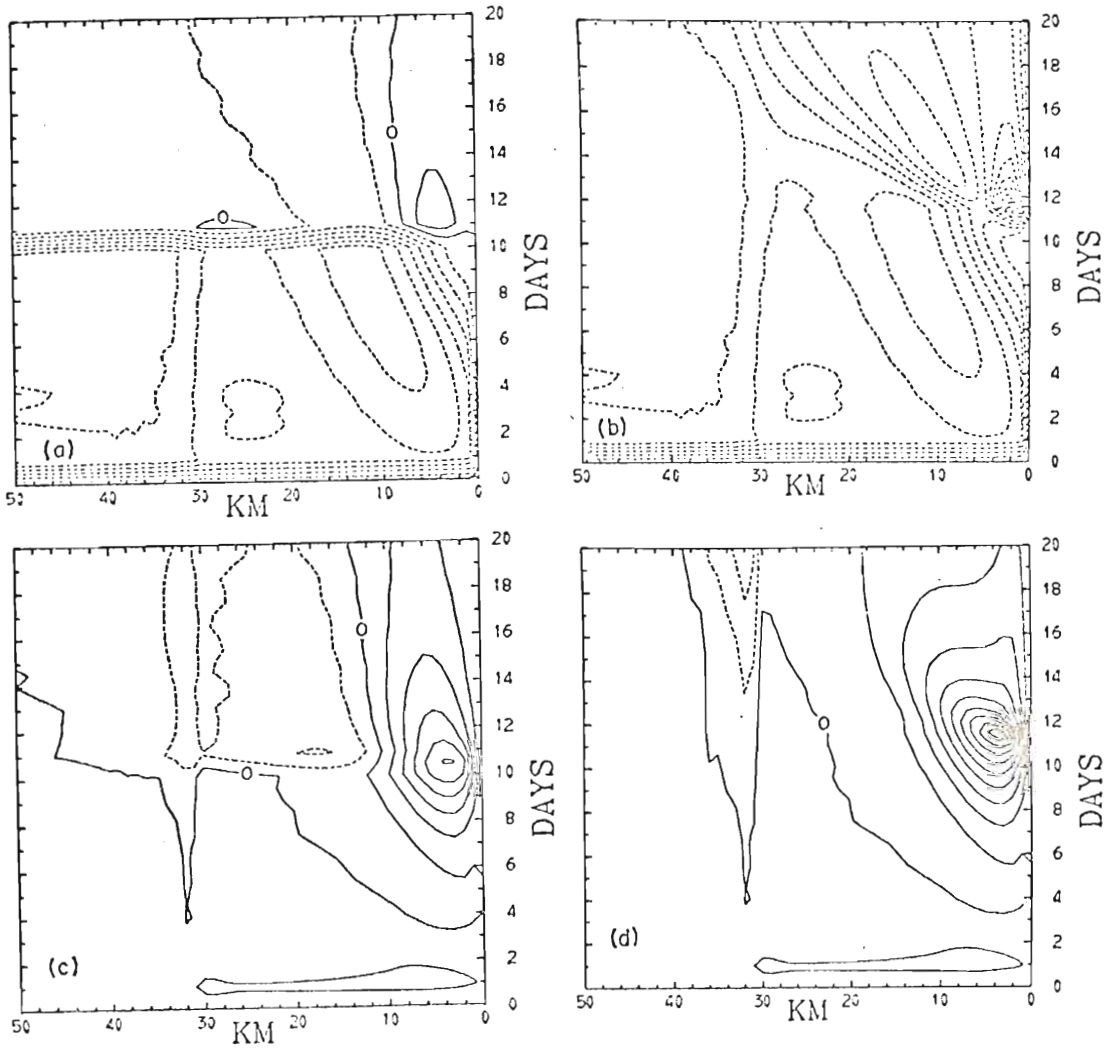

Fig. 20. Same as Fig. 19 but for the zonal flow components. Contour intervals are 1 cm sec^{-1} everywhere.

everywhere.

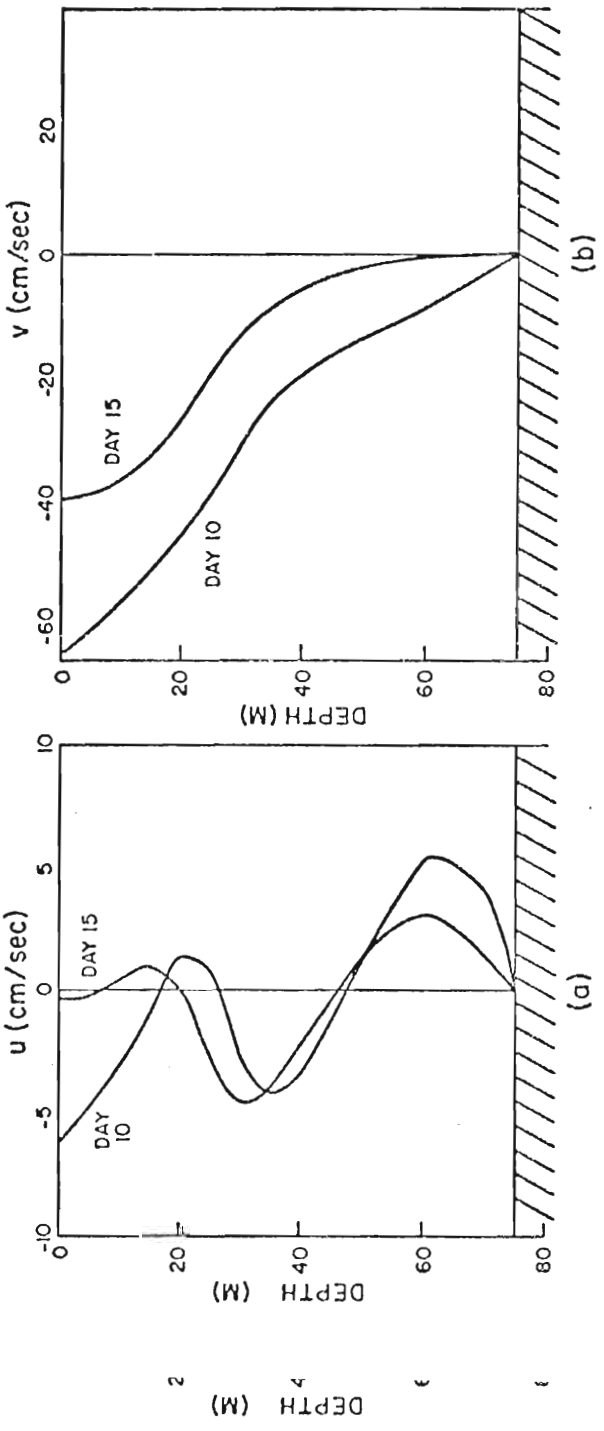

Fig. 21. Depth profiles of the zonal (a) and longshore (b) flow in the continental shelf event case at day 10 and 15, 9 km offshore.

circulation once more. Significantly the offshore flow at mid-depth remains nearly constant while the offshore flow near the surface and onshore flow near the bottom change substantially over the five-day period. We conclude that upwelling, once initiated, will continue for a significant period after the wind forcing is removed, due to the effects of longshore currents and current shears. However, in order to maintain upwelling in the nearest 20 m of the sea surface, i.e., in the biologically important euphotic zone, wind forcing is required. This wind forcing provides one-sided surface divergence near the coast and acts to raise the pycnocline.

5.3 Heating model

As stated earlier, we are limited to examining wind-dominated regimes, where colder water from below is entrained upwards into the mixed layer due to work done by turbulence against buoyancy forces. Consistent with the earlier work of Kraus and Turner (1967) and Denman (1973), it is found that the mixed layer thickens and cools during this process alone. Unfortunately, our model is not designed to accomodate a heat dominated regime, where all the available turbulent energy is used to mix warm surface water throughout the mixed layer, with none remaining to mix the interface downward. Nevertheless, moderate solar heating and the related effects of latent and sensible heat transfer and long-wave radiation can be included in this model. The principal restriction

is that heating processes at least be compensated by cooling due to vertical mixing and back-radiation. For strong heating our model is highly unrealistic, since it cannot account for formation of a new shallower layer above the original interface. Upon ignoring horizontal advection and diffusion in Eq. (10), the condition indicating transition from a wind-dominated to a heat-dominated regime is

$$\frac{\Delta\rho Q_1}{h_1} = \frac{\gamma H}{\rho_1 c_p h_1} ,$$

or

$$h_1 = \frac{\rho_0^{\,2}\, \phi u_*^{\,3}\, c_p}{g\gamma H} .$$

This form was first proposed by Kitaigorodskii (1960) using dimensional reasoning similar to that leading to the more renowned Monin-Obukhov length scale (Turner, 1973). Interestingly, Kitaigorodskii, on analyzing actual ocean data, found $\phi = 2$. Using realistic heating and wind forcing off Oregon during summer we find $h_1 \simeq 10$ m, the approximate depth of the seasonal thermocline.

Because of the high incidence of fog and low stratus during summer off Oregon moderate solar heating can be expected during the active upwelling season. Further, the extremely stable conditions arising from the cold SST's inhibit latent and sensible heat transfers. We have chosen to include this moderate solar radiation (with a diurnal

inhibit latent and sensible heat transfers. We have chosen to include this moderate solar radiation (with a diurnal cycle) and back radiation in the flat bottom and continetal shelf, continuously forced models described earlier. Latent

and sensible heat fluxes have been omitted. We are interested in exploring the effects of heating on the flow fields, the mixed layer depth, and the formation of the sea surface front.

Incident short-wave radiation was estimated using actual observations of radiation received on a horizontal surface at the ground along the Oregon coast in July (Decker, 1961). Cloudiness was estimated using Weather Service data summarized by Decker. For the case considered, clear sky short-wave radiation was taken as

$$R_0 = \begin{cases} \pi R_{00} \sin\left(\frac{2\pi t}{T}\right) & 0 \leq t \leq \left(\frac{2k-1}{2}\right) T \\ 0 & \frac{2k-1}{2} \leq t \leq kT \end{cases}$$

where $k = 1, 2 \ldots$, $R_{00} = 350$ Langleys day^{-1} and $T = 1$ day. Cloudiness and surface vapor pressure were assumed constant at 0.6 and 20 mb, respectively, during the integration period.

Fig. 22 depicts the SST's x-t section for the flat bottom and continental shelf heating models. The wind forcing is identical to that used earlier, with constant northerly wind stress after day 1. The diurnal component in the heating is only obvious very near the coast in both cases. When compared to Fig. 5d and Fig. 14c, it is clear that the maximum zonal temperature gradient is greater for the heating cases than for the non-heating cases.
that the maximum zonal temperature gradient is greater for the heating cases than for the non-heating cases.

Perhaps the effects of solar heating are best seen in Fig. 23, where offshore temperature profiles of mixed

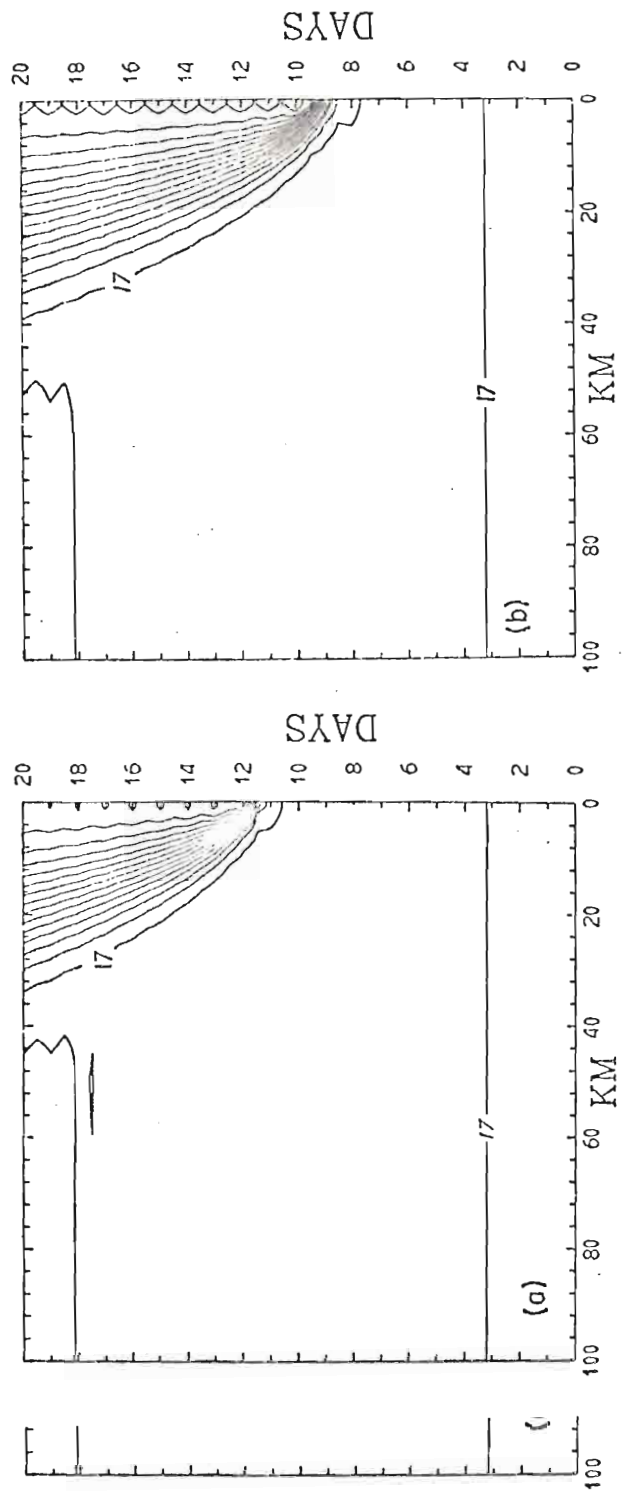

Fig. 22. Mixed-layer temperature x-t sections for the continuously forced continental shelf (a) and flat bottom (b) heated models. Contour intervals are 0.5°C.

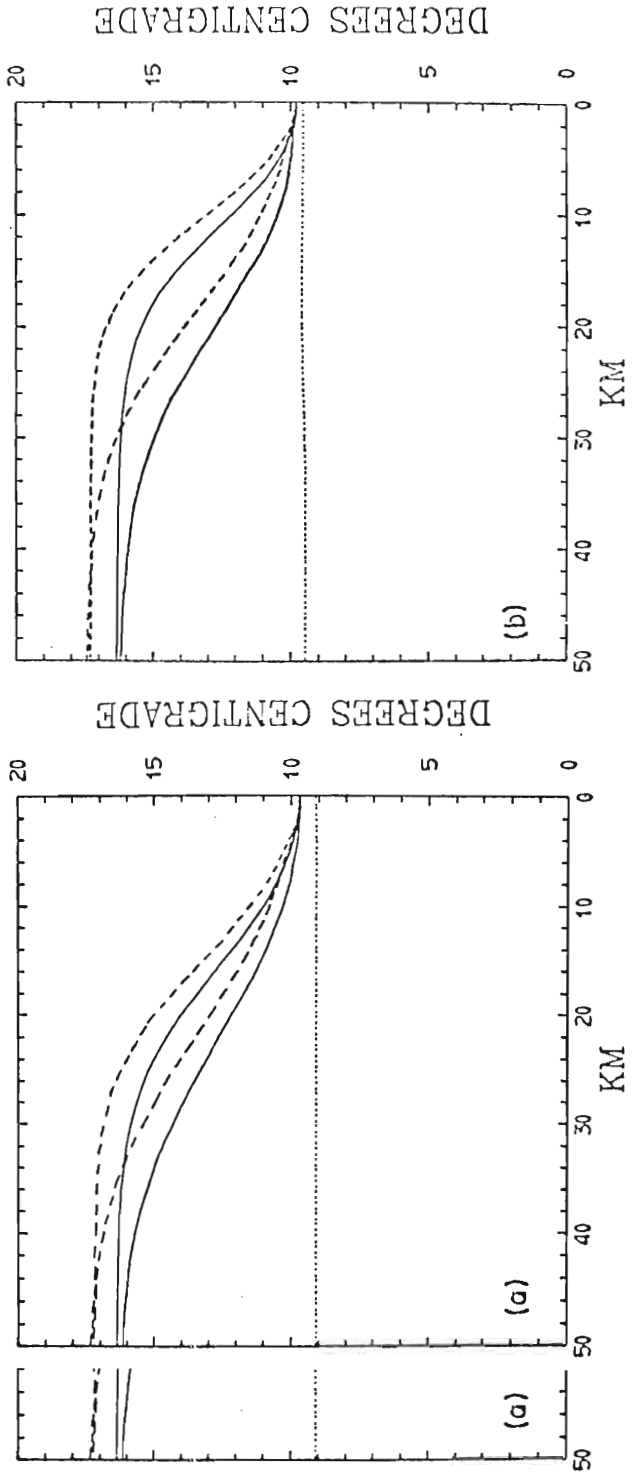

Fig. 25. Mixed-layer temperatures of the heated (dashed) and unheated (solid) continuously forced flat bottom (a) and continental shelf (b) cases at day 15 and 20.

layer temperature are plotted for heating and non-heating cases. The flat shelf and continental shelf model results at day 15 and day 20 are shown in Fig. 23a and 23b, respectively. Note that very near the coast little difference exists between heating and non-heating cases. Further offshore however the heated model is significantly warmer than the non-heated model. Consequently, the maximum SST zonal gradient is larger for the heated case. The substantial mixing near the coast and the effective heat sink represented by the lower layer are the principal reasons for this result. It is concluded that solar heating may strengthen the zonal SST contrast and may enhance frontal intensification.

Even with the addition of solar heating the frontal zone decays in time, as can be seen by comparing the day 15 and day 20 profiles for both models in Fig. 23. We have seen in the earlier results the horizontal diffusion and advection of heat weaken the front with either continuous forcing or with the event forcing. If indeed a quasi-steady frontal zone exists in actual upwelling situations over the seasonal time scale, it must be maintained by pulsations of the wind forcing, continually reinitiating the strong SST zonal gradients. In light of our results it is proposed that only a succession of coastal upwelling "events" over a season can maintain frontal structure. In our model steady wind forcing cannot lead to a steady coastal upwelling

front. Thus the wind "event" assumes even greater importance in the frontal dynamics of coastal upwelling.

To illustrate the effects of moderate heating on the depth of the mixed layer in this advective model, Fig 24a is included, where the depth of the mixed layer at 1 km and 4 km versus time for the heated and non-heated continental shelf model is shown. The effects of heating are not significant until after day 10, when the layer thickness becomes small. Briefly, the heating produces stronger stratification and hence turbulent energy must work against larger buoyancy forces to deepen the layer. Note the near-steady 8 m depth reached by the pycnocline at 1 km offshore after day 13.

The mixed-layer temperatures for the heated and non-heated continental shelf models are shown in Fig. 24b. Clearly in the heated model a steady (ignoring the diurnal variation) mixed-layer temperature is reached at 1 km offshore following a drastic temperature change near day 11. Although a steady temperature is also reached in the unheated model at 1 km, the absence of heating prevents maintenance of an equilibrium mixed-layer depth, as shown in Fig. 24a. In that case vertical mixing is balanced by horizontal diffusion and advection. Were the integrations extended past day 20 we expect that an equilibrium depth would be reached in the heated model at 4 km offshore also.

extended past day 20 we expect that an equilibrium depth would be reached in the heated model at 4 km offshore also.

Though there are weak effects of solar heating on the flow fields over the 20 day time integrations, we have chosen

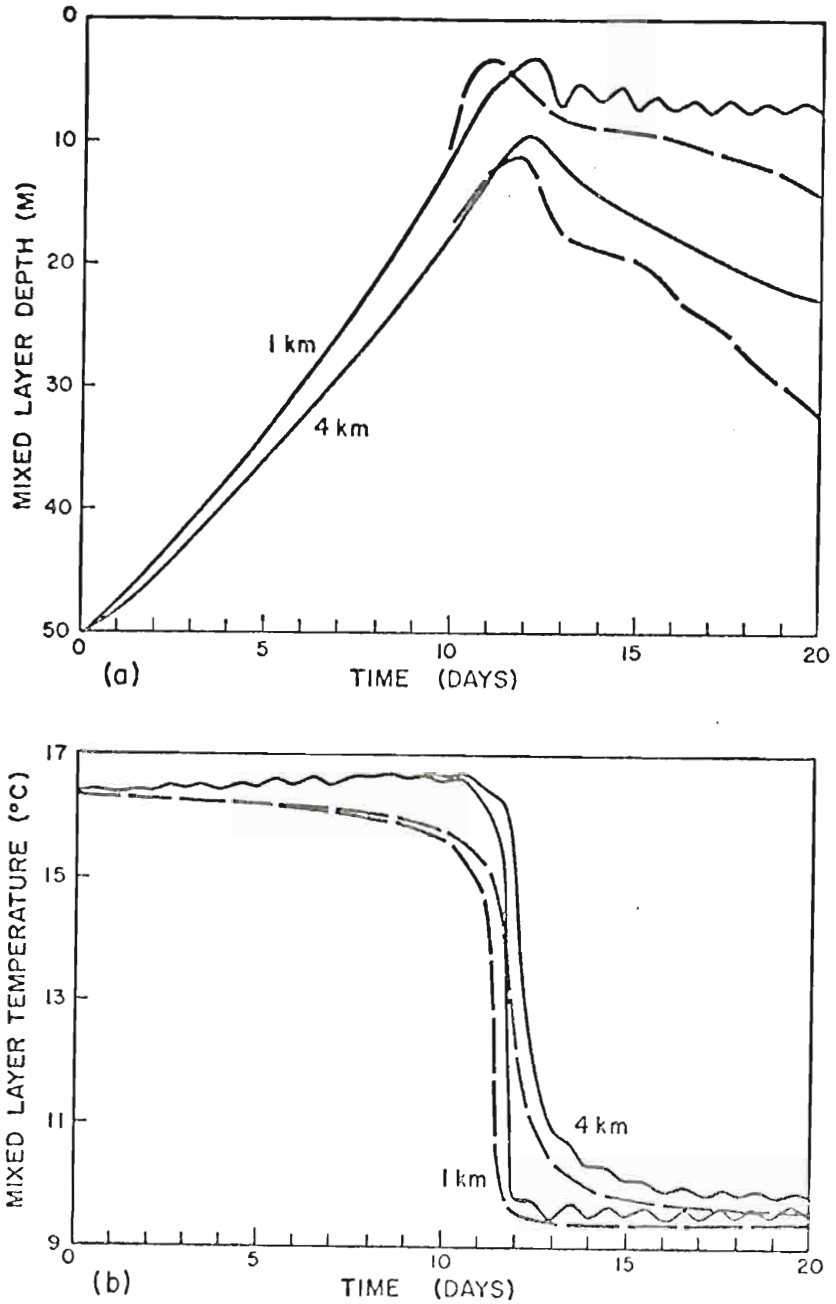

Fig. 24. Time series of mixed-layer depth (a) and temperature (b) at 1 km and 4 km offshore for the heated (solid) and unheated (dashed) continental

Fig. 24. Time series of mixed-layer depth (a) and temperature (b) at 1 km and 4 km offshore for the heated (solid) and unheated (dashed) continental shelf continuously forced case.

to omit discussion of them here. The main circulation features encountered in the unheated models are also found in these heated model runs. The principal differences arise in regions where solar heating alters the stratification substantially. Even in these areas qualitative differences in the circulations are not significant on the 20 day time scale. Obviously over an entire season the solar heating may substantially modify the flow patterns – but at present this model is much too crude to realistically account for them

5.4 Comparison with observations

In order to establish the credibility of the model it is desirable to compare model solutions with actual observations. This is a dangerous undertaking since such a highly idealized model cannot possibly account for the enormous complexity of the actual coastal upwelling process. The real situation is quite obviously three dimensional, with irregular wind forcing and bottom topography and propagating Kelvin waves. It is complicated by the effects of salinity and complex stratification and numerous other physical processes we have chosen to ignore. Nevertheless, if this model is to be instructive and useful to the physical oceanographer, biologist, or meteorologist at least its gross results must be grounded in observations.

biologist, or meteorologist at least its gross results must be grounded in observations.

In this subsection we have attempted to select from the observational literature results pertinent to this model.

One is reminded that these results, while in agreement with many of our findings, do not conclusively support our theories, since similar looking effects may be produced by quite dissimilar causes. These observations and comparisons are presented with the intent of establishing plausibility. It is not suggested that conclusive verification of this model lies in the cited observations.

During CUE I and CUE II held in 1972 and 1973 respectively off Oregon, a Barnes PRT-5 infrared radiometer was mounted from an NCAR Queen Air aircraft and used daily in SST mapping efforts. In 1973 a Sea Grant program provided a Barnes PRT-6 mounted on a light aircraft to map SST in an operational program to aid the Coho salmon fishery. Fig. 25a shows time series of SST along two lines perpendicular to the Oregon coast during an upwelling event in summer 1973 (Holliday, 1974). Data is presented for points 5, 10, and 15 km offshore. This figure should be compared with Fig. 7b and Fig. 24b. Note the rapid decreases of temperature during the first two days of observation. Since the sampling was only made once each day the rate of temperature decrease may be underestimated. Generally the coldest water is found nearest shore, the warmest at the seaward extremity.

In 1973 Bang presented a remarkable series of detailed BT transects of a frontal zone observed during an upwelling

In 1973 Bang presented a remarkable series of detailed BT transects of a frontal zone observed during an upwelling event in February, 1968 off Cape Town, South Africa (18°E, 36°S). His paper represents an extremely well-documented

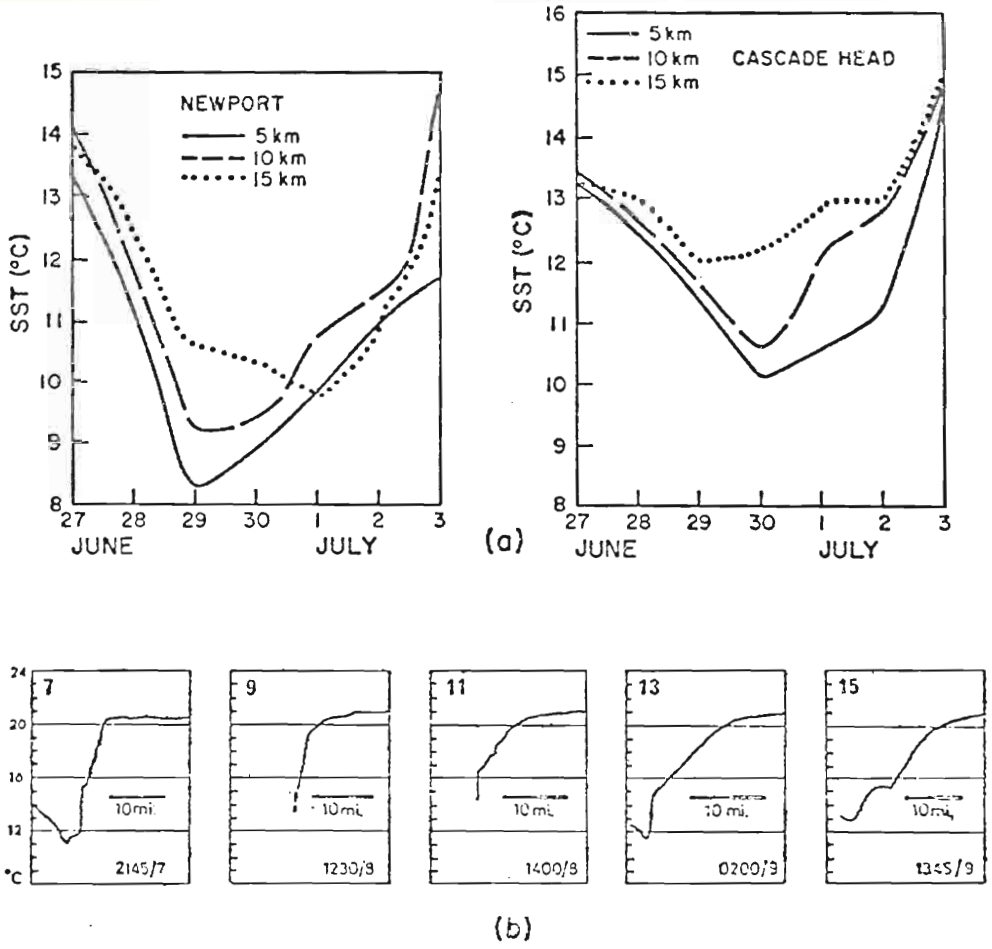

Fig. 25. (a) SST vs. time at 5, 10, and 15 km off Newport and Cascade Head, Oregon, during June 27-July 3, 1973 (after Holladay, 1974). (b) Frontal transect surface thermograph records during active upwelling 7-9 February, 1968 off Cape Town, South Africa (from Bang, 1973).

description of a surface front in an upwelling zone. Unfortunately, space limits us to include only one diagram from that study, Fig. 25b. In that figure Bang presents surface thermograph records for February 7 through February 9 during 5 transects through a frontal zone aligned parallel to the coast. Each transect was accomplished along approximately the same line. Meteorologically, strong southerly winds (8-12 m sec^{-1}) had begun to blow during the 5th and continued through the 7th, then the winds rapidly weakened, shifted to the north, where they blew strong northwesterly and westerly during the 8th, weakening on the 9th. Thus upwelling-favorable winds began the period, then diminished in strength during the remainder of the period.

Note that during the February 7 transect an intense frontal structure is observed near 5 km offshore. The zone is approximately 5 km wide and across it the SST change is nearly 13°C. During the next four transects the front weakens, and by 1345Z on February 9 the front has become broad (15 km in width) and the inshore temperature has increased slightly. The width scale, intensity, and temporal characteristics of this frontal zone are similar to those shown in our Fig. 23. Though our model does not account for the details of Bang's observations, the gross correspondence is encouraging. Finally, Bang notes that the

for the details of Bang's observations, the gross correspondence is encouraging. Finally, Bang notes that the frontal intensity responds very rapidly to changes in wind-

stress, citing dramatic changes in the intensity of the frontal zone within several hours.

Often the intense frontal regions are marked by long, well-defined foam lines of tidal rips and marked changes in water color. These dramatic features are well-documented in photographs and film clips taken during CUE-I and CUE-II. Having flown nearly 100 hours on the NCAR Queen Air in CUE-I during August, 1972 mapping SST off Oregon, this author has had many opportunities to view these characteristic features of coastal upwelling. In a more quantitative fashion Steveson et al. (1973) has succintly described the main features of those convergence zones from analysis of surface drogue movements during CUE-I in August, 1972. We quote their description of surface drogue movement during August 7, ". . . surface layer motion was clearly dominated by a convergent surface front located about 2.8 nautical miles offshore with a direction of 211°. The front could be seen readily because of the striking surface color difference on either side with inshore water a greener tone and offshore water more blue. The front or separation zone appeared to be no more than a few meters wide. Surface drogues deployed near the front were drawn rapidly into the frontal zone from both sides. At this point they were trapped, as water which had carried them there sank along the inclined frontal
both sides. At this point they were trapped, as water which had carried them there sank along the inclined frontal
layer. After reaching the front the drogues were useless as

indicators of fluid motion and merely indicated the position of the front, in common with other floating debris."

Clearly surface convergence zones depicted in our simple model (such as shown in Fig. 9a) may be found in the observations. We propose that the convergence zones are tenuous, depending upon a delicate balance between offshore Ekman drift, the gravitational circulation, and the intensity of frontal mixing. It is speculated that the color difference across the front may reflect difference in the circulation patterns seaward and shoreward of the front.

During active upwelling the model solutions indicate that strong vertical shear zones may be associated with offshore flow below the pycnocline and onshore flow above it. The resulting two-cell circulation is a common feature of both our flat-shelf and continental-shelf models. In Fig. 26a we have reproduced the schematic diagram presented by Mooers et al. (1973) which represents the mean cross-stream streamlines which are consistent with observations obtained during active upwelling in two successive years (1965 and 1966) off the Oregon coast using current meter and hydrographic data. The authors note that "the element of conjecture (in the figure) increases with depth and distance offshore."

The two-cell circulation is well-delineated in Fig. 26a. While the details of the circulation depicted by Mooers et al. (1973) are not directly comparable to our

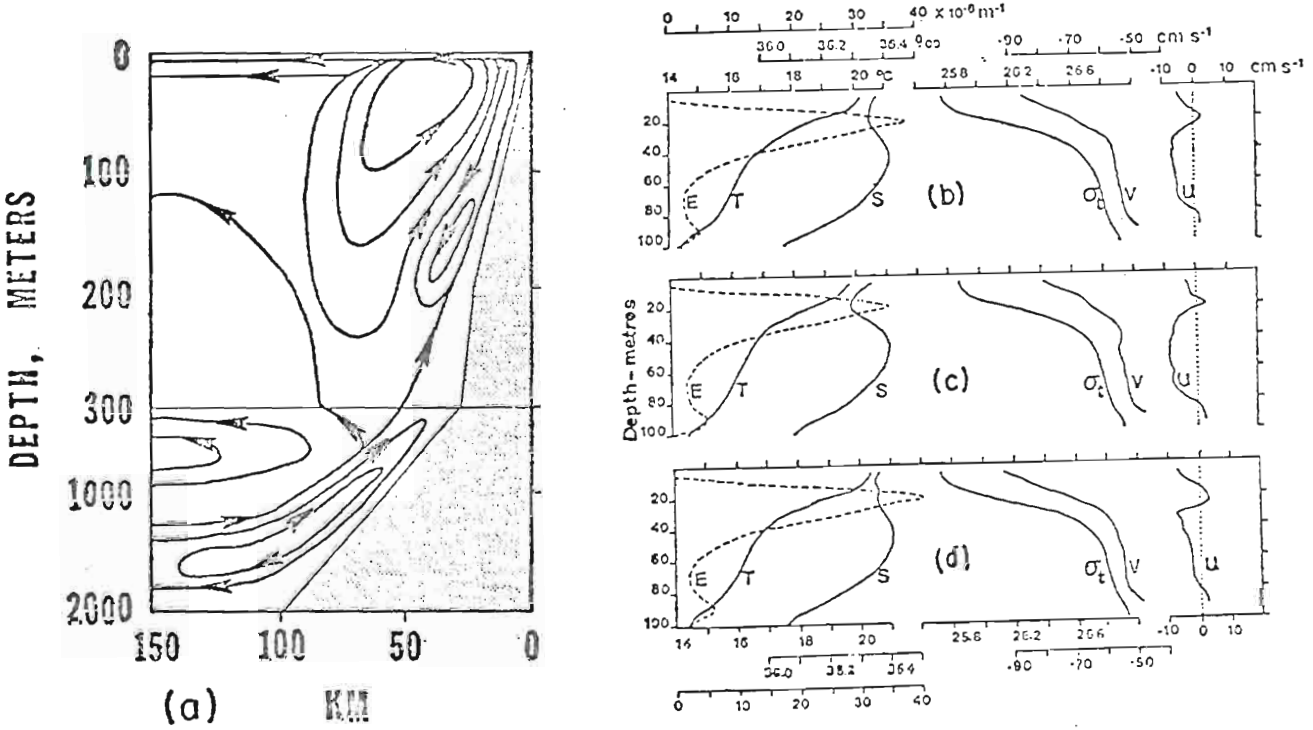

Fig. 26. (a) Conceptual diagram of the zonal flow during active upwelling off Oregon (from Mooers et al., 1973). Values of R, S, σ_t, static stability E, longshore speed v and onshore speed u for (b) the two-day mean and (c) and (d) for individual days at 26°01'N, 14°44'W during active upwelling in July and August, 1972, off NW Africa (from Hughes and Barton, 1973).

model results, due to differences in bottom topography, etc., the sense of the circulation agrees with our results. It is significant that Mooers et al. found "relatively high shear in both the axial and cross-stream flows in the inclined frontal layer."

Fig. 26b, c, d are reproduced from Hughes and Barton (1973), who presented mean profile of static stability, salinity, temperature, and velocity components (oriented along the bathymetry) off Northwest Africa (26°09'N, 14°44'W) during July and August, 1972. The observations were taken during active upwelling on Discovery cruise 48. A series of 98 half-hourly STD dips supplemented by 9 six-hourly profiling current meter dips (undertaken by Dr. Don Johnson, OSU) at a time series station situated in a depth of 105 m defined the circulation in a plane normal to the coast. Fig. 26b shows the overall means of each quantity while Fig. 26c and 26d present means for individual days.

Note that cross-stream flow in the upper region is offshore above 15 m and onshore in the region of maximum static-stability (15-25 m). A marked offshore flow is present below the stable layer down to 80 m, below which onshore flow is observed.

Figs. 26b, c, d should be compared with our continental shelf model results, Fig. 21. Again, the gross

Figs. 26b, c, d should be compared with our continental shelf model results, Fig. 21. Again, the gross

aspects of the circulation certainly agree. Notice that Hughes and Barton do not find a poleward-flowing undercurrent

over the continenal shelf. We find only a weak sporadic undercurrent in our sharp continental shelf configuration and, in fact, none appears at day 10, 9 km offshore in Fig. 21b.

Concerning the surface cyclonic and subsurface anti-cyclonic cells found just off the continental shelf of Northwest Africa by Mittelstaedt and Koltermann (1974), we find no evidence for such a circulation in our model results. However, it should be noted that their results are somewhat in question due to poor vertical resolution and the assumptions used in their analyses.

From these and other observations it seems clear that the two-cell circulation is an actual feature of at least some coastal upwelling regimes. While the offshore flow at the base of the pycnocline has been frequently described as a result of gravitationally unstable water sinking under warmer offshore water, we believe that the vertical current shears play an important role in driving the offshore subsurface current. This simple numerical-analytical model also simulates the onshore flow above the pycnocline.

Fig. 27 summarizes some observations concerning the poleward undercurrent and equatorward surface jet found off Oregon before (Fig. 27a) and during (Fig. 27b) CUE-I. Fig. 27a from Mooers et al. (1974) shows absolute geostrophic longshore velocity measurements off Depoe Bay in late
27a from Mooers et al. (1974) shows absolute geostrophic longshore velocity measurements off Depoe Bay in late
August, 1966. Two-week current averages at 20 and 60 meters depth, 10 km offshore; 20 meters depth, 20 km offshore; and

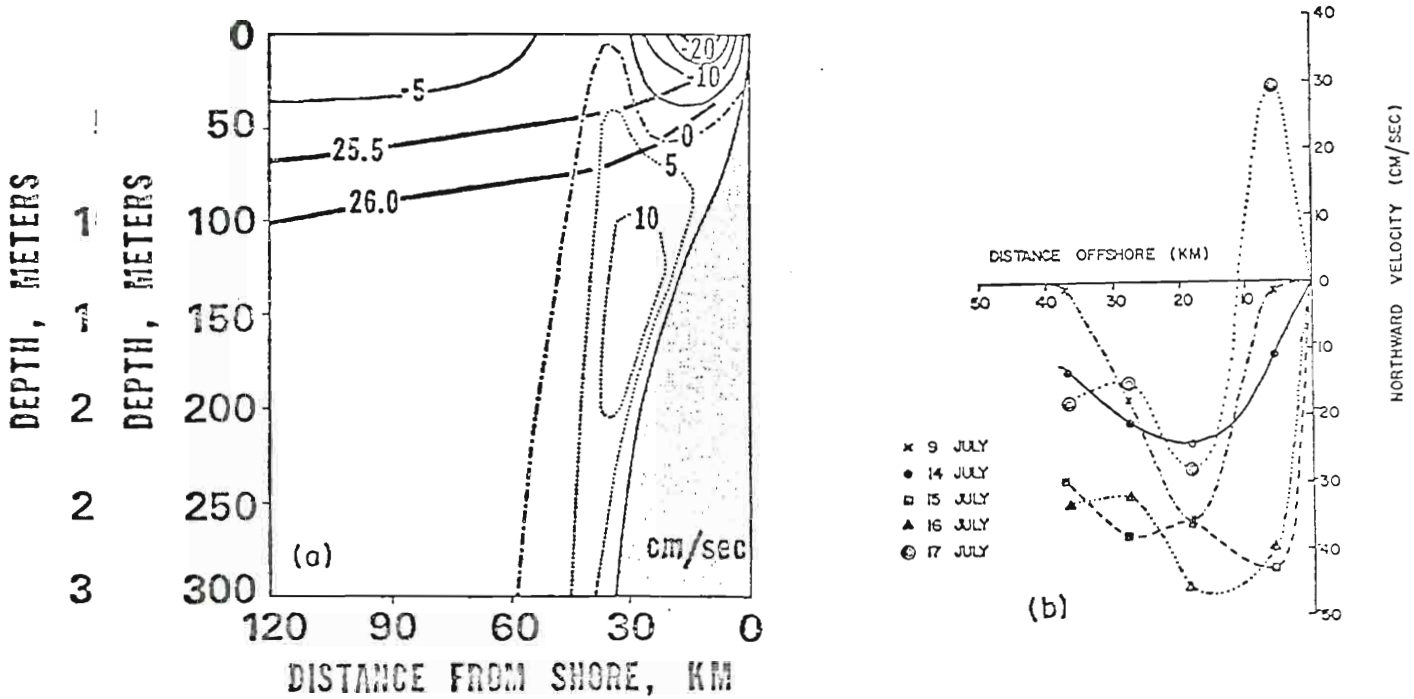

Fig. 27. (a) The absolute geostrophic longshore flow (two week average) off Depoe Bay during August, 1966 (from Mooers et al., 1973). (b) Northward component of the surface current vs. distance offshore off Oregon in July, 1972 (from Huyer, 1974).

60 meters depth, 30 km offshore were used to determine the absolute velocity from the relative geostrophic field. This diagram is most readily compared to Fig. 9d from our flat bottom case. Certainly the width scales for the surface and subsurface jets in the model correspond well with the observed fields. Though intensities are not comparable for the near-surface flow, this is not surprising considering the averaged nature of the observations.

Fig. 27b, taken from Huyer (1974), presents the longshore surface velocity estimated from observations off Oregon in July, 1972 during CUE-I. The jet structure is clearly evident in every case shown, though its shape varies substantially in time. It should be noted that surface winds were variable during this period, being most favorable for upwelling after July 13. These observed currents are certainly consistent with those produced in our model in terms of width scale and current amplitudes.

Though only a few of the observations from coastal upwelling studies have been presented, it seems clear that each major aspect of our model results does have an observational counterpart. While this establishes model plausibility, it by no means secures the model from criticism. This problem is considered in some detail below.

problem is considered in some detail below.

6. SUMMARY, CONCLUSIONS, AND CRITIQUE

Vertically-averaged equations for velocity, density, and thickness have been formulated for a time-dependent, nonlinear, two-layer model of coastal upwelling. The earth's rotation, bottom topography, the atmospheric pressure gradient, short and long-wave radiation, latent and sensible heat flux, parameterizations of horizontal and vertical turbulence, and barotropic and baroclinic modes are included in the formulation. Surface, interfacial, and bottom stresses and vertical mixing based on a parameterization of boundary and shear generated turbulence are incorporated in the model.

The vertically-averaged momentum equations are solved for the two-dimensional problem using a highly-efficient semi-implicit numerical scheme and a discrete variation telescoping grid which allows high resolution near the coast. Because solutions in the upwelling zone require a realistic interior ocean the model width is greater than 1000 km. Both a Sverdrup interior balance and westward propagating Rossby waves exist in the model solutions. Perturbation equations for momentum are developed and solved analytically to account for Ekman-like boundary layers occurring in high vertical shear zones near the surface, pycnocline, and bottom

for Ekman-like boundary layers occurring in high vertical shear zones near the surface, pycnocline, and bottom.

For model cases with and without bottom topography, solar heating, and continuosu wind forcing several features often observed in actual coastal upwelling regimes are simulated. These include (1) the strong sea surface temperature gradients which appear within 50 km of the coast, (2) the equatorward surface jet and poleward undercurrent often found within the baroclinic Rossby radius of deformation, and (3) the two cyclonically rotating cells reported by Mooers et al. (1973) as situated in a plane normal to and within 50 km of the coast. Due to horizontal diffusion and advection and vertical mixing the sea surface temperature front produced during active upwelling is found to decay both upon cessation of the wind and during continuous forcing. It is conjectured that periodic forcing "events" are necessary to maintain the mean position and intensity of the observed upwelling fronts. Solar heating appears to enhance frontal intensity.

As a result of this research several coastal upwelling observational studies are proposed:

(a) Profiling current meters be used in areas of relatively uniform north-south topography to investigate the transhore circulation. Of particular value would be high resolution measurements of the vertical current structure in the pycnocline region during active upwelling.

(b) Transects across an intense frontal zone be made frequently for a several day period during and following coastal upwelling. Are the spatial scales of the

surface temperature gradients comparable to the width scales of surface convergence zones? Does the front decay during continuous equatorward wind forcing as predicted by the model?

(c) Detailed measurements of the near-bottom flow over the continental shelf and shelf slope be obtained during and following intense upwelling activity.

On the basis of the model results, it is predicted that the transhore two-cell circulation can be consistently observed when:

(1) There exists a strong shear zone (order of cm's sec^{-1} m^{-1}) during active upwelling in the region of the permanent pycnocline concurrent with an equatorward surface flow and a poleward undercurrent; and

(2) the flow fields are not severely complicated by capes, bays, and highly irregular submarine topography.

It is also speculated that subsurface near shore upwelling may continue several days after cessation of the wind. Such subsurface motion ($10^{-3} - 10^{-2}$ cm sec^{-1}) could be measured directly from a fixed platform mounted on the ocean bottom, using the recently developed Laser Doppler Velocimeter (Fowlis, Thompson, and Terry, 1974).

In contrast to our model formulation coastal upwelling is not two-dimensional, its turbulent motions are most likely

In contrast to our model formulation coastal upwelling is not two-dimensional, its turbulent motions are most likely

poorly represented by constant eddy coefficients and Fickian diffusion, and it is rarely defined by a simple two-layer

system. At best the model is a crude approximation to the actual coastal upwelling situation. Nevertheless, this combined numerical-analytical model of coastal upwelling has provided substantial insight into the basic upwelling dynamics. Certainly the model results are compatible with many observations obtained in upwelling areas. For example, the spatial and temporal characteristics of the sea-surface temperatures and currents predicted by the model are in reasonable agreement with observations obtained off Oregon during CUE-I and CUE-II. The intense upwelling, the two-cell circulation, the equatorward surface jet, and the poleward undercurrent are features predicted by the model and observed at least periodically, off the Oregon coast.

At this time we are proceeding, in collaboration with Dr. H. E. Hurlburt, to include three-dimensionality in a thermodynamic-hydrodynamic model of the eastern ocean circulation. The effects of longshore advection of heat on coastal upwelling will be investigated in this new model. Methods are being devised to include the physics of the heat-dominated regime in the model equations, perhaps in the manner of Denman (1973). It is most desirable to include a seasonal thermocline in the model formulation. Various new parameterization schemes for turbulent processes are also being considered. In the near future this ocean model

new parameterization schemes for turbulent processes are also being considered. In the near future this ocean model

will be coupled with an atmospheric model in order to

investigate mesoscale air-sea interactions during the upwelling season. Of particular interest is the feedback between coastal upwelling and the sea breeze.

APPENDICES

APPENDIX A

LIST OF SYMBOLS

A_H, A_V	horizontal and vertical eddy viscosities
B	Bowen's ratio
C_1, C_2	heat content per unit area for the upper and lower layer
c_I, c_B	interfacial and bottom drag coefficients
c_p	specific heat of sea water at constant pressure
c_R	phase speed for barotropic Rossby wave
D	height of the bottom topography above a reference level
e, e_w	ship level vapor pressure, saturated ship level vapor pressure
f	Coriolis parameter
g	acceleration of gravity
g'	reduced gravity
h_1, h_2	instantaneous thickness of upper and lower layers
h_m	minimum thickness of a layer
H	heating function
H'	Heaviside unit function
H_1, H_2	initial thickness of upper and lower layers
H_L, H_S	latent and sensible heat flux
H_1, H_2	initial thickness of upper and lower layers
H_L, H_S	latent and sensible heat flux
k_0	von Karman's constant

K_H, K_V	horizontal and vertical density diffusion coefficients
L	total width of the model basin – also used as a vertical length scale
m	the fraction of downward flux of turbulent energy of the wind field available for mixing in the layer
M_1, M_2	mass per unit area for the upper and lower layer
n	cloudiness in tenths
P_A	the atmospheric pressure at sea level
Q_1, Q_2	entrainment rates for the upper and lower layers
r	ratio of vapor pressure to saturated vapor pressure
R, R_0	short wave radiation penetrating the sea surface
R_i, R_L	bulk Richardson number and critical bulk Richardson number
t	time
T_1, T_2	vertically-averaged temperature for the upper and lower layer
T_V, T_H	vertical and horizontal diffusion time scales
u, v	x and y-directed total velocity components
$\bar{u}$	maximum zonal advective speed in the model
u_1, u_2	x-directed vertically-averaged components of current velocity
u_*, u_{*B}	surface and bottom friction velocity
v_1, v_2	y-directed vertically-averaged components of current velocity
w_1, w_2	complex perturbation velocities current velocity
w_1, w_2	complex perturbation velocities
w_I	vertical velocity at the interface
x,y,z	tangent-plane Cartesian coordinates: x positive northward, z positive upward

β	df/dy
γ	effective coefficient of thermal expansion for sea water
$\vec{\nabla}$	horizontal del operator $\frac{\partial}{\partial x}\hat{i} + \frac{\partial}{\partial y}\hat{j}$
$\Delta\rho$	density contrast between layers, $\rho_2 - \rho_1$
Δt	time increment in the numerical integration
Δx	horizontal grid increment in the x direction
ζ	vertical component of vorticity
λ	baroclinic radius of deformation
ρ_0	reference density for sea water
ρ_1, ρ_2	vertically-averaged densities of sea water
σ	Stefan-Boltzman constant
$\tau_{Sx}, \tau_{Ix}, \tau_{Bx}$	x-directed tangential stresses at the surface, interface, and bottom
$\tau_{Sy}, \tau_{Iy}, \tau_{By}$	y-directed tangential stresses at the surface, interface, and bottom
ϕ	constant of proportionality relating the ratio of entrainment rate and friction velocity to inverse Richardson number

APPENDIX B

HORIZONTAL MIXING FORMULATION

Consider the equation for conservation of momentum for the upper layer

$$\frac{\partial}{\partial t}(\rho_1 h_1 \vec{v}_1) + \vec{v}_1 \cdot \nabla(\rho_1 h_1 \vec{v}_1) + \rho_1 h_1 \vec{v}_1 (\nabla \cdot \vec{v}_1) = \vec{F} \quad \text{(B-1)}$$

where $\vec{F}$ represents momentum transfer processes through the top or bottom of the column. We desire to derive an equation for the mean flow, following the usual Reynolds' averaging procedure in accounting for subgrid scale horizontal turbulence.

The component equation for the total zonal momentum can be written

$$\frac{\partial}{\partial t}(\rho_1 h_1 u_1) + \frac{\partial}{\partial x}(\rho_1 h_1 u_1 u_1) + \frac{\partial}{\partial y}(\rho_1 h_1 u_1 v_1) = F_x. \quad \text{(B-2)}$$

On writing the quantities ρ_1, u_1 and v_1 in terms of a spatial mean and a departure from the mean and averaging the resulting equation over a suitable length scale we obtain

$$\frac{\partial}{\partial t}(h_1 \overline{\rho_1 u_1}) + \frac{\partial}{\partial x}(h_1 \overline{\rho_1 u_1 u_1}) + \frac{\partial}{\partial y}(h_1 \overline{\rho_1 u_1 v_1}) + \frac{\partial}{\partial x}(h_1 \rho_1 \overline{u_1' u_1'}) + \frac{\partial}{\partial y}(h_1 \rho_1 \overline{u_1' v_1'}) = \overline{F}_x. \quad \text{(B-3)}$$

$$\frac{\partial}{\partial x}(h_1 \rho_1 \overline{u_1' u_1'}) + \frac{\partial}{\partial y}(h_1 \rho_1 \overline{u_1' v_1'}) = \overline{F}_x. \quad \text{(B-3)}$$

In deriving (B-3) we have assumed that triple correlations are negligible and that correlations between departures in density and velocity are small compared to those between velocity components.

On defining

$$\overline{u_1' u_1'} = - A_H \frac{\partial \bar{u}}{\partial x}$$

$$\overline{u_1' v_1'} = - A_H \frac{\partial \bar{u}}{\partial y}$$

and dropping the bar notation

$$\frac{\partial}{\partial t}(\rho_1 h_1 u_1) + \frac{\partial}{\partial x}(h_1 \rho_1 u_1 u_1) + \frac{\partial}{\partial y}(\rho_1 h_1 u_1 v_1) = F_x + \frac{\partial}{\partial x}\left(\rho_1 h_1 A_H \frac{\partial u_1}{\partial x}\right) + \frac{\partial}{\partial y}\left(\rho_1 h_1 A_H \frac{\partial u_1}{\partial y}\right). \quad \text{(B-4)}$$

The general vector expression is

$$\frac{\partial}{\partial t}(\rho_1 h_1 \vec{v}_1) + \vec{v}_1 \circ \nabla(\rho_1 h_1 \vec{v}_1) + \rho_1 h_1 \vec{v}_1 (\nabla \circ \vec{v}_1) = F + (\nabla \circ (\rho_1 h_1 A_H \nabla))\, \vec{v}_1 . \quad \text{(B-5)}$$

Utilization of the mass conservation equation coupled with simple algebraic manipulation yields the more familiar form

$$\frac{\partial \vec{v}_1}{\partial t} + \vec{v}_1 \circ \nabla \vec{v}_1 = \vec{G} + A_H \nabla^2 \vec{v}_1 + \frac{[\nabla(\rho_1 h_1 A_H) \circ \nabla]\vec{v}_1}{\rho_1 h_1} , \quad \text{(B-6)}$$

where $\vec{G}$ represents vertical turbulent momentum transfers across the bottom or top of the fluid column. On scaling

where G represents vertical turbulent momentum transfers across the bottom or top of the fluid column. On scaling

the last two terms of (B-6), the last term is found to be approximately $\Delta h_1 / h_1$ times the magnitude of the second term,

where Δh_1 represents the departure of the upper layer thickness from its undisturbed value. For regions where h_1 is small (i.e., near-surfacing of the pycnocline) $\Delta h_1/h_1$ may be O(1). Clearly, the term involving a depth-weighted eddy viscosity may be significant and should be retained.

APPENDIX C

VERTICAL MOMENTUM TRANSPORTS

Consider the vertical transports of momentum which accompany vertical exchanges of mass in a turbulent stratified fluid. From the second law of thermodynamics, we expect that energy of organized motions, converted to horizontal or vertical turbulence, will ultimately be dissipated as thermal energy. Therefore any parameterization of turbulent mixing processes must lead to a dissipation of the net energy in the fluid system. Assume the momentum in a column of fluid of unit cross-sectional area has density ρ_1, thickness h_1, and velocity $\vec{v}_1$. Examining only the process of mixing across the interface, the conservation of momentum equation for the upper layer is

$$\frac{\partial}{\partial t}(\rho_1 h_1) + \vec{v}_1 \cdot \nabla(\rho_1 h_1 \vec{v}_1) + \rho_1 h_1 \vec{v}_1 (\nabla \circ \vec{v}_1) = \vec{v}_2 \rho_2 Q_1 - \vec{v}_1 \rho_1 Q_2 \,, \tag{C-1}$$

and for the lower layer

$$\frac{\partial}{\partial t}(\rho_2 h_2) + \vec{v}_2 \circ \nabla(\rho_2 h_2 \vec{v}_2) + \rho_2 h_2 \vec{v}_2 (\nabla \circ \vec{v}_2) =$$

$$\frac{\partial}{\partial t}(\rho_2 h_2) + \vec{v}_2 \circ \nabla(\rho_2 h_2 \vec{v}_2) + \rho_2 h_2 \vec{v}_2 (\nabla \circ \vec{v}_2) = \vec{v}_1 \rho_1 Q_2 - \vec{v}_2 \rho_2 Q_1 \,, \tag{C-2}$$

where Q_1 represents entrainment of lower layer fluid into the upper layer and Q_2 represents entrainment of upper layer fluid into the lower layer. The particular forms of Q_1 and Q_2 are unimportant except that each is a positive definite quantity. (There can be no un-mixing.)

Using the conservation of mass equation in (C-1) and (C-2), we obtain

$$\frac{\partial \vec{v}_1}{\partial t} + \vec{v}_1 \cdot \nabla \vec{v}_1 = \frac{\rho_2 Q_1 (\vec{v}_2 - \vec{v}_1)}{\rho_1 h_1} , \qquad \text{(C-3)}$$

$$\frac{\partial \vec{v}_2}{\partial t} + \vec{v}_2 \cdot \nabla \vec{v}_2 = \frac{-\rho_1 Q_2 (\vec{v}_2 - \vec{v}_1)}{\rho_2 h_2} . \qquad \text{(C-4)}$$

From (C-3) one finds that total changes in momentum per unit mass for the upper layer depend upon Q_1 and not Q_2. This is reasonable since only additions of mass with momentum differing from that already in the layer changes the momentum per unit mass in that layer. Likewise, if $v_2 = v_1$ then no change in momentum per unit mass occurs in the layer during mixing. A similar argument holds in the lower layer. Defining the kinetic energy as

$$(KE)_i = 1/2 \; \rho_i h_i |\vec{v}_i|^2 , \quad i = 1, 2 \qquad \text{(C-5)}$$

kinetic energy equations can be formed from (C-3) and (C-4),

$$\frac{\partial}{\partial t}\left[\frac{\rho_1 h_1 |\vec{v}_1|^2}{2}\right] + \nabla \cdot \left[\frac{\rho_1 h_1 |\vec{v}_1|^2 \vec{v}_1}{2}\right] = \qquad \text{(C-6)}$$

$$\frac{\partial}{\partial t}\left[\frac{\rho_1 h_1 |\vec{v}_1|^2}{2}\right] + \nabla \cdot \left[\frac{\rho_1 h_1 |\vec{v}_1|^2 \vec{v}_1}{2}\right] = |\vec{v}_1|^2 - \qquad \text{(C-6)}$$

$$\rho_2 Q_1 \vec{v}_1 \cdot (\vec{v}_2 - \vec{v}_1) + \frac{|\vec{v}_1|^2}{2}\left[\rho_2 Q_1 - \rho_1 Q_2\right]$$

and

$$\frac{\partial}{\partial t}\left[\frac{\rho_2 h_2 |\vec{v}_2|^2}{2}\right] + \nabla \circ \left[\frac{\rho_2 h_2 |\vec{v}_2|^2 \vec{v}_2}{2}\right] = \tag{C-7}$$

$$\rho_1 Q_2 \vec{v}_2 \circ (\vec{v}_1 - \vec{v}_2) + \frac{|\vec{v}_2|^2}{2}(\rho_1 Q_2 - \rho_2 Q_1) .$$

Examination of (C-6) and (C-7) reveals several important aspects of the mixing process. First note that in a layer, mixing may <u>increase</u> the kinetic energy. The second term on the right-hand side of (C-6) and (C-7) represents the net effect of the entrainments in transferring mass and energy. If $\rho_2 Q_1 > \rho_1 Q_2$, then that term represents an addition to the total kinetic energy in the upper layer and a depletion for the lower layer.

The first term on the right-hand side of (C-6) and (C-7) represents the effect of vertical current shear in transmitting energy upward or downward. When expanded, the terms contain an energy transfer ($\vec{v}_1 \circ \vec{v}_2$) and a dissipation ($-|\vec{v}_1|^2$, $-|\vec{v}_2|^2$).

Upon addition of (C-6) and (C-7) we obtain the total kinetic energy for the column,

$$\frac{\partial}{\partial t}(KE_1 + KE_2) + \nabla \circ (KE_1 \vec{v}_1 + KE_2 \vec{v}_2) = \tag{C-8}$$

$$- \rho_1 Q_2 (\vec{v}_1 - \vec{v}_2)^2 - \rho_2 Q_1 (\vec{v}_1 - \vec{v}_2)^2$$

Clearly the right-hand side of (C-8) is always negative or zero. Hence the mixing process, as we have parameterized it, does indeed dissipate the kinetic energy in the column.
zero. Hence the mixing process, as we have parameterized it, does indeed dissipate the kinetic energy in the column.
This is consistent with physical reasoning and the second law of thermodynamics.

APPENDIX D

SOLUTION OF THE FINITE DEPTH EKMAN-THERMAL WIND EQUATIONS

The upper region problem discussed in Section 3 with $z = 0$ the sea surface, $z = b$ the pycnocline and $z = c$ the bottom is

$$\frac{\partial^3 w_1}{\partial z^3} - s^2 \frac{\partial w_1}{\partial z} = G_1, \quad b \leq z \leq 0 \tag{D-1}$$

$$\left.\begin{aligned} &\text{with } \int_b^0 w_1 dz = 0 , \\ &\frac{\partial w_1}{\partial z} = \frac{\tau_{sx}}{A_v} + i \frac{\tau_{sy}}{A_v} = P, \quad z = 0 , \\ &\text{and } \frac{\partial w_1}{\partial z} = \frac{\partial w_2}{\partial z} = Q, \quad z = b . \end{aligned}\right\} \tag{D-2}$$

The solution to (D-1) to (D-3) is

$$w_1 = \frac{A_1 e^{sz}}{s} - \frac{B_1 e^{-sz}}{s} - \frac{G_1 z}{s^2} + C_1 \tag{D 3}$$

where

$$\left.\begin{aligned} A_1 &= P - B + \frac{G_1}{s^2} , \\ B_1 &= \left(P e^{sb} - Q + \frac{G_1}{s^2} (e^{sb} - 1) \right) \operatorname{csch}(sb) , \\ B_1 &= \left(P e^{A_1} - Q + \frac{G_1}{s^2} (e^{B_1} - 1) \right) \operatorname{csch}(sb) C_1 , \\ C_1 &= \frac{1}{b} \left(\frac{A_1}{s^2} (1 - e^{sb}) + \frac{B_1}{s^2} (1 - e^{-sb}) + \frac{C_1}{2s^2} b^2 \right) . \end{aligned}\right\} \tag{D-4}$$

The upper solution (D-3) is coupled to the lower solution by the boundary condition $Q = \partial w_2/\partial z$, at $z = b$.

The lower region problem is

$$\frac{\partial^3 w_2}{\partial z^3} - s^2 \frac{\partial w_2}{\partial z} = G_2, \quad c \leq z \leq b , \tag{D-5}$$

with

$$\left.\begin{aligned} &\int_c^b w_2 \, dz = 0 , \\ &w_2(b) = w_1(b) + \Delta v = J , \\ \text{and} \quad &w_2(c) = K , \\ \text{where} \quad &\Delta v = (u_1 - u_2) + i(v_1 - v_2) , \\ \text{and} \quad &K = -(u_2 + iv_2) . \end{aligned}\right\} \tag{D-6}$$

The solution for (D-5) is of the form

$$w_2 = \frac{A_2 e^{sz}}{s} - \frac{B_2 e^{sz}}{s} - \frac{G_2 z}{s^2} + C_2 , \tag{D-7}$$

where

$$\left.\begin{aligned} A_2 &= \frac{s}{\alpha_1}\left[K\gamma_3 + \frac{G_2\alpha_3}{s^2} + \frac{B_2\alpha_2}{s}\right] , \\ B_2 &= s\left[\frac{K\gamma_1\gamma_3 - \alpha_1(J-K) - \frac{G_2}{s^2}(\alpha_1\gamma_3 - \alpha_3\gamma_1)}{\alpha_1\gamma_2 - \alpha_2\gamma_1}\right] \\ C_2 &= J - \frac{A_2 e^{sb}}{s} + \frac{B_2 e^{-sb}}{s} + \frac{G_2 b}{s^2} . \end{aligned}\right\} \tag{D-8}$$

Also, $\alpha_1 = e^{sc}\gamma_3 - \frac{\gamma_1}{s}$,

$\alpha_2 = e^{-sc}\gamma_3 + \frac{\gamma_2}{s}$,

$\alpha_3 = -\frac{(\gamma_3)^2}{2}$,

$\gamma_1 = e^{sb} - e^{sc}$,

$\gamma_2 = e^{-sb} - e^{-sc}$,

and $\gamma_3 = b - c$.

Clearly w_2 is coupled to w_1 through the boundary condition $w_2(b) = w_1(b) + \Delta v$, and thus is related to the mean vertical current shear.

The remaining task is to solve (D-1) through (D-8) for Q and J. Recall that

$$Q = \frac{\partial w_2(b)}{\partial z} = A_2 e^{sb} + B_2 e^{-sb} - \frac{G_2}{s^2} . \qquad \text{(D-9)}$$

On substituting for A_2 and B_2 in (D-9) and collecting terms

$$Q = Y - \varepsilon J , \qquad \text{(D-10)}$$

where

$$\left.\begin{aligned} Y &= X + \left[\frac{1}{\alpha_1\gamma_2 - \alpha_2\gamma_1}\right]\left[\mu s K \gamma_1\gamma_3 + \mu s \alpha_1 K - \frac{\mu G_2(\alpha_1\gamma_3 - \alpha_3\gamma_1)}{s}\right] \\ X &= \frac{K\gamma_3 s e^{sb}}{\alpha_1} + \frac{G_2\alpha_3 e^{sb}}{s\alpha_1} - \frac{G_2}{s^2} , \\ \varepsilon &= \frac{\mu s \alpha_1}{\alpha_1\gamma_2 - \alpha_2\gamma_1} , \qquad \text{(D-11)} \\ \varepsilon &= \frac{\mu s \alpha_1}{\alpha_1\gamma_2 - \alpha_2\gamma_1} , \qquad \text{(D-11)} \end{aligned}\right\}$$

and

$$\mu = \frac{\alpha_2}{\alpha_1} e^{sb} + e^{-sb} .$$

Set

$$J' = J - \Delta v = \frac{A_1 e^{sb}}{s} - \frac{B_1 e^{-sb}}{s} - \frac{G_1 b}{s^2} + C_1 \ . \qquad \text{(D-12)}$$

Upon substituting for A_1, B_1, and C_1 and collecting terms

$$J' = R + Q\eta \ , \qquad \text{(D-13)}$$

where

$$\left.\begin{aligned} R &= \frac{P_1\delta_1}{s} + \frac{G_1\delta_3}{2} \ , \\ \eta &= \frac{1}{s}\left[\coth sb - \frac{1}{sb}\right] \ , \\ \delta_1 &= e^{sb}\,(1 - \coth sb) + \frac{1}{sb} \ , \\ \delta_2 &= \coth sb - \frac{1}{sb} \ , \\ \delta_3 &= \frac{e^{sb}}{s}\,(1 - \coth sb) + \frac{\coth sb}{s} - \frac{b}{2} \ , \\ \lambda_1 &= e^{sb} + \frac{1 - e^{sb}}{sb} \ , \\ \text{and} \quad \lambda_2 &= -\frac{(1 - e^{-sb})}{sb} + e^{-sb} \ . \end{aligned}\right\} \qquad \text{(D-14)}$$

On solving for J and Q using (D-10) and (D-13)

$$\left.\begin{aligned} Q &= \frac{Y - \varepsilon(R + \Delta v)}{1 + \varepsilon\eta} \ , \\ \text{and} \\ J &= \frac{R + [Y - \varepsilon(R + \Delta v)]}{1 + \varepsilon\eta} \ . \end{aligned}\right\} \qquad \text{(D-15)}$$

REFERENCES

Allen, J. S., 1973: Upwelling and coastal jets in a continuously stratified ocean. J. Phys. Oceanogr., 3, 245-257.

Bang, N. D., 1973: Characteristics of an intense ocean frontal system in the upwell regime west of Cape Town. Tellus, 25, 256-265.

Bates, J. R., 1973: A generalization of the CISK theory. J. Atmos. Sci., 30, 1509-1519.

Budyko, M. I., 1956: The heat balance of the earth's surface. Translated from Russian by Office of Technical Services, U.S. Department of Commerce, 1966, 255 pp.

Charney, J. G., 1955: The generation of oceanic currents by wind. J. Marine Res., 14, 477-498.

Csanady, G. T., 1972: Frictional secondary circulation near an upwelled thermocline. (Paper presented to the Canadian Committee of Oceanography Symposium, Burlington, Ontario, May 4, 1972.)

Decker, F. W., 1961: The weather of Oregon. Oregon State University Press, Corvallis, 86 pp.

Defant, A., 1936: Das Kaltwasserauftribsgebiet vor der Küste Südwestafrikas. Länderkdl. Forsch. Festschr. Vollendung, 60, 52-66.

Denman, K. L., 1973: A time-dependent model of the upper ocean. J. Phys. Oceanogr., 3, 173-184.

_____, and M. Miyake, 1973: Upper layer modification at ocean station PAPA: Observation and simulation. J. Phys. Oceanogr., 3, 185-196.

Ekman, V. W., 1905: On the influence of the earth's rotation on ocean currents. Arkiv. Mat. Astron. Fysik, 12, 1-52.

[illegible], 1967: On gas
tion on ocean currents. Arkiv. Mat. Astron. Fysik, 12, 1-52.

Fortescue, G. E., and J. R. A. Pearson, 1967: On gas absorption into a turbulent liquid. Chem. Eng. Sci., 1163-1176.

REFERENCES

Allen, J. S., 1973: Upwelling and coastal jets in a continuously stratified ocean. J. Phys. Oceanogr., 3, 245-257.

Bang, N. D., 1973: Characteristics of an intense ocean frontal system in the upwell regime west of Cape Town. Tellus, 25, 256-265.

Bates, J. R., 1973: A generalization of the CISK theory. J. Atmos. Sci., 30, 1509-1519.

Budyko, M. I., 1956: The heat balance of the earth's surface. Translated from Russian by Office of Technical Services, U.S. Department of Commerce, 1966, 255 pp.

Charney, J. G., 1955: The generation of oceanic currents by wind. J. Marine Res., 14, 477-498.

Csanady, G. T., 1972: Frictional secondary circulation near an upwelled thermocline. (Paper presented to the Canadian Committee of Oceanography Symposium, Burlington, Ontario, May 4, 1972.)

Decker, F. W., 1961: The weather of Oregon. Oregon State University Press, Corvallis, 86 pp.

Defant, A., 1936: Das Kaltwasserauftribsgebiet vor der Küste Südwestafrikas. Länderkdl. Forsch. Festschr. Vollendung, 60, 52-66.

Denman, K. L., 1973: A time-dependent model of the upper ocean. J. Phys. Oceanogr., 3, 173-184.

_____, and M. Miyake, 1973: Upper layer modification at ocean station PAPA: Observation and simulation. J. Phys. Oceanogr., 3, 185-196.

Ekman, V. W., 1905: On the influence of the earth's rotation on ocean currents. Arkiv. Mat. Astron. Fysik, 12, 1-52.

[illegible] tion on ocean currents. Arkiv. Mat. Astron. Fysik, 12, 1-52.

Fortescue, G. E., and J. R. A. Pearson, 1967: On gas absorption into a turbulent liquid. Chem. Eng. Sci., 1163-1176.

Fowlis, W. W., J. D. Thompson, and W. E. Terry, 1974: A Laser-Doppler velocimeter with ocean applications. J. Mar. Res., 32, 93-102.

GARP Joint Organizing Committee, 1972: Parameterization of sub-grid scale processes. GARP Publications Series No. 8, 101 pp.

Garvine, R. W., 1971: A simple model of coastal upwelling dynamics. J. Phys. Oceanogr., 1, 169-179.

Gates, W. L., 1968: A numerical study of transient Rossby waves in a wind-driven homogeneous ocean. J. Atmos. Sci., 25, 3-22.

Geisler, J. E., and R. E. Dickenson, 1972: The role of variable Coriolis parameter in the propagation of inertia-gravity waves during the process of geostrophic adjustment. J. Phys. Oceanogr., 2, 263-272.

Gill, A. E., and A. J. Clarke, 1973: Wind-induced upwelling, coastal current and sea-level changes. (Unpublished manuscript.)

Grammeltvedt, A., 1969: A survey of finite-difference schemes for the primitive equations for a barotropic fluid. Mon. Wea. Rev., 97, 384-404.

Greenspan, H. P., 1968: The theory of rotating fluids. Cambridge Monographs on Mechanics and Applied Mathematics, Cambridge University Press, 327 pp.

Gunther, E. R., 1936: A report on oceanographic investigations in the Peru Coastal Current. Discovery Repts., 13, 107-276.

Halpern, D., 1973: Variations in the density field during coastal upwelling. (Presented at 2nd Conference on Analysis of Upwelling Ecosystems, May 1973, Marseilles, France.)

Holbrook, J. R., and R. M. Reynolds, 1973: Physical oceanographic observations made by the Pacific Oceanographic Laboratory off the Oregon coast during July and August, 1972. CUEA Technical Report 3, University of Washinton, Seattle.

Hansen, D. V., and Rattray, M. R., Jr., 1972: Estuarine circulation induced by diffusion. J. Marine Res., 30, 281-294.

Hantel, M., 1971: Zum Einflus des Entrainmentprozesses auf die Dynamik der Oberflächenschicht in eine, tropisch-subtropischen Ozean. Deutschen Hydrodynamischen Zeitschrift, 24, 120-137.

Harrison, E. J., 1973: Three-dimensional numerical simulations of tropical systems utilizing nested finite grids. J. Atmos. Sci., 30, 1528-1543.

_____, and R. L. Elsberry, 1972: A method for incorporating nested finite grids in the solution of systems of geophysical equations. J. Atmos. Sci., 29, 1235-1245.

Hart, T. J., and R. I. Currie, 1960: The Benguela Current. Discovery Repts, 31, 123-298.

Hidaka, K., 1954: A contribution to the theory of upwelling and coastal currents. Trans. Amer. Geophys. Union, 35, 431-444.

Holladay, C. G., 1974: Sea surface temperature analysis off Oregon during summer 1973. M.S. Thesis, Florida State University, Tallahassee (in preparation).

Hsueh, Y., and J. J. O'Brien, 1971: Steady coastal upwelling induced by an along-shore current. J. Phys. Oceanogr., 1, 180-186.

Hughes, P., and E. D. Barton, 1973: Physical investigations in the upwelling region off N. W. Africa on RRS DISCOVERY cruise 48. (Presented at the 2nd conference on 'Analysis of Upwelling Systems', Marseilles, France, May, 1973. To be published in the Conference issue of TETHYS.)

Hurlburt, H. E., 1974: The influence of coastline geometry and bottom topography on the eastern ocean circulation. Ph.D. Dissertation, Florida State University, Tallahassee.

_____, and J. D. Thompson, 1973: Coastal upwelling on a β-plane. J. Phys. Oceanogr., 3, 16-32.

Huyer, A., 1974: Observations of the coastal upwelling region off Oregon during 1972. Ph.D. Dissertation, Oregon State University, Corvallis.

_____, and R. L. Smith, 1972: Observations of a mixed bottom layer. CUE Notes, No. 8, 1-2.
State University, Corvallis.

_____, and R. L. Smith, 1972: Observations of a mixed bottom layer. CUE Notes, No. 8, 1-2.

Johnson, A., and J. J. O'Brien, 1973: A study of an Oregon sea breeze event. J. Phys. Oceanogr., 3, 1267-1283.

Johnson, D. R., 1973: The seasonal density structure and circulation on the continental shelf. Ph.D. Dissertation, The University of Miami, Florida.

Kato, H., and O. M. Phillips, 1969: On the penetration of a turbulent layer into a stratified fluid. J. Fluid Mech., 37, 643-655.

Kitaigorodskii, S. A., 1960: On the computation of the thickness of the windmixing layer in the ocean. Bull. (Izvestia) Social Sci. USSR, Geoph. Series, 284-287 (translated issue), 425-431 (original).

Kraus, E., 1959: The evaporation-precipitation cycle of the trades. Tellus, 11, 147-158.

_____, and C. Rooth, 1961: Temperature and steady state vertical heat flux in the surface layers. Tellus, 13, 231-238.

_____, and J. S. Turner, 1967: A one-dimensional model of the seasonal thermocline: II. The general theory and its consequences. Tellus, 19, 98-106.

Kullenberg, G., 1971: Vertical diffusion in shallow waters. Tellus, 23, 129-135.

Kwizak, M., and A. Robert, 1971: A semi-implicit scheme for grid point atmospheric models of the primitive equations. Mon. Wea. Rev., 94, 32-36.

Leith, C. E., 1968: Two-dimensional eddy viscosity coefficients. Proc. WMO/IUGG Symposium on Numerical Weather Prediction, Tokyo, Japan, Nov. 26-Dec. 4, 1968, I-41--I-44.

Longuet-Higgins, M. S., 1965: Planetary waves on a hemisphere bounded by meridians of longitude. Phil. Trans. Roy. Soc., A260, 317-350.

Mittelstaedt, E., and K. P. Koltermann, 1974: On the currents over the shelf off Cap Blanc in the Northwest African upwelling area. (Submitted for publication to Deutsche Hydrogr. Zeitschrift).

Mooers, C. N. K., 1970: The interaction of an internal tide with the frontal zone in a coastal upwelling region. Ph.D. Dissertation, Oregon State University, Corvallis.

Mooers, C. N. K., 1970: The interaction of an internal tide with the frontal zone in a coastal upwelling region. Ph.D. Dissertation, Oregon State University, Corvallis.

_____, C. A. Collins, and R. L. Smith, 1973: The dynamic structure of the onset of a coastal upwelling event. (Submitted for publication to J. Phys. Oceanogr.)

McNider, R. T., and J. J. O'Brien, 1973: A multi-layer transient model of coastal upwelling. J. Phys. Oceanogr., 3, 258-273.

Niiler, P. P., 1973: Deepening of the wind-mixed layer. (Unpublished manuscript.)

O'Brien, J. J., 1965: The non-linear response of a two-layer, baroclinic ocean to a stationary, axially-symmetric hurricane. Tech. Report, Ref. 65-34T, Texas A&M University, 99 pp.

_____, 1972: CUE-I Meteorological atlas. Vol. I. Coastal upwelling ecosystems analysis. International Decade of Ocean Exploration, 309 pp.

_____, 1973: A note on nonlinear eddy viscosity for two-dimensional numerical models. (Unpublished manuscript.)

_____, and R. Grotjahn, 1974: Intermittency in coastal upwelling. (To be submitted for publication to J. Phys. Oceanogr.)

_____, and H. E. Hurlburt, 1972: A numerical model of coastal upwelling. J. Phys. Oceanogr., 2, 14-26.

_____, and R. O. Reid, 1967: The non-linear response of a two-layer, baroclinic ocean to a stationary, axially-symmetric hurricane: Part I. Upwelling induced by momentum transfer. J. Atmos. Sci., 24, 197-207.

Orlanski, I., and B. B. Ross, 1973: Numerical simulation of the generation and breaking of internal gravity waves. J. Geoph. Res., 78, 8808-8826.

Pavlova, Y. V., 1966: Seasonal variations of the California current. Oceanology, 8, 801-814.

Pedlosky, J., 1974: On coastal jets and upwelling in bounded basins. J. Phys. Oceanogr., 4, 3-18.

Pietrafesa, L., 1973: Steady baroclinic circulation on a continental shelf. Ph.D. Dissertation, University of Washington, Seattle.

Pike, A. C., 1971: Intertropical convergence zone studied with an interacting atmosphere and ocean model. Mon. Wea. Rev., 99, 469-477.

Pillsbury, R. D., 1972: A description of hydrography, winds, and currents during the upwelling season near Newport, Oregon. Ph.D. Dissertation, Oregon State University, Corvallis. 163 pp.

_____, R. L. Smith, and J. G. Pattulo, 1970: A compilation of observations from moored current meters and thermographs, Vol. III. Oregon State University, Ref. 70-3.

Pollard, R. T., and R. C. Millard, 1970: Comparison between observed and simulated wind generated inertial oscillations. Deep Sea Res., 17, 813-821.

_____, P. B. Rhines, and R. O. R. Y. Thompson, 1973: The deepening of the wind-mixed layer. J. Geophys. Fluid Mech., 3, 381-404.

Rao, G. V., and T. S. Murty, 1973: Some case studies of vertical circulations associated with oceanic fronts. J. Geoph. Res., 549-557.

Rattray, M., 1960: On the coastal generation of internal tides. Tellus, 12, 54-62.

Rouse, H., and J. Dodu, 1955: Turbulent diffusion across a density discontinuity. La Houille Blanche, 10, 530-532.

Ryther, J. H., 1969: Photosynthesis and fish production in the sea. Science, 166, 72-76.

Saito, Y., 1956: The theory of the transient state concerning upwelling and coastal current. Trans. Amer. Geophys. Union, 37, 38-42.

Simmons, T. J., 1974: Note on diffusion in numerical models with variable layer depths. (To appear in J. Phys. Oceanogr.)

Smagorinsky, J., S. Manabe, and J. L. Holloway, 1965: Numerical results from a nine-level general circulation model of the atmosphere. Mon. Wea. Rev., 93, 727-768.

Smith, R. L., 1968: Upwelling. Oceanogr. Mar. Biol. Ann. Rev., 6, 11-47.

Smith, R. L., 1968: Upwelling. Oceanogr. Mar. Biol. Ann. Rev., 6, 11-47.

_____, 1973: A description of current, wind and sea level variations during coastal upwelling off the Oregon coast, July-August, 1972. J. Geophys. Res., 79, 435-443.

Stevenson, M. R., R. W. Garvine, and B. Wyatt, 1973: Lagrangian measurements in the coastal upwelling zone off Oregon. (Submitted for publication to J. Phys. Oceanogr.)

Stewartson, K., 1957: On almost rigid rotations. J. Fluid. Mech., 3, 17-26.

Suginohara, N., 1973: Coastal upwelling in a two-layer ocean by wind stress with longshore variation. (Unpublished manuscript.)

Summers, H. J., and K. O. Emery, 1963: Internal waves of tidal period off southern California. J. Geoph. Res., 68, 827-839.

Thompson, J. D., 1973: Sea surface temperatures mapping of coastal upwelling areas using remote sensing. (Presented to the Coastal Upwelling Experiment Workshop, January 23, 1973 in Tallahassee, Florida.)

_____, and J. J. O'Brien, 1973: Time-dependent coastal upwelling. J. Phys. Oceanogr., 3, 33-46.

_____, R. T. McNider, B. Soong, and J. J. O'Brien, 1972: Temporal changes in sea surface temperatures during coastal upwelling in CUE. (Paper presented at Fall Annual Meeting, American Geophysical Union, San Francisco, California.)

Thompson, S. M., 1969: Turbulent interfaces generated by an oscillating grid in a stably stratified fluid. Ph.D. Dissertation, University of Cambridge, England.

Thorade, H., 1909: Ann. Hydrogr. Bul., 37, 17-34, 63-76.

Turner, J. S., 1968: The influence of molecular diffusivity on turbulent entrainment across a density interface. J. Fluid Mech., 33, 639-656.

_____, 1973: Buoyancy effects in fluids. Cambridge Monographs on Mechanics and Applied Mathematics, Cambridge University Press, 367 pp.

_____, and E. B. Kraus, 1967: A one-dimensional model of the seasonal thermocline. I. A laboratory experiment and its interpretation. Tellus, 19, 88-97.

model of the seasonal thermocline. I. A laboratory experiment and its interpretation. Tellus, 19, 88-97.

Veronis, G., and H. Stommel, 1956: The action of variable wind stresses on a stratified ocean. J. Mar. Res., 15, 43-75.

Woods, J. D., 1968: Wave-induced shear instability in the summer thermocline. J. Fluid Mech., 32, 791-800.

_____, and R. L. Wiley, 1972: Billow turbulence and ocean microstructure. Deep Sea Res., 19, 87-121.

Wooster, W. S., and M. Gilmartin, 1961: The Peru-Chile undercurrent. J. Mar. Res., 19, 97-120.

Wyrtki, K., 1963: The horizontal and vertical field of motion in the Peru current. Bull. Scripps Inst. Oceanogr., 8, 313-346.

_____, 1967: Circulation and water masses in the eastern equatorial Pacific Ocean. Intern. J. Oceanol. Limnol., 1, 117-147.

Yoshida, K., 1967: Circulation in the eastern tropical oceans with special reference to upwelling and undercurrents. Japan J. Geophys., 4, 1-75.

VITA

James Dana Thompson, Jr., was born August 16, 1948 in Rutherfordton, North Carolina. In 1969 he graduated Phi Beta Kappa from the University of North Carolina at Chapel Hill with a B.S. in Physics. In 1969 he was awarded a fellowship for graduate study in the atmospheric sciences from the University Corporation for Atmospheric Research, Boulder, Colorado. He began his graduate study in the Department of Meteorology at the Florida State University in September, 1969 and was awarded the M.S. degree in 1971.